VOLUME 31 MARCH 1953 NUMBER 3

Canadian Journal of Physics

Editor: G. M. VOLKOFF

Published by THE NATIONAL RESEARCH COUNCIL
OTTAWA CANADA

CANADIAN JOURNAL OF PHYSICS

(Formerly Section A, Canadian Journal of Research)

The CANADIAN JOURNAL OF PHYSICS is published bimonthly by the National Research Council of Canada under the authority of the Chairman of the Committee of the Privy Council on Scientific and Industrial Research. Matters of general policy are the responsibility of a joint Editorial Board consisting of members of the National Research Council of Canada and the Royal Society of Canada.

The National Research Council of Canada publishes also: *Canadian Journal of Botany, Canadian Journal of Chemistry, Canadian Journal of Medical Sciences, Canadian Journal of Technology, Canadian Journal of Zoology.*

EDITORIAL BOARD

Representing

NATIONAL RESEARCH COUNCIL	ROYAL SOCIETY OF CANADA	
DR. J. H. L. JOHNSTONE (*Chairman*), Professor of Physics, Dalhousie University, Halifax, N.S.	DR. G. M. VOLKOFF, Professor of Physics, University of British Columbia, Vancouver, B.C.	Section III
DR. OTTO MAASS, Macdonald Professor of Physical Chemistry, McGill University, Montreal, P.Q.	DR. T. THORVALDSON, Dean Emeritus of Graduate Studies, University of Saskatchewan, Saskatoon, Sask.	
DR. CHARLES W. ARGUE, Dean of Science, University of New Brunswick, Fredericton, N.B.	DR. D. L. BAILEY, Department of Botany, University of Toronto, Toronto, Ont.	Section V
DR. A. G. MCCALLA, Dean, Faculty of Agriculture, University of Alberta, Edmonton, Alta.	DR. E. HORNE CRAIGIE, Department of Zoology, University of Toronto, Toronto, Ont.	

THE CANADIAN ASSOCIATION OF PHYSICISTS	THE CHEMICAL INSTITUTE OF CANADA
DR. G. M. VOLKOFF, Professor of Physics, University of British Columbia, Vancouver, B.C.	DR. H. G. THODE, Department of Chemistry, McMaster University, Hamilton, Ont.

Ex officio

DR. LÉO MARION (*Editor-in-Chief*), Director, Division of Pure Chemistry, National Research Laboratories, Ottawa.	DR. H. H. SAUNDERSON, Director, Division of Information Services, National Research Council, Ottawa.

Manuscripts should be addressed to:

DR. LÉO MARION,
Editor-in-Chief,
Canadian Journal of Physics,
National Research Council,
Ottawa, Canada.

Each manuscript should be typewritten, double-spaced, and the original and one extra copy submitted (see **Notice to Contributors** inside of back cover).

Subscriptions, renewals, and orders for back numbers should be addressed to:

Administrative Services,
National Research Council,
Ottawa, Canada.

Subscription rate: $3.00 a year; single numbers: 50 cents. Special rates can be obtained for subscriptions to more than one of the Journals published by the National Research Council.

Canadian Journal of Physics

Issued by THE NATIONAL RESEARCH COUNCIL OF CANADA

VOLUME 31 MARCH, 1953 NUMBER 3

THE INITIAL MAGNETIZATION OF NICKEL UNDER TENSION[1]

BY B. N. BROCKHOUSE[2]

ABSTRACT

In an attempt to resolve apparent discrepancies in the literature the initial susceptibility (χ) and Rayleigh constant (a) of pure nickel wire were measured between room temperature and the Curie point under various tensions (Z). For annealed nickel the quantity χZ is independent of Z, as required by Becker's theory, if the stresses are applied in order of increasing magnitude and if no plastic deformation occurs. χ and a are found to be connected by Néel's relation $a = c\,\chi^2\,J_0/J_s$. The same temperature dependence is shown by χZ as by the initial susceptibility of unstressed nickel given in the literature. At temperatures below 150°C. the temperature dependence of χZ is consistent with the recent theory of Döring. At higher temperatures χZ increases monotonically to the Curie point but at a smaller rate than Döring's low temperature theory predicts. This temperature dependence is in apparent conflict with Becker's theory and magnetostriction measurements of Döring and Kirkham. It is possible, but unlikely, that the conflict arises from the presence of textures in the various specimens. An appendix gives the textures of the wire specimens as found by neutron diffraction.

INTRODUCTION

The interaction of magnetostriction with internal stresses is one of the principal factors influencing the magnetization curves of ordinary materials. In fact experiments indicate that for a great many materials this is the dominant process. Unfortunately no method of determining the internal stresses is known and it is not possible to correlate directly experiment and theory. Accordingly it is important to determine whether the effect of an external stress upon the magnetization is in agreement with theory.

Becker's Theory

A theory of the magnetization curve of nickel under tension was first given by Becker (1) in 1930 and is fully discussed by Becker and Döring (2). His theory involves three assumptions:

(1) The magnetostriction is isotropic.

(2) The applied stress is so great that internal stresses and crystal anisotropy can be neglected.

(3) Only the lowest (nonzero) order terms in the expansion of the free energy in the direction cosines of the magnetization are important.

The magnetization of a nickel wire under tension is

$$[1] \qquad J = \frac{J_s^2}{3(-\lambda_s)}\frac{H}{Z}, \qquad \begin{matrix} Z \gg Z_i \\ \lambda_s Z \gg K \end{matrix}$$

[1] *Manuscript received July 16, 1952.*
Contribution from the Department of Physics, University of Toronto, Toronto, Ont.

[2] *Now with the Atomic Energy of Canada Ltd., Chalk River, Ontario.*

where λ_s is the saturation magnetostriction at T°K.,
J_s is the saturation magnetization at T°K.,
Z is the applied (tensional) stress,
Z_i is the internal stress,
H is the applied field parallel to Z,
K is the crystal anisotropy constant.

According to the theory, therefore, the magnetization curve should be a straight line whose slope is inversely proportional to the applied stress and which is reversible. Since in practice the internal stresses and crystal anisotropy are not completely negligible boundary movements and irreversible rotations also occur and the magnetization curve has a small curvature. Because of this the initial susceptibility $\chi = \underset{H \to 0}{\text{Lim}} \frac{J}{H}$ is the quantity which must be compared with experiment. On the Becker theory

$$\chi = \frac{J_s^2}{3(-\lambda_s)} \frac{1}{Z}. \qquad [2]$$

A careful experimental check of relation [2] has been made for nickel at room temperature by Kersten (8), who found the predicted inverse relation between χ and Z and about the correct value for the constant of proportionality. Since the magnetostriction of nickel is not isotropic, λ_s being -27×10^{-6} in the 111 directions and -54×10^{-6} in the 100 directions (2) at room temperature, Kersten used the mean value of $1/\lambda_s$ in comparing his results with the theory.

In 1935 Scharff (15) measured χ at temperatures from 20°C. to the Curie point (358°C.). She found that χ was proportional to $1/Z$ at all temperatures but that the proportionality constant was strongly temperature dependent. Her values of χZ are shown in Fig. 1.

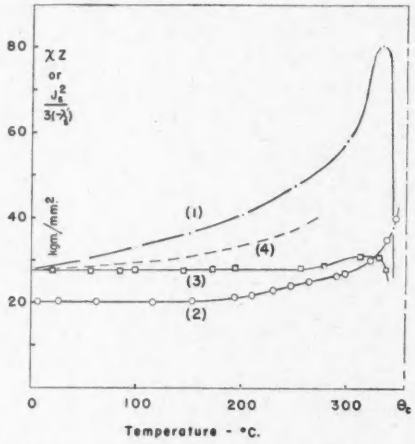

FIG. 1. Comparison of the quantities χZ and $J_s^2/3(-\lambda_s')$ as functions of the temperature:
(1) χZ by Scharff, Reference (15).
(2) $J_s^2/3(-\lambda_s')$ by Kirkham (10).
(3) $J_s^2/3(-\lambda_s')$ by Döring (4).
(4) Constant $\times$ J_0/J_s normalized to (1) and (3) at 0°C.

No measurements of λ_s, the true magnetostriction, have been made at temperatures other than room temperature but the so-called longitudinal magnetostriction (λ_s') has been measured from room temperature to the Curie point. This quantity is the fractional change in length of a specimen between the demagnetized state and saturation. It is proportional to $\bar{\lambda}_s$, the average of λ_s over the crystal directions, if the domain distribution in the demagnetized state is the same for all temperatures and equal to $\bar{\lambda}_s$ if the distribution is isotropic. The quantity $J_s^2/3(-\lambda_s')$ computed from the results of Döring (4) and Kirkham (10) is also shown in Fig. 1. It is immediately obvious that equation [2] is not obeyed. Equality of the three curves is not to be expected because of possible preferred orientations in the specimens but they should have the same temperature dependence. Döring's value of $J_s^2/3(-\lambda_s')$ at room temperature is about that expected for an isotropic specimen while Kirkham's value suggests that his specimen had a preferred orientation in the 100 direction. This preferred orientation could also be the reason for the change of slope at about 180°C. The crystal anisotropy constant (K) becomes very small at about this temperature, below it the distribution of domains in the demagnetized state is controlled by the crystal anisotropy and hence by the crystal orientation. Above this temperature the domain distribution is controlled by the internal stresses, and the two distributions may not be the same.

No satisfactory explanation for the apparent failure of formula [2] has been offered. Becker and Döring (2) suggest that it may be due to λ_s having different temperature dependence for different crystal directions since then $1/\bar{\lambda}_s$ and $\overline{1/\lambda_s}$ would not have the same temperature dependence and hence χZ and $J_s^2/3(-\lambda_s)$ would also be different. But they consider this explanation unlikely. However, the difference between Döring's and Kirkham's results lends some support to this suggestion, if the preceding discussion is invalid.

Döring's Theory

Döring (5) has recently put forward a new, fundamental, theory. He assumes that the individual spins are held in position by the exchange forces, the magnetic field, and stress anisotropy forces. In a low temperature approximation, and assuming isotropic magnetostriction, Döring finds

$$\chi Z = \text{constant} \times J_0/J_s \qquad [3]$$

where J_0 is the saturation magnetization at 0°K. A plot of χZ as given by [3] is shown in Fig. 1. The agreement with Scharff's results is improved but there is still a large discrepancy.

Peppiatt and Brockhouse (14) attempted to check Döring's theory at low temperatures where it is intended to apply. At low temperatures the crystal anisotropy of nickel becomes very large and hence high stresses are necessary to make $\lambda_s Z > K$. In order to support the high stresses cold worked wire must be used, but these authors found that at room temperature cold worked nickel and annealed nickel gave different values for χZ and also showed a different temperature dependence. This disagreement was interpreted to mean that internal stresses affect χZ for cold worked nickel, and hence that no useful results could be obtained at very low temperatures. At temperatures from

20°C. to 100°C. χZ for annealed nickel had a significantly smaller temperature dependence than that found by Scharff and was in agreement with equation [3], but this agreement cannot be considered very significant in view of the small temperature range and the resulting uncertainty.

EXPERIMENT AND CONCLUSIONS

Apparatus and Method

The work described in the previous section suggested the desirability of making new measurements of χZ up to the Curie point. Specimens of Johnson Matthey "specpure" nickel wire *A*, *B*, and *C* were prepared as described in Table I, in the form of rods 1 mm. in diameter and 250 mm. in length. The demagnetizing factor of these rods is sufficiently small to be neglected.

TABLE I

MECHANICAL AND HEAT TREATMENT OF SPECIMENS OF HARD-DRAWN NICKEL WIRE (JOHNSON MATTHEY "SPECPURE" NICKEL). TEMPERATURES ARE APPROXIMATE ONLY. THE TEXTURES OF THE SPECIMENS ARE GIVEN IN THE APPENDIX

Specimen	Heat treatment
A	Annealed 1 hour at 830°C. in H_2
B	Annealed 2 hours at 1000°C. in H_2
C	Annealed 1 hour at 700°C., straightened and then annealed 1 hour at 830°C. in H_2

The specimen was mounted in a vertical furnace and stresses applied by hanging weights. The main heater of the furnace was wound on a copper tube 30 cm. long, and differential heaters at the top and bottom were separately controlled by variable transformers. Four thermocouples at different points on the specimen indicated the degree of thermal uniformity. When the heaters were properly adjusted the maximum measured temperature difference was about 2°C. All heaters were bifilar wound to reduce stray magnetic fields.

The temperature at the center of the specimen was measured by a copper–constantan thermocouple which was calibrated at the beginning and end of the work. An internal reference temperature was provided by the Curie point itself which was found to be very sharp. It could be located to about 2°C. and was found to be 358°C., the accepted value, for all applied stresses.

The magnetization curves were taken by the ballistic "method of reversals". The search coil consisted of 1500 turns of copper wire insulated by silicone-glass and impregnated with alundum cement. The coil was satisfactory at 370°C. though the wire itself is rated at 250°C. The effect of the applied field was eliminated by mounting a similar coil parallel to the search coil and connecting the two in series opposition. The turns on the compensating coil were adjusted to provide complete compensation at room temperature with no specimen through the search coil. Measurements above the Curie point indicated that the compensation was satisfactory at all temperatures. The deflection of the ballistic galvanometer was thus directly proportional to the magnetization *J*.

The field coil was such that the applied field was very nearly uniform over the

length of the specimen. The vertical component of the earth's field was neutralized by use of an extra winding on the field coil.

As the furnace contained air it was thought necessary to check the specimens for oxidation. One of the specimens was weighed before and after an extended series of runs. No change in weight greater than 1 part in 10^4 was detected.

Determination of χZ

The principal work was done on specimen A. A stress of 3.82 kgm. per mm.^{2} was applied and the temperature held at 360°C. for several hours. Normal magnetization curves were then taken at various temperatures below 360°C. with this applied stress. The process was repeated for successively increased stresses. Since plastic deformation occurs more readily at the higher temperatures this procedure ensured that, for any given stress, the specimen was in the same metallurgical state at all temperatures.

Readings were taken for values of the magnetization J up to about 25 gauss.

Measured values of J/H were plotted against H and fitted with a straight line. This involves the assumption that Rayleigh's Law

[4] $$J = \chi H + aH^2$$

is obeyed for small fields, as it is by nearly all materials. The initial susceptibility χ is given directly by the intercept on the J/H axis.

As the galvanometer scale could be read to 0.05 gauss J-values in the range 5 to 25 gauss were useful for extrapolation to zero field. The uncertainty in χ from this cause is thus of the order of $\frac{1}{2}\%$.

A typical set of results for stresses of 7.60 kgm. per mm.^{2} is shown in Fig. 2. It will be seen that the fit by means of Rayleigh's Law is satisfactory.

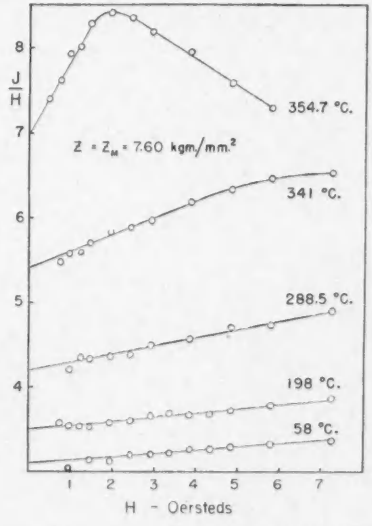

FIG. 2. Susceptibility of nickel wire under a stress of 7.60 kgm. per mm.^{2} at various temperatures.

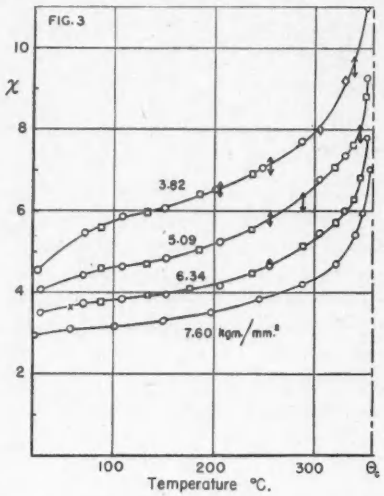

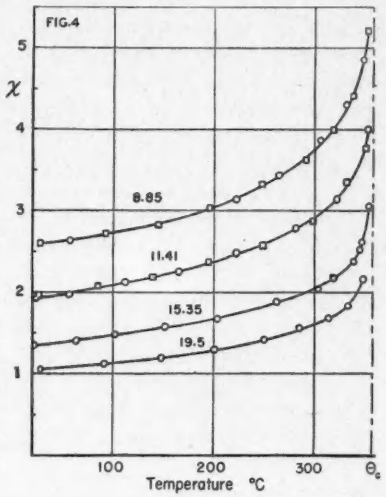

FIG. 3. Initial susceptibility (χ) of nickel wire (A) under various stresses as a function of temperature. In this and similar figures the points at any particular stress were taken in order of decreasing temperature.

FIG. 4. Initial susceptibility (χ) of nickel wire (A) under various applied stresses.

In Fig. 3 χ is shown plotted as a function of the temperature for different stresses. The different symbols indicate that the measurements were taken on different runs. In the case of the small stresses runs were sometimes made after exposure to a larger stress. The values obtained were independent of the order in which the stresses were applied when the stress was less than 7.60 kgm. per mm.^{2} Results for higher stresses are shown in Fig. 4. At these stresses the results

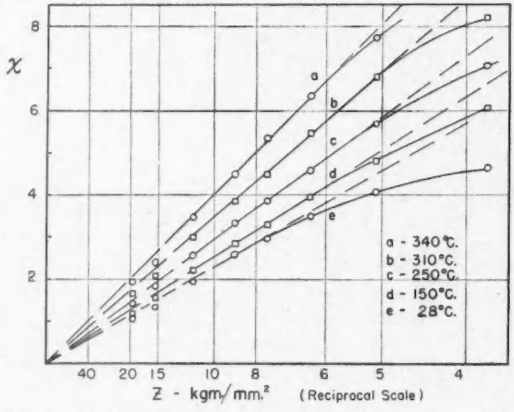

FIG. 5. Initial susceptibility plotted as a function of the inverse of the applied stress. The slope of the linear part of these curves is the quantity χZ of interest in this work.

were dependent on the order in which the stresses were applied. In the curves shown in Fig. 4 the maximum stress to which the specimen had been subjected after the heat treatment was the applied stress. The two symbols on the 8.85 and 11.41 kgm. per mm.^{2} curves represent successive runs at the same stress. The drooping of the curves in Fig. 3 for low stresses at low temperatures is due to the effect of crystal anisotropy, i.e., $\lambda_s Z \sim K$ in this region.

In Fig. 5 χ is plotted against the reciprocal stress $1/Z$ for a series of temperatures. Most of the points here plotted were obtained by interpolation from the curves of Fig. 3 and Fig. 4. The extent of the validity of the $1/Z$ law can be clearly seen. At low stresses deviations occur because of the internal stresses and, at the lower temperatures, crystal anisotropy. The proportionality between susceptibility and the reciprocal stress also breaks down at high stresses. Fig. 6 shows the reduction in area of the specimen as measured after exposure to stresses. The breakdown of the $1/Z$ relation occurs at about the technical yield point of the specimen.

The slopes χZ obtained from curves of the type of Fig. 5 are given in Table II

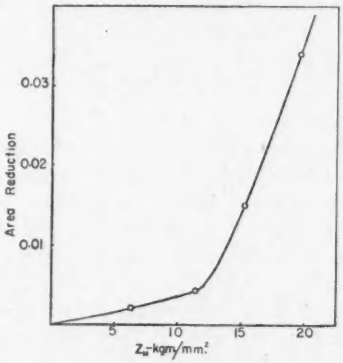

FIG. 6. Area reduction of 1 mm. diameter nickel wire (A) as function of maximum applied stress.

TABLE II

THE INITIAL SUSCEPTIBILITY OF NICKEL UNDER TENSION. VALUES OF χZ WERE OBTAINED FROM CURVES OF THE TYPE OF THOSE IN FIG. 5

T°C.	χZ	T°C.	χZ	T°C.	χZ
28	22.9	175	25.7	310	34.5
50	23.3	200	26.7	320	35.7
75	23.4	225	27.8	325	36.6
88	23.9	250	29.2	330	37.5
100	24.1	256	29.5	340	40.2
125	24.6	275	31.0	345	42.5
150	25.3	300	33.2	350	46
				354.7	53

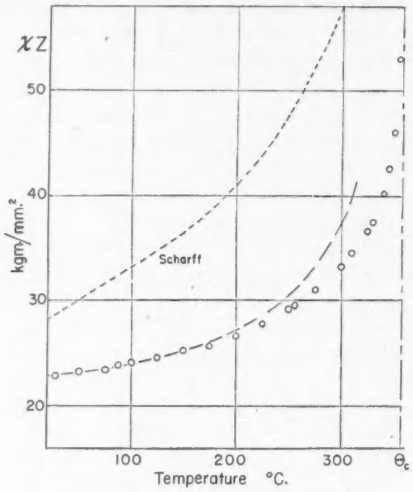

FIG. 7. Open circles are values of χZ found in this work. The dashed curve is Döring's formula [3], the constant having been adjusted for best fit at the low temperatures. The values of χZ found by Scharff are plotted for comparison.

and are plotted as a function of the temperature in Fig. 7. The points are not experimental but points for which interpolations were made. Döring's formula [3] gives the dashed line, the constant having been selected to fit the low temperature results. In the low temperature region the agreement is good but too much significance cannot be attached to this because the temperature effect is small in this region. At higher temperatures the experimental curve increases with temperature but more slowly than the theoretical curve. This increase appears to continue right up to the Curie point. Measurements very close to the Curie point (356°C.) were attempted and, though accurate readings could not be obtained, it was apparent that the susceptibility was still increasing.

This is contrary to the result obtained by Scharff (Fig. 1) whose χZ vs. T curve shows a maximum a few degrees below the Curie temperature. The explanation is believed to lie in the relative purity of the specimens. Scharff used nickel containing 0.6% manganese. According to Marian (12) the Curie point of this alloy is about 350°C. instead of 358°C. for pure nickel. In general the Curie points of alloys are difficult to measure, being "smeared out", possibly because of localized nonuniformities. A spread in the local Curie temperatures around a mean of 350°C. could account for the observations of Scharff.

In the lower temperature region there is also a large discrepancy between the curve of Fig. 7 and Scharff's results, also shown in the figure. Normalization of the two curves does not make them agree. It is thought that part of this difference arises in the following way. The magnetization curves obtained by Scharff consisted of three or four points only, taken in the range of magnetization zero

to 25 gauss, and fitted by a law of the form $J = \chi H$. Thus any curvature in the magnetization curve was neglected. In every case examined by Peppiatt (14) and the author the H^2 term in [4] was appreciable, as exemplified in Fig. 2. In general the constant a in equation [4] increases with temperature at a faster rate than χ itself. Assumption of a linear magnetization curve results in an erroneously high temperature variation of χ.

In order to determine, as far as possible, the extent to which the χZ vs. temperature curve of Fig. 7 is characteristic of nickel under tension as distinct from the particular specimen used, several experiments were performed. These subsidiary experiments are described in the two sections following.

Effect of Cold Working on χZ

Measurements were made at lower stresses after application of a higher seasoning stress. Fig. 8 shows one such set of measurements taken at various

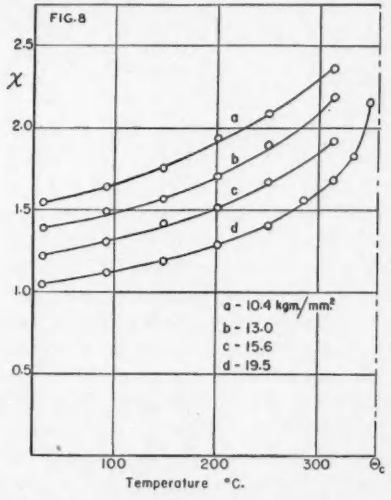

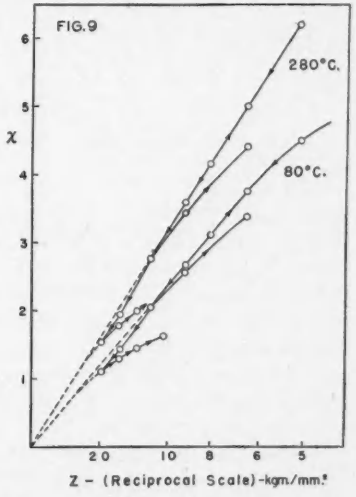

FIG. 8. Initial susceptibility of a nickel wire (A) at various stresses, after application of a seasoning stress of 19.5 kgm. per mm.² with resulting cold working.

FIG. 9. Initial susceptibility χ plotted against the reciprocal stress $1/Z$, showing effects of cold working. The arrows indicate the direction of change in applied stress.

stresses after application of a stress of 19.5 kgm. per mm.² This caused an area reduction of 3.4%. These values of χ are not proportional to $1/Z$ as is shown in Fig. 9 for two temperatures. On these curves the arrows indicate the direction of change in applied stress. Though χ is not proportional to $1/Z$ for cold-worked wire it appears possible that the curves are asymptotic to the curves obtained for annealed wire.

Effects of Annealing Procedure

Measurements were made on another specimen (B) which had been annealed at 1000°C. These results are shown in Fig. 10. The $1/Z$ relation is not obeyed,

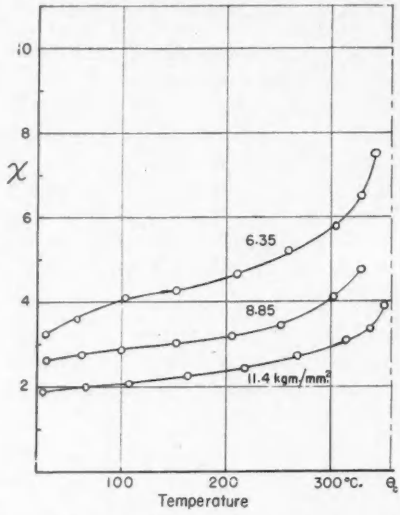

FIG. 10. Initial susceptibility of nickel wire (*B*) annealed two hours at 1000°C. under various applied stresses.

the initial susceptibility at the lower stresses being slightly too high. The 11.4 kgm. per mm.^{2} curve is identical with that for specimen *A* for the same stress, shown in Fig. 4. At this stress a small amount of cold working (0.32% area reduction) occurred. It is believed that at the lower stresses boundary movements made an appreciable contribution resulting in a higher susceptibility than expected and departure from the $1/Z$ law. This is supported by the observation that magnetization curves for these stresses had more curvature than usual. The slight cold working at 11.4 kgm. per mm.^{2} presumably suppressed the boundary movements.

The situation is complicated by the fact that metallurgical changes in the specimen can occur during the course of an experiment at temperatures below the Curie point. For certain purposes nickel is annealed at about 300°C. which results in small but definite changes in the mechanical properties. This is spoken of as "stress relief" or perhaps more properly "stress equalization".

A specimen (*C*), which had been annealed at the same temperature as *A* (but which had had different treatment prior to annealing as indicated in Table I), was studied under an applied stress of 6.37 kgm. per mm.^{2} at a temperature of 150°C. where the effects of crystal anisotropy are smaller than at room temperature. The curve of J/H vs. H is shown as curve I in Fig. 11. The specimen was then annealed for eight hours at 330°C. without removing the stress and the initial magnetization again measured at 150°C. (Curve II). The initial susceptibility is quite different from previously and is the same as that given in Fig. 3 for specimen *A* at the same stress. This experiment illustrates the necessity for making the measurements in a definite order of temperatures and stresses, and justifies the order of temperatures adopted.

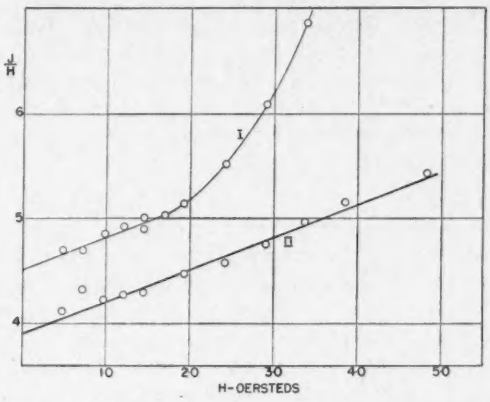

FIG. 11. Susceptibility of nickel wire (*C*) at 150°C. under stress of 6.37 kgm. per mm.² I-Annealed without stress as shown in Table I. II-Then annealed eight hours at 330° under stress of 6.37 kgm. per mm.²

Effects of Internal Stresses

Thiessen (16) found that nickel wires under stresses up to several kgm. per mm.² had susceptibilities much smaller than would be expected from equation [2] and that the susceptibility initially increased with applied stress. Thiessen found that repeated annealing eliminated the effect and he interpreted his results in terms of an anisotropic distribution of internal stresses.

No such effect was shown by the specimens used in the present work, but Peppiatt and Brockhouse (unpublished) observed that the susceptibility of specimens annealed at about 1100°C. did increase initially with applied stress. The slight cold working produced by a stress of 11.4 kgm. per mm.² was sufficient to destroy the effect, which in these specimens was equally prominent at temperatures from 20°C. to 200°C. This temperature independence indicated that crystal anisotropy was not involved and that the effect was caused by internal stresses. The stresses deduced from equation [2] had values of about 8 kgm. per mm.² and stresses of this order may thus be present in apparently well-annealed nickel.

In general internal stresses can affect the results in two ways (*a*) by causing deviation of the domain vectors from directions normal to the axis of the wire, hence permitting boundary movements to occur, and (*b*) by changing the mean stress over the volume of a domain, hence affecting the rotational susceptibility. A change in the mean stress will occur only if the internal stresses are coherent over volumes of the order of a domain volume and boundary movements can be appreciable only if the gradient of the internal stress is not too large. Both mechanisms thus require that the stress should be of long "period", i.e. a slowly varying function of position, as well as of large magnitude, in order to affect the results. It seems likely that annealing may increase the "period" of the internal stresses as well as decrease their magnitude, in the same way as it

promotes crystal growth. Hence it is not too surprising that specimen (*A*), annealed at a comparatively low temperature, seemed to show the most freedom from effects due to internal stresses, and that slight cold working eliminated most of the differences between specimens. In view of these considerations, the author does not believe that internal stresses appreciably affect the results given in Fig. 7 and Table II.

The Rayleigh Constant

The coefficient of the quadratic term in equation [4], known as the Rayleigh constant, was also computed from curves of the type of Fig. 2. One set of values is shown in Fig. 12. According to Néel (13) the quadratic term arises from

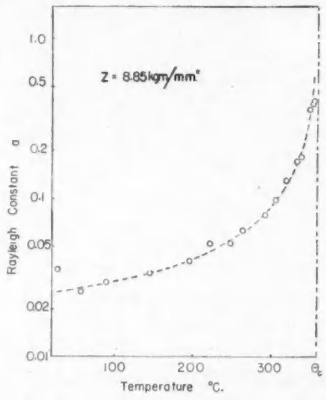

FIG. 12. Rayleigh constant of nickel wire *A* under stress of 8.85 kgm. per mm.^{2} The dashed curve is the best fit to equation [6].

irreversible boundary movements. It can be shown, simply and generally, that if the number of domain boundaries does not change with temperature and if the irreversible movements take place between definite positions in the crystal, which also do not change with temperature, then

$$[5] \qquad a = \text{constant} \times \frac{J_0}{J_s} \chi_B^2$$

where χ_B is the susceptibility due to boundary movements. This equation is given by Néel (13) but is not dependent on the details of his theory. The points in Fig. 12 are fitted with a curve of the form

$$[6] \qquad a = \text{constant} \times \frac{J_0}{J_s} \chi^2.$$

Within the rather poor accuracy the curves can be satisfactorily fitted though for some a better fit is obtained with an index slightly higher than 2. In general the deviation from the index 2 was greatest for those curves which failed to obey the $1/Z$ law. Since the initial susceptibility χ is believed to be due almost entirely to a rotation process, this implies that the rotation and boundary

movement processes probably have the same temperature dependence, and hence probably arise from the same mechanism—the interaction of magnetostriction with stress.

It is perhaps worth mentioning that over a considerable temperature range equation [6] turns out to be nearly

$$a = \text{constant} \times \chi^4,$$

the relation between a and χ found empirically by Radanovic and Weiss and de Freudenreich (17) for unstressed nickel.

GENERAL DISCUSSION

Initial Susceptibility of Unstressed Nickel

A large number of investigations of the initial magnetization of nickel have been made (7, 10, 16, 17). The collected results for the initial susceptibility are shown in Fig. 13. The temperature scale may be divided into two regions

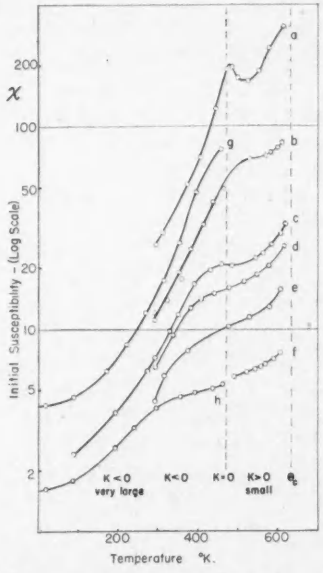

FIG. 13. Initial susceptibility of nickel by various authors. (*a*) Kirkham (10); (*b*) and (*c*) Kahan (7); (*d*) and (*e*) Thiessen (16); (*f*) Weiss and de Freudenreich (17); (*g*) and (*h*) author (unpublished). Generally speaking the initial susceptibility increases with annealing temperature.

according to the sign of the crystal anisotropy constant K. In the upper region the crystal anisotropy is usually negligible, i.e. $K \ll \lambda_s Z_i$. Where this condition is fulfilled the temperature dependence of χ is very nearly the same as that found for nickel under tension in this investigation. Curves *d*, *e*, *f* in this region have the same temperature dependence as (χZ) to within about 5% (see Fig. 7).

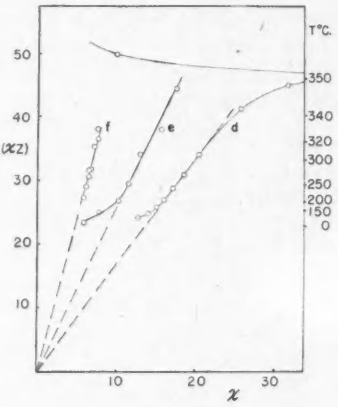

FIG. 14. Plot of χZ found in this work against initial susceptibility at the same temperature given in curves of Fig. 13. In the high temperature region proportionality holds between all the curves, within the accuracy of the data, except in the immediate vicinity of the Curie point.

This relationship is displayed in Fig. 14 in which (χZ) is plotted against values of χ taken from the curves in Fig. 13 at the same temperature.

The marked decrease in χ at lower temperature is believed by the author to arise from a mixing of rotation and boundary movements caused by demagnetizing fields produced at crystal and domain boundaries. Where crystal anisotropy is the dominant energy term ($K \gg \lambda_s Z_i$) the susceptibility for rotation

$$\chi_R = \text{constant} \times \frac{J_s^2}{K}.$$

This is usually only a small part of the total susceptibility, which comes principally from boundary movements. But the boundary movements are inhibited by demagnetizing fields produced at crystal and domain boundaries and at gross imperfections. These demagnetizing fields can be markedly reduced by the alternative rotation process and hence this has a profound effect on the over-all susceptibility. A detailed account of these ideas will be presented in another paper.

If any such theory of the falling off of the susceptibility at low temperatures is accepted then the variation of the high temperature susceptibility can properly be investigated only with specimens *which show no anomaly where K passes through zero* (*i.e. somewhere in the vicinity of* 450°*K.*),* *since only for these specimens will the condition* $K \ll \lambda_s Z_i$ *be satisfied at higher temperatures.* This excludes curves *a*, *b*, *c*. The remainder of the curves have, as noted, the same temperature dependence as stressed nickel, shown in Fig. 7.

**The measurements of Honda, Masumoto, and Shirakawa (6) show that above about 375°K. the (1, 1, 1) directions are no longer the easy directions of magnetization. It is believed (10, 3) that the anisotropy constant K changes sign somewhere above this temperature, but only the roughest estimate of K can be obtained, particularly in view of the fact that anisotropy constants of higher order and internal stresses may then be important.*

Other Magnetic Quantities

In addition to the initial susceptibility, expressions for other quantities have been derived from the strain theory, especially by Kersten (9). These include

(*a*) Alteration of remanent magnetization of a wire by an applied stress

$$\left(\frac{dJ_R}{dZ}\right)_{Z=0} = -\frac{J_s}{4Z_i}.$$

(*b*) Alteration of magneto-resistance by an applied stress

$$\frac{\partial}{\partial Z}\left(\frac{\Delta\rho}{\rho}\right) = -\frac{4}{15}\frac{D}{Z_i}$$

where D is found experimentally to be proportional to J_s^2.

(*c*) Change in Young's modulus E between the demagnetized state and saturation (ΔE effect)

$$\Delta\left(\frac{1}{E}\right) = \frac{2}{5}\frac{\lambda_s}{Z_i}.$$

Where the crystal anisotropy K can be neglected the measurements of Thiessen (16) and Köster (11) are in agreement with theory for all three effects, if Z_i is assumed to be independent of temperature.

It will be noted that all three effects arise from competition between external and internal stresses, while the initial susceptibility and Rayleigh constant involve competition between internal or external stress and a magnetic field. That is, the theory describes correctly the temperature dependence of processes which involve only stresses but not processes which involve both stress and fields. However existing information is consistent with the view that the latter processes have always the same temperature dependence. This is evidence for a fundamental origin of the failure of the Becker formula [2] but unfortunately not conclusive evidence. A study of the true magnetostriction (and perhaps χZ) as a function of temperature and crystal orientation is needed.

The author wishes to thank Prof. H. Grayson Smith of the University of Alberta for helpful correspondence.

APPENDIX

Texture Determination in Annealed Nickel Wires by Neutron Diffraction

The texture of cold worked nickel wire resembles that of copper, having a strong [111] texture and a weaker [100] texture, i.e. the normals to the (111) and (100) planes respectively tend to lie in the direction of the axis of the wire. The texture of annealed nickel wire has not, to the author's knowledge, been reported. By neutron diffraction studies with a crystal spectrometer, the textures in the specimens *A* and *B* used in this work have been determined. The results are for wires which were annealed as stated in Table I and then subjected to stresses as described in the text. It is believed that the stresses applied after annealing did not affect the texture appreciably. A specimen which had been annealed at about 1100°C. under the same conditions as the specimen used by Peppiatt and Brockhouse (14) was also tested. This specimen had not been stressed beyond the elastic limit.

Neutron diffraction provides an easy method of determining textures in annealed materials. The large areas of the beams used in neutron spectrometers and the great depth of penetration of the neutrons ensure that the pattern obtained applies to a large volume of the specimen and hence averages over a large number of crystals, even if the crystals are fairly big. Because of the large depth of penetration surface conditions are unimportant, in contrast to texture determination with X rays.

To achieve adequate counting rate the specimen wires were cut into short lengths and secured to thin aluminum foils as shown in Fig. *A*1. The wires

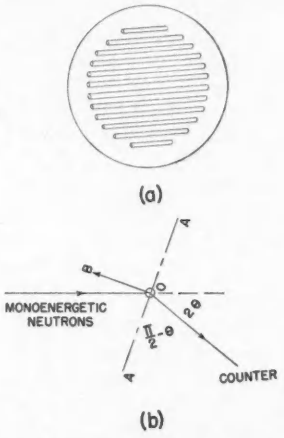

FIG. *A*1. (*a*) Form of specimen. Nickel wire segments are glued to a thin aluminum sheet. (*b*) Experimental arrangement. The counter rotates in plane of paper about *O*. The specimen is mounted in plane *A*-*A*, perpendicular to paper, and is rotated about the normal *OB*.

formed a circular array with diameter smaller than the neutron beam. With this construction no corrections for geometry or absorption were required.

The array was located in the plane *A*-*A* which normally bisected the angle between the incident and emergent beams but could be rotated out of this position. The spectrometer was set on the appropriate Debye Scherrer line (h, k, l) and the array was rotated in the plane *A*-*A* about the normal *OB*. The intensity of the line was recorded as a function of the angle which the axes of the wires made with the spectrometer plane. This intensity is proportional, neglecting extinction, to the volume of material with planes (h, k, l) perpendicular to the bisector of the angle between the incident and the emergent beams (in Fig. *A*1 line *OA*). Since the wire has cylindrical symmetry this intensity gives directly the distribution of the planes with respect to the axis of the wire.

The distributions for the (111), (200), and (220) planes are shown in Fig. *A*2. The texture may be described as a [100] texture ($25 \pm 10\%$) and a texture ($65 \pm 10\%$) in which a 111 axis makes a small angle with the axis of the wire. This angle appears to increase with annealing temperature. The texture of cold

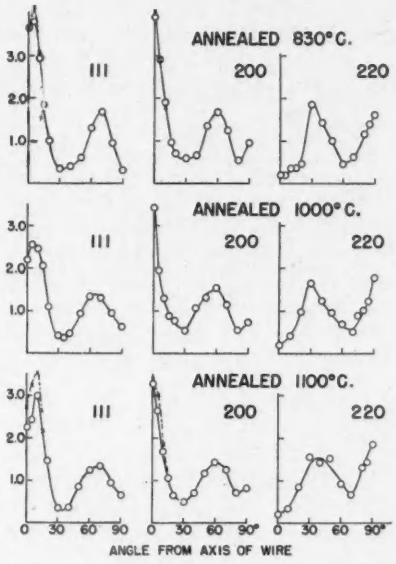

FIG. A2. Normalized intensities of 111, 200, and 220 lines of specimens annealed at 830°C. (*A*), 1000°C. (*B*), and 1100°C. as a function of the angle between the wire axis and the spectrometer plane (plane of the paper in Fig. A1). The crosses represent intensities measured with the axes of the wires in the spectrometer plane as a function of the angle between the plane and the "half-angle" position of the specimen.

worked wire (from another source however) was verified to be [111] with a weaker [100] texture. Further work is being done on textures of annealed materials and will be reported in a separate publication.

The work described in this appendix was carried out at the Chalk River Laboratory of Atomic Energy of Canada, Ltd.

REFERENCES

1. BECKER, R. Z. Physik, 62: 253. 1930.
2. BECKER, R. and DÖRING, W. Ferromagnetismus. Verlag von Julius Springer, Berlin. 1939.
3. BOZORTH, R. M. Phys. Rev. 50: 1076. 1936.
4. DÖRING, W. Z. Physik, 103: 560. 1936.
5. DÖRING, W. Z. Physik, 124: 501. 1948.
6. HONDA, K., MASUMOTO, H., and SHIRAKAWA, Y. Sci. Repts. Tôhoku Imp. Univ. 24: 391. 1935.
7. KAHAN, T. Ann. phys. 11^{E} Series, 9: 105. 1938.
8. KERSTEN, M. Z. Physik, 71: 553. 1931.
9. KERSTEN, M. Z. Physik, 85: 708. 1933; 82: 723. 1933.
10. KIRKHAM, D. Phys. Rev. 52: 1162. 1937.
11. KÖSTER, W. Z. Metallkunde, 35: 57. 1943.
12. MARIAN, V. Ann. phys. 7: 459. 1937.
13. NÉEL, L. Cahiers phys. No. 12, 1. 1942; No. 17, 47. 1943.
14. PEPPIATT, H. J. and BROCKHOUSE, B. N. J. Applied Phys. 22: 985. 1951.
15. SCHARFF, G. Z. Physik, 97: 73. 1935.
16. THIESSEN, G. Ann. Physik, 38: 5, 153. 1940.
17. WEISS, P. and DE FREUDENREICH, J. Arch. sci. phys. et nat. 42: 449. 1916.

COUNTING RATE MEASUREMENT BY INTERVAL SAMPLING[1]

By M. F. Crouch and G. E. Haynam

ABSTRACT

Two methods are described for measuring high counting rates with a counting device having a long resolving time. Both methods are based on the deliberate introduction of a large but calculable counting loss to transform a high counting rate to a lower rate. Formulas giving the counting rate in terms of the reduced rate are presented, together with formulas for the standard deviation of the counting rate. The performance of circuits used to study one of the methods is described, and a comparison is made with conventional rate measurement methods. It is found that, while the relative simplicity of equipment is gained at the expense of speed of measurement, the latter sacrifice is not as severe as might be expected.

INTRODUCTION

In addition to the two conventional methods for measuring high counting rates with a Geiger–Müller counter, viz. by means of scaling circuits and by the use of counting rate meters, a third method, which might be called "interval sampling", can, in principle, be used. This method makes use of the fact that the distribution function (Equation [1], Fig. 1) for the time intervals between successive G-M counter pulses arriving at a mean rate R,

$$[1] \qquad P_0(t) = R \exp(-Rt),$$

is a known function possessing a "tail" at its upper end. By measuring the rate of arrival S of intervals longer than some predetermined value T, corresponding

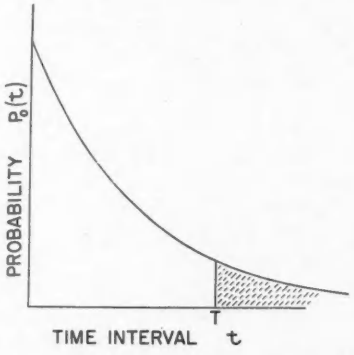

Fig. 1. Distribution function for time intervals between G-M counter pulses.

to the shaded "tail" of Fig. 1, the counting rate R can be found by using the implicit relation Equation [2].

$$[2] \qquad S = R \exp(-RT)$$

[1] *Manuscript received September 26, 1952.*
Contribution from the Department of Physics, Case Institute of Technology, Cleveland, Ohio, U.S.A.

However large R may be, a value of T can always be found to make S sufficiently low to be measured with an electromechanical register. Thus, whereas the scaler passes on 1/64 or 1/100 of the G-M counter pulses to the message register, in a regular fashion, the interval sampling circuit passes on a fraction $S/R = \exp(-RT)$ of the G-M counter pulses, in random fashion. It might therefore appropriately be designated a "pseudoscaler".

Although Equation [2], regarded as a counting loss formula, has been verified (5, 6) up to a scaling factor $R/S = 25$, no previous attempt seems to have been made to utilize Equation [2] as the basis of counting rate measurements, which would require values of R/S ($= \exp(RT)$) up to 300 and larger. Although the apparent lack of any previous studies of this method is possibly attributable to several inherent disadvantages, it was nevertheless felt worth while to investigate certain aspects of the method.

The investigation to be described had four objectives, which were (*a*), to ascertain the value or values of T needed to accommodate G-M counter rates from 0 to 50,000 counts per min., (*b*), to design and test circuits for performing the operation of interval sampling, such circuits to have T-values readily calculable from the circuit constants, (*c*), to investigate how the time required for a counting rate determination by the interval sampling method varies with the counting rate, the accuracy desired, and the accuracy of time discrimination, and (*d*), to determine the advantages and disadvantages of this method over conventional methods.

A related method for measuring rates with long resolving time equipment, which suggests itself when ways are considered to utilize the register at higher rates, will also be briefly discussed. This method is basically different, but it is equally well described as "interval sampling". In this method, the counting device is rendered sensitive every τ seconds for a brief interval of time T. If the register records a single count whenever one or more input counts are received during the sensitive interval T, then the relation between input counting rate R and output counting rate S is

$$S = (1/\tau)(1 - \exp(-RT)). \qquad [3]$$

This method will be discussed briefly in the following section, but no analysis of actual circuits will be presented.

THEORY

Equation [2], giving the relation between rates R and S for the first method, has been derived by several authors (1, 5). In addition, Feller (1) has worked out the rigorous expression for the standard deviation of the rate S. His result, to a sufficient approximation for the present purpose, is given in Equation [4].

$$\sigma_s = (n_s(1 - 2ST))^{\frac{1}{2}} \qquad [4]$$

(n_s is the total number of sampled counts). When Equation [2] is regarded as an implicit relation between R, S, and T, the relation between the errors of these quantities is computed to be (7)

$$\sigma_R/R = (1/1 - RT)\sqrt{((1 - 2ST)/n_s) + (RT)^2(\sigma_T/T)^2}. \qquad [5]$$

Although the error in R is seen to be a function of R, S, T, n_s, and σ_T/T, each value of R in normal operation is associated with unique values of S and T. Therefore by assuming a reasonable value for σ_T/T, a one-to-one correspondence between n_s and R exists for any desired accuracy σ_R/R of rate measurement. After the circuits that were tested have been described, Equation [5] will be used to calculate typical values for the time required to determine R to a given accuracy.

Equation [3], for the alternative method described in the introduction, is derived as follows: For G-M counter pulses occurring at a rate R and having a Poisson distribution, the probability of no count occurring in a given time interval T is easily found to be $q = \exp(-RT)$. Therefore the probability of one or more G-M counts in a given time interval T is $p = 1 - \exp(-RT)$. Since q and p also represent respectively the probability of zero and one count recorded on the message register, the frequency distribution of the number of counts recorded in a fixed period of time is a binomial distribution. The standard formula (Fry (2)) for the mean of the distribution leads at once to [3]. Similarly the standard deviation formula becomes, in the present case,

$$\sigma_s = \sqrt{n_s \exp(-RT)}. \qquad [6]$$

In [6] the coefficient of $\exp(-RT)$ should be the mean expected number of recorded counts. Ordinarily it is a reasonable approximation to use the actual number n_s.

All of the expressions given here for rates and standard deviations are asymptotic expressions valid only for measurement times large compared to the critical times T and τ.

EXPERIMENTAL METHOD

As a working basis, maximum and minimum values for S of 10 counts per sec. and 2.5 counts per sec. were assumed—the former being the approximate upper limit of the Cenco dial-type message register and circuit used, for random pulses, and the latter being an arbitrarily imposed lower limit on the rate of data accumulation. The first circuit studied, designated ISC-1, has been described in a preliminary form (4). It contains a scale-of-two to permit analysis of every other interval, so that S and R are related as in Equation [7].

$$S = \tfrac{1}{2} R \exp(-RT) \qquad [7]$$

With this arrangement, four values of T are sufficient to cover the range of counting rates desired. Fig. 2 is a plot of the family of curves (Equation [7]) of S vs. R for the four chosen values of T. The range of counting rates over which each value of T is used is indicated by the heavy portion of each curve. Fig. 3 is a plot of the counting rate versus the scaling factor R/S plotted on a logarithmic scale. Plotted in this manner, Equation [7] becomes a straight line with slope $1/T$, R/S intercept 2. Fig. 4 gives the same straight-line plot for a circuit described by Equation [2], five values of T being needed to cover the desired range of values of R.

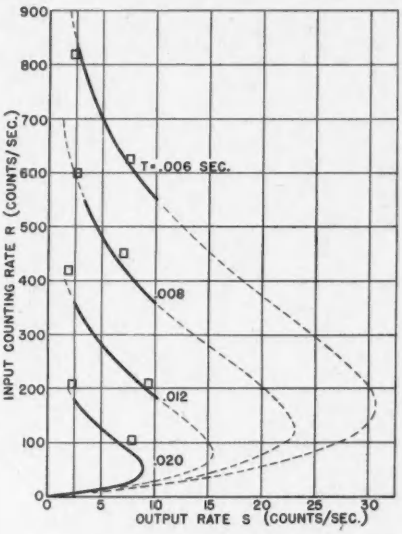

FIG. 2. Output rate vs. input counting rate, ISC-1.

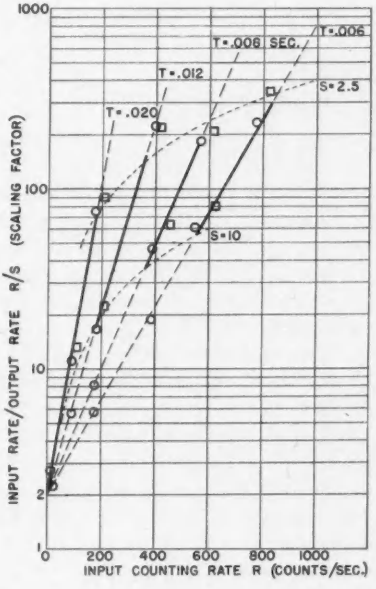

FIG. 3. Input counting rate vs. scaling factor, ISC-1.

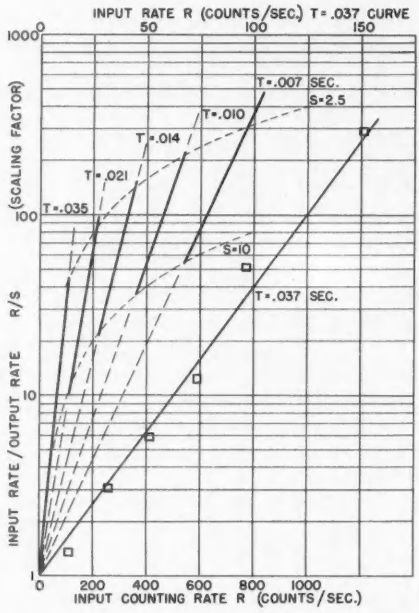

FIG. 4. Input counting rate vs. scaling factor, ISC-2.

The ISC-1 circuit (Fig. 5) was a straightforward approach to the problem, with little regard for economy of tubes. In brief, an exponential saw-tooth generator is turned on for the duration of each interval studied, so that the length of the time interval is indicated by the final voltage amplitude of the saw-tooth. These saw-tooth signals are then applied to a series diode amplitude discriminator, the cathode of which is maintained, in the absence of signals, at a reference potential corresponding to the critical time desired. An additional diode is used to clamp the cathode of the discriminator diode after it has risen 3 volts above the reference potential, so that this potential cannot stray far from its proper value. The discriminator output is amplified and used to trigger a multivibrator message register driver.

The saw-tooth generator used is a standard sweep generator using a "hard" tube, whose plate potential rises exponentially with a time constant RC when the grid is driven below cutoff, but returns to its starting value very quickly when the grid signal is removed because the capacitor C is recharged by current flowing through the tube. It is to be noted that the nonlinear character of the saw-tooth doesn't introduce any difficulty in this application.

The second circuit tested (miniaturized), designated ISC-2 (Fig. 6), represents an attempt to perform the interval sampling operation with a near-minimum of vacuum tubes. Here the same saw-tooth generator is used, except that it is normally cut off in this case, and the grid signal consists of short positive pulses applied at the start of each interval.

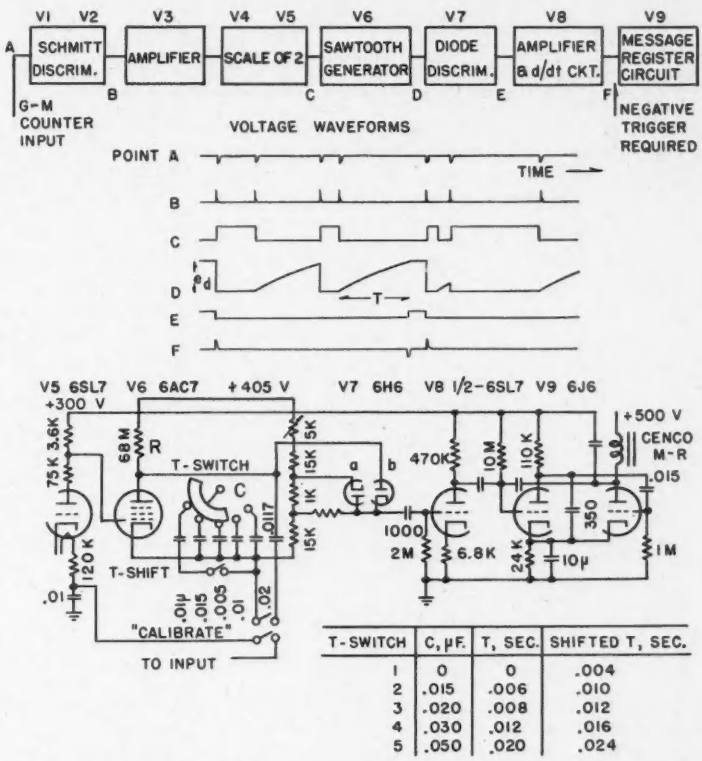

T-SWITCH	C, μF.	T, SEC.	SHIFTED T, SEC.
1	0	0	.004
2	.015	.006	.010
3	.020	.008	.012
4	.030	.012	.016
5	.050	.020	.024

FIG. 5. Block diagram, wave forms, and partial schematic circuit diagram, ISC-1.

RESULTS

The curves characterizing ISC-1 were verified along their entire length (circular data points, Fig. 3) using an auxiliary scaling circuit to measure the rate S. The complete ISC-1 circuit including message register was then checked (square data points) near the ends of the range of R-values covered with each value of T. The agreement between experimental results and the theoretical curves was felt to be satisfactory, since, with the exception of the timing capacitors, the circuit was assembled from ordinary circuit components such as carbon resistors with $\pm$ 10% tolerance.

The performance of ISC-2 was verified only for $T \cong 0.04$ sec., since experience had shown it to be most difficult to obtain proper operation for the larger T-values. Fig. 7 is an oscilloscope photograph of the wave form at the saw-tooth generator. The plate potential drops so rapidly at the start of each interval that the camera doesn't record this part of the wave form. The discriminator output is used as a blanking signal, so that a gap in the trace should (and does) occur each time there is an interval long enough for the associated saw-tooth to rise

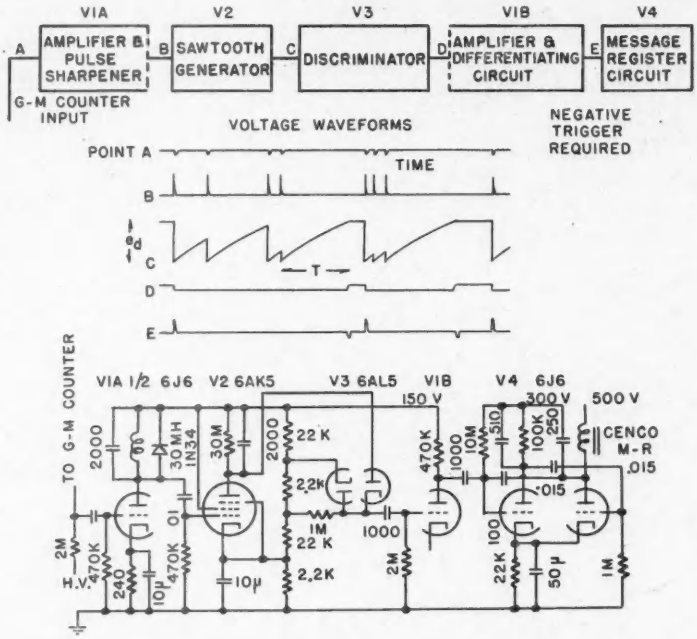

FIG. 6. Block diagram, wave forms, and schematic circuit diagram, ISC-2.

to the discriminator reference potential. The clamping action which takes place as soon as the discriminator pulse is generated is also apparent from the photograph, the apparent slight drift after clamping being an oscilloscope distortion.

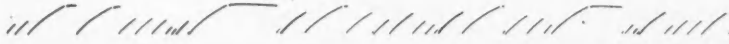

FIG. 7. Oscillogram of saw-tooth generator output voltage vs. time, ISC-2.

The relationship between circuit parameters and the T-value of the circuit is readily found for both circuits to be

$$\exp\,(T/RC) = (E_{bb} - e_{b0})/(E_{bb} - e_d), \tag{8}$$

where E_{bb} = saw-tooth generator plate supply potential, e_{b0} = saw-tooth generator plate potential (no signal), and e_d = discriminator diode cathode potential. This expression is found to give T-values agreeing closely with those inferred from the slope of the curves through the experimental points of Figs. 3 and 4. As an example, for circuit ISC-1 operated with a nominal T-value of 0.006 sec., the circuit constants were measured as $R = 0.68$ MΩ, $C = 0.015$ μf., $E_{bb} = 110$ v., $e_{b0} = 1.7$ v., and $e_d = 48.0$ v. Using these values, Equation [8] gives $T = 0.057$ sec. Thus the requirement that T be calculable from the circuit parameters is reasonably well satisfied.

Since the Schmitt circuit of ISC-1 responds readily to sinusoidal inputs, a simple alternative procedure for setting the discriminator level to correspond to a desired value of T can be employed using an audio-frequency oscillator connected to the input. As the frequency is raised, a point is reached at which the message register suddenly stops counting. Calling this frequency f_c, the T-value is given by $T = 1/f_c$. Alternatively, the discriminator can be set by connecting the a-c. filament voltage to the input and using the appropriate T-value.

DISCUSSION

Having shown that circuits can be made to perform the operation of interval sampling (first method), it remains to consider the effect on speed of measurement of counting only the long intervals. As an example, Table I lists (for circuit ISC-2) the number of sampled counts n_s and the average time t to register these counts in order to give a standard deviation of 5% in the inferred value for R (i.e., $\sigma_R/R = 0.05$). It was assumed that $\sigma_T/T = 0.02$, requiring,

TABLE I

NUMBER OF SAMPLED COUNTS NEEDED TO DETERMINE R TO 5% ACCURACY (ISC-2)

Input rate R (counts/sec.)	T (sec.)	No. of sampled counts n_s	Avg. time of measurement (sec.)	Conventional measurement time (sec.)
833	.007	21.6	8.9	0.5
700	.007	32.6	6.3	0.6
540	.007	61.3	5.2	0.7
540	.010	25.8	10.4	0.7
460	.010	39.0	8.2	0.9
360	.010	68.6	7.0	1.1
360	.014	30.4	13.1	1.1
300	.014	47.2	10.5	1.3
220	.014	102	10.1	1.8
220	.021	37.5	17.3	1.8
160	.021	81.5	14.7	2.5
110	.021	252	23.0	3.6
110	.035	58.0	24.8	3.6
80	.035	133	27.3	5.0
60	.035	385	52.4	6.7

according to Equation [8], that the threshold potential be held to about 1½%. Fig. 8 is a graph of time of measurement vs. rate.

The most striking feature of the ISC method is apparent from Table I, viz. that, despite the randomness of arrival of the sampled pulses, the counting rate can be determined to within 5% by a total count of as little as 22 counts, instead of the usual 400. This surprising result is due to the fact that, except for a range of very low rates, a given percentage variation of R-values corresponds to a much larger range of S-values, percentagewise. That is, there is a sort of "band spread" effect, to borrow a term from radio communication. As a result of this effect, the measurement time is < 15 sec. for $220 \leqslant R \leqslant 833$ per sec., and it is < 50 sec. for $65 \leqslant R \leqslant 833$ per sec.

However the region of the maximum of the S vs. R curve (Fig. 2) is readily seen to be characterized by inherently low accuracy, and the limit of accuracy

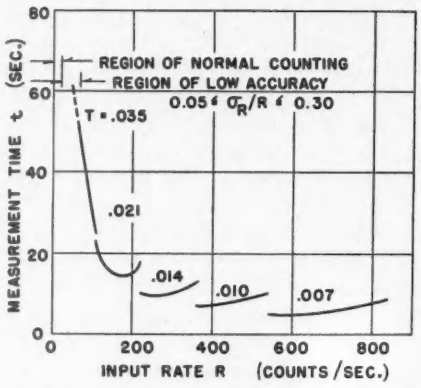

FIG. 8. Measurement time for 5% error in R, ISC-2.

of measurement depreciates to $\pm$ 30% in the worst case. It is, of course, possible to remedy this difficulty by providing additional T-values, avoiding the use of this region of any of the curves.

In evaluating the possible utility of the interval sampling method, one observes the following advantages:

1. Simplicity (cf. Fig. 6). The improvement over conventional scaler circuits is quite considerable. Counting rate meters, although simple in principle, are usually somewhat more complex.

2. Nonsusceptibility to multiple G-M counts, which provide the *nonconstant* contribution to the slope of the G-M "plateau".

3. Adaptability to the preset time method of rate measurement. For a wide range of rates (cf. Fig. 8), a fixed duration of measurement yields roughly a constant precision of measurement.

4. The "band spread" effect noted above leads to unexpectedly short times of measurement, although the speed of measurement is still far less than with conventional methods.

5. All rates from 0–50,000 per min. and greater can be counted. This constitutes an advantage over the counting rate meter, which is not adaptable to very low rates, such as one encounters in cosmic ray measurements, etc.

6. Poisson distribution histograms, for student laboratory experiments, are readily obtained without additional equipment.

To summarize the disadvantages, they are:

1. Speed of measurement is sacrificed, although the sacrifice is not so drastic as might be expected. (Cf. Table I.)

2. Only input pulses obeying a Poisson distribution can be counted.

3. Accuracy is limited by the precision with which the time discrimination can be accomplished.

4. The curve of S vs. R is double valued (cf. Fig. 2), although one can easily devise simple operational procedures for eliminating this ambiguity.

5. The circuit gives only rates, and cannot give number of counts.
6. A calibration curve is required.
7. The proper T-value must be selected to give $2.5 \leqslant S \leqslant 10$ counts per sec.

It is acknowledged that the advantages of this method of rate measurement are probably not sufficiently compelling to make it a serious competitor to the scaler or counting rate meter at present, except possibly for low rate measurements. Hence the results are presented primarily for their own intrinsic interest, with the added thought that the results may be of practical use in some future rate measurement problem which may be especially amenable to solution by the interval sampling method. Faster message registers now becoming available may permit ISC-type circuits with improved characteristics.

In this connection, the lack of a practical motivation means that the circuits described are far from being engineered circuits. Should an actual application arise, more elegant and reliable circuits, or possibly mechanical devices for accomplishing the same end, could undoubtedly be developed.

Although the second method has not been studied by analysis of actual circuits, it is apparent that it does have the advantage of a single-valued relation (Equation [3]) between R and S. Moreover, using a reasonable value of τ, say 1/30 to 1/60 sec., the entire useful range of input counting rates can be covered with only two different T-values. The actual circuit to accomplish this type of counting could be quite simple—for example an a-c. operated phase-controlled shield grid thyratron circuit would exhibit the desired periodic intermittent sensitivity. It is also apparent that this method can be used for rate measurement of incoherent periodic phenomena.

Recently Greenberg and Happ (3) have described another instrument for studying the statistical properties of counter pulses. With their method the mean deviation is continuously measured, in conjunction with a conventional counting rate measurement.

The authors wish to express thanks to Prof. A. L. Hughes, Dr. O. S. Duffendack, Prof. Jonathan Townsend, and Dr. Harold Lyons for helpful criticisms. The helpful suggestions of the referee, particularly that pointing out an error in Equation [4] as originally written, are gratefully acknowledged.

REFERENCES

1. FELLER, W. Studies and essays. Courant Anniversary Volume. Interscience Publishers, Inc., New York. 1948.
2. FRY, T. C. Probability and its engineering uses. D. Van Nostrand Company, Inc., New York. 1928.
3. GREENBERG, L. H. and HAPP, W. W. Can. J. Phys. 30: 317. 1952.
4. HAYNAM, G. E. Thesis, Case Institute of Technology, Cleveland, Ohio. 1951.
5. HUGHES, A. L. Am. Phys. Teacher, 7: 271. 1939.
6. LIFSCHUTZ, H. and DUFFENDACK, O. S. Phys. Rev. 54: 714. 1938.
7. MARGENAU, H. and MURPHY, G. M. The mathematics of physics and chemistry. D. Van Nostrand Company, Inc., New York. 1943. Section 13.35.

PLAFONNEMENT DES AEROSTATS A GRANDE ALTITUDE[1]

PAR PIERRE DEMERS

SOMMAIRE

On décrit un procédé simple combinant l'usage de ballons fermés de caoutchouc et d'un ballon ouvert de taille moyenne en Polythène, qui a permis de faire plafonner pendant 9 à 10 heures, des émulsions sensibles aux rayons cosmiques à des altitudes comprises entre 24 et 32 km.

1. INTRODUCTION

L'étude des rayons cosmiques avec des ballons requiert de préférence une ascension rapide, un plafonnement prolongé et une descente rapide. Ces conditions ne sont pas faciles à réaliser par l'emploi des seuls ballons de caoutchouc fermés à moins de mécanismes lance-ballasts. Ils gardent en effet leur force ascensionnelle et continuent de monter jusqu'à ce qu'ils crèvent. Le plafonnement est impossible avec un seul ballon qui suffirait pourtant à porter une charge intéressante pour l'expérimentateur. Théoriquement un système de trois ballons ou davantage, gonflés de façon à régler très exactement les hauteurs d'éclatement et les vitesses ascensionnelles, assure le résultat cherché, mais ce réglage est difficile et aléatoire vu les propriétés variables des ballons. Des systèmes de nombreux ballons avec une forte charge sont plus faciles à régler, et donnent parfois un bon plafonnement, mais les renseignements publiés font défaut à ce sujet. En somme avec des ballons de caoutchouc fermés, une faible charge peut bien être portée à une grande altitude, mais elle n'y plafonne pas facilement.

D'autre part, nous avons décrit un nouveau procédé de fabrication des ballons de Polythène ouverts (3). Les ballons de ce type sont capables de plafonner. Cependant avec les matériaux actuellement disponibles pour leur construction, le plafonnement au-dessus de 25 km. exige des ballons vastes et lourds, dont la manipulation est peu commode. Ces ballons n'apportent pas une solution au problème du plafonnement de petites charges à de plus grandes altitudes.

2. PROCÉDÉ NOUVEAU

Au cours de l'été 1952, nous avons essayé une solution qui s'est avérée excellente, et qui apparemment n'a pas été décrite ailleurs. Elle combine des ballons de caoutchouc fermés, de force ascensionnelle constante, et un ballon de Polythène ouvert, de taille moyenne, qui perd à mesure qu'il monte, de sa force ascensionnelle. Le procédé est équivalent à une ascension de ballons de caoutchouc avec un lance-ballast négatif, ou avec une charge croissant avec l'altitude. Ou encore, à une ascension d'un ballon de Polythène avec suppression constante d'une fraction choisie de son poids total et de sa charge.

Il faut naturellement prévoir au départ la force ascensionnelle nette F_c des ballons de caoutchouc pour qu'elle ne suffise pas à supporter le poids P du reste de la charge y compris le ballon de Polythène supposé vide, sinon l'ascension ralentit une fois que celui-ci a pris forme, mais ne s'arrête pas avant qu'un ballon

[1] *Manuscrit reçu le 24 septembre, 1952.*
Contribution de l'Institut de Physique, Université de Montréal, Montreal, Que.

de caoutchouc ait crevé. Au moment du plafonnement, il faut que le ballon de Polythène ait à contribuer une force ascensionnelle F_p positive:

$$F_p = P - F_c.$$

F_p est proportionnelle à la pression au moment du plafonnement. Il faut en outre que l'altitude du plafonnement soit inférieure à l'altitude d'éclatement des ballons de caoutchouc dans l'état de gonflement qu'on leur a imposé. Pour un plafonnement à l'altitude maximum, il faut les gonfler peu, en mettre plusieurs et avoir une faible valeur de F_p. Le lancement du système peut se faire à une grande vitesse ascensionnelle, le ballon de Polythène pouvant être fortement gonflé puisque F_p ne dépend pas de son gonflement initial.

Les ballons de Caoutchouc J8-800 Darex chauffés dans l'eau à 60°C. pendant cinq minutes ont été gonflés à l'hydrogène jusqu'à ce qu'ils tirent à leur base avec

FIG. 1. Du haut en bas, cinq ballons de caoutchouc peu gonflés, un ballon de Polythène, queue de gaze, nacelle et baromètre enregistreur, aspect au départ. Approximativement à l'échelle.

une force nette de 700 à 800 gr. en général, l'altitude d'éclatement étant alors environ 37 km. Ces ballons étaient attachés par des rubans Padoue, (voir Fig. 1), grâce à une patte à cinq doigts en même ruban, collée avec du ruban type Durex, au sommet d'un ballon de Polythène de 10 fuseaux, préparé au laboratoire, et gonflé ensuite, par les procédés déjà décrits (3). Le ballon de Polythène était

gonflé de façon à assurer une force nette au départ de 1 à 3 kg. Une grande queue en gaze surmontait la nacelle pour éviter les oscillations. Le départ a eu lieu de l'Université de Montréal.

3. RÉSULTATS

Sur six ascensions, trois ont été retrouvées, et permettent les conclusions suivantes, en partie décrites dans la liste que voici:

	No 1	No 2	No 3
Date	7 VII 52	17 VII 52	7 VIII 52
Lieu d'atterrissage	Glen Buell, Ont.	Pierreville, Qué.	Courcelles, Qué.
Distance de Montréal	205 km. O.S.O.	91 km. N.E.	208 km. E. par E.N.E.
Nombre de ballons de caoutchouc	2	4	5
Poids sous les ballons de caoutchouc	3900 gr.	4150	4150
F_c, force nette des ballons de caoutchouc	1700	2950	3600
F_p, contribution du ballon de Polythène au moment du plafonnement	2200	1200	550
Altitude et pression prévues	28.1 km. 0.0163 atm.	31.8 0.0089	36.4 0.0041
Altitude et pression atteintes	22.1 km. 0.04 atm.	26.6 0.02	31.1 0.01
Départ	10 h. 30 H.A.E.	10 h. 05	10 h. 16
Arrivée	23–24 h. environ	23 h. 10	23 h. 40
Durée du vol	13 h. environ	12 h. 05	13 h. 24
Coucher du soleil au sol et fin du crépuscule à Montréal	20 h. 47 23 h. 36	20 h. 41 23 h. 14	20 h. 15 22 h. 24

La pression a été déterminée par un baromètre à minimum du type imaginé par Piccard. Des tubes de verre fermés dans le haut laissant échapper l'air qu'ils contiennent au cours de la montée par le bas qui plonge dans de l'huile pour pompe à vide. A la descente l'huile remplit les tubes sauf une petite bulle renfermant l'air résiduel, dont la longueur est proportionnelle à la pression minimum. D'après notre expérience de cet appareil très simple, dans d'autres ascensions, la pression minimum trouvée peut être trop faible d'environ 0.005 atm. Nous avons négligé cette erreur dans l'évaluation de la pression atteinte, l'altitude réellement atteinte est probablement légèrement inférieure à celle indiquée. Les observations faites sur les émulsions portées dans ces ascensions, en particulier sur les noyaux lourds, confirment les altitudes indiquées.

Le système atteint son plafond en 1h.$\frac{1}{2}$ à 2h.$\frac{1}{2}$, d'après l'observation au théodolite du No 1. Son équilibre est ensuite très stable et évidemment le coucher du soleil seul le fait descendre en le refroidissant. Le coucher du soleil a lieu à ces altitudes près d'une heure plus tard qu'au sol, soit environ à 9 h.30 au lieu de 8 h.30, et la descente prend environ deux heures. On dispose donc ainsi d'un moyen très sûr d'obtenir un plafonnement d'environ neuf heures ou davantage si le lancement est fait plus tôt, à une altitude réglable, sans avoir à manipuler un très grand ballon de Polythène.

L'altitude atteinte est notablement inférieure à la prévision théorique. Les pertes de gaz par des trous ou à travers les surfaces ne peuvent expliquer ce fait, puisque si elles suffisaient à abaisser le plafond, elles abrégeraient aussi le vol. Après considération des facteurs mis en jeu, l'explication paraît être la suivante:

le ballon de Polythène acquiert sensiblement son volume maximum quand il prend forme, mais il ne garde pas sa forme pleine aux très basses pressions où il est entraîné, par suite de la réduction des tensions transversales de l'enveloppe. La tension verticale qui lui est imposée par les ballons accrochés à son sommet, et par la charge à sa base, contribue à lui donner une forme étirée. Un remède partiel serait de soutenir le ballon de Polythène par le haut, et la charge par une corde de longueur appropriée le traversant.

4. VENTS DANS LA STRATOSPHÈRE

Une remarque concerne le lieu d'atterrissage. Le vent entre 0 et 10 km. d'altitude avait une composante vers l'est, comme les vents de surface dominants, et une allure de l'ordre de 40 km. par heure. La proximité du lieu d'atterrissage et sa position suggèrent fortement que les vents au cours du plafonnement présentaient une inversion, i.e., étaient dirigés vers l'ouest, d'accord avec une étude bibliographique aimablement préparée par M. D. P. McIntyre. Selon lui, les vents stratosphériques au-dessus de Montréal vont surtout vers l'est en hiver et surtout vers l'ouest en été. De plus l'ascension No 1 a permis d'observer cette inversion, elle est partie vers le N.N.E. puis est revenue exactement au zénith après 101 min., puis est disparue à l'ouest après 150 min.

Ces expériences avaient pour but d'irradier des émulsions photographiques orientées au cours du vol, leurs résultats seront décrits en détail plus tard. Voir aussi (1, 2, 4, 5, 6).

5. REMERCIEMENTS

Je remercie M. D. P. McIntyre du Service de Météorologie du Ministère du Transport du Canada à Toronto, pour les renseignements communiqués; M. Andrew Thomson, directeur du même service, pour l'intérêt témoigné; Mlle Simone Kittel, M. Réal Courtemanche, Mlle Pauline Cartier, pour leur aide dans la préparation des ascensions; le Conseil National des Recherches et la Compagnie Canadian Industries Limitée, pour des octrois qui ont permis ce travail.

SUMMARY

A simple procedure is described, combining the use of closed rubber balloons with that of an open Polythene balloon of medium size, which has allowed us to keep cosmic ray sensitive emulsions for 9 to 10 hr. at a ceiling of 24 to 32 km.

BIBLIOGRAPHIE

1. DEMERS, P. Can. J. Research, A, 25: 223. 1947.
2. DEMERS, P. et COURTEMANCHE, R. Ann. ACFAS, 18: 120. 1952.
3. DEMERS, P. et DE GRANDPRÉ, J.-L. Can. J. Phys. 30: 235. 1952.
4. DEMERS, P., LAMARCHE, G. et COURTEMANCHE, R. Compt. rend. 231: 651. 1950.
5. DEMERS, P. et LECHNO-WASIUTYNSKA, Z. Compt. rend. 235: 474. 1952.
6. HEBERT, J. Ann. ACFAS, 18: 119. 1952.

TEMPERATURE-PRESSURE HYPOTHESIS AND THE EARTH'S INTERIOR[1]

By J. A. Jacobs

ABSTRACT

Bullen and Ramsey have shown that the reciprocal of the compressibility is a linear function of the pressure both in the Earth's core and in the mantle below 1000 km. In view of this result, it seems reasonable to suppose that a similar relationship exists between the reciprocal of the volume coefficient of thermal expansion and pressure. Support for this hypothesis is obtained by two independent methods (*a*) using Uffen's results based on the theory of solids, (*b*) using Murnaghan's theory of finite strain. Assuming the validity of the hypothesis, an estimate is made of the adiabatic gradient throughout the Earth. Taking the temperature at 1000 km. to be 3600° K., values of the temperature at greater depths are estimated. In particular it is found that the temperature at the boundary of the core is 4350°K., and at the center of the Earth a little over 4800°K. These results have considerable interest and bearing on Bullard's theory of the transfer of heat from the core.

1. INTRODUCTION

From a detailed analysis of seismic data, Bullen (4, 5) has derived both the density ρ and the adiabatic compressibility β of the Earth as functions of depth. In later papers (6, 7) he found empirically that the adiabatic incompressibility k, which is the reciprocal of β, is a linear function of the pressure p viz.

$$k = k_0 + ap. \tag{1.1}$$

This relation was found to be valid both in the core and in the surrounding mantle below a depth of 1000 km. Ramsey (10, 11, 12) has re-examined this relation from the point of view of the theory of solids, and his conclusions point to the validity of equation [1.1]. He found, however, that the constant k_0 had different values in the core and mantle, although the derivative $dk/dp = a$ was essentially the same. In a more recent and comprehensive paper on the constitution of the Earth's interior, Birch (1) disagrees with the work of Bullen and Ramsey, and regards the relationship [1.1] as at best approximately valid over limited ranges of pressure for the particular materials of the Earth's interior. It is the purpose of this paper to try to obtain some information on the behavior of the thermodynamic coefficients with increasing depth and hence to make an estimate of the temperature distribution in the Earth. In view of equation [1.1], it seems reasonable to suppose that a similar relationship exists between the volume coefficient of thermal expansion α and pressure p, viz. that the reciprocal of α is a linear function of p

$$\frac{1}{\alpha} = \text{const.} + bp = C + bp. \tag{1.2}$$

Birch himself (1) has pointed out the importance of the thermal expansion in a number of geophysical problems, and little attention has been given to the question of the change of α with pressure. Experimental data are scanty and subject to relatively large uncertainties.

[1] *Manuscript received October 14, 1952.*
Contribution from the Geophysics Laboratory, University of Toronto, Toronto, Ontario.

It is because of this lack of data that the possibility of a relationship [1.2] is investigated, in spite of Birch's objections to [1.1]. It will be shown that excellent support may be obtained for the temperature–pressure hypothesis [1.2], and although it is not suggested that it is a fundamental physical law, it is nevertheless a good approximation over large ranges of pressure and should give an indication of the variation of α in the Earth's interior—at least below 1000 km.

2. ANALYSIS OF THE TEMPERATURE–PRESSURE HYPOTHESIS

In a recent investigation on the thermal properties of the Earth (based on the theory of solids), Uffen (13) has obtained values of α within the mantle. These are reproduced in Table I. In Fig. 1, $1/\alpha$ is plotted against p, and it can

TABLE I

VALUES OF α IN THE MANTLE (AFTER UFFEN)

Depth, km.	α (°K.)$^{-1}$	$1/\alpha$, °K.
200	36×10^{-6}	2.78×10^{4}
600	28	3.57
1000	20	5.00
1400	17	5.88
1800	14	7.14
2200	12	8.34
2600	10	10.00
2900	9	11.11

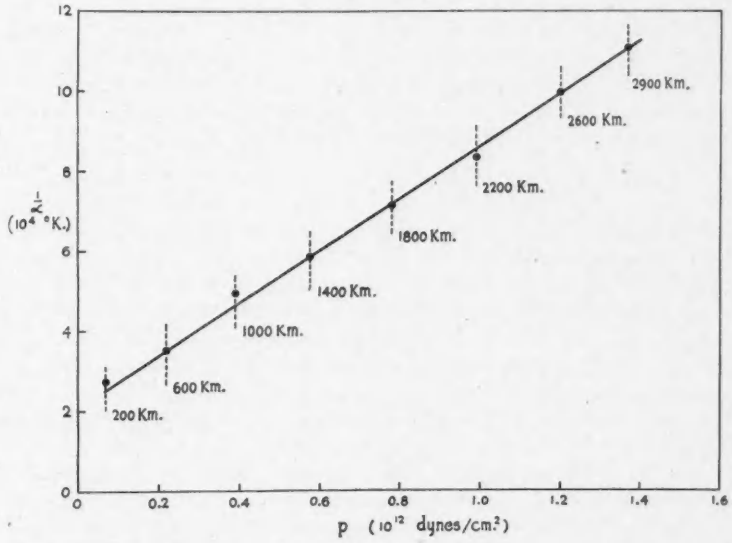

FIG. 1. The reciprocal of the volume coefficient of thermal expansion as a function of the pressure in the mantle.

be seen that these results lend support to the hypothesis [1.2]. An alternative method was sought to corroborate this result if possible—this was made possible using Murnaghan's (9) theory of finite strain. Birch (1) has used the same theory to obtain many of his results. Values of α are calculated from the equation

$$[2.1] \qquad \alpha = \frac{\gamma \rho c_v}{k}$$

where γ is Grüneisen's ratio and c_v the specific heat at constant volume. We assume that we can neglect any changes in c_v—a fact which is substantiated by the work of Uffen and Birch (*ibid.* 13, 1).

Then $\dfrac{\alpha}{\alpha_0} = \dfrac{\gamma}{\gamma_0}\dfrac{\rho}{\rho_0}\dfrac{k_0}{k}$, where the suffix 0 refers to zero pressure. From Murnaghan's theory, we can obtain expressions for ρ, k_T, and p in terms of the strain ϵ or compression f, where we write $f = -\epsilon$, a more convenient variable for compression. We have (see, for example, Birch (1), equation (15))

$$[2.2] \quad \begin{cases} p = 3k_0 f\,(1+2f)^{5/2}\,(1-2\xi f), \\ \left(\dfrac{\partial k_T}{\partial p}\right)_T = [12 + 49f - 2\xi(2 + 32f + 81f^2)]/3[1 + 7f - 2\xi f(2 + 9f)], \\ k_T/\rho = k_0/\rho_0\,.\,(1+2f)\,[1 + 7f - 2\xi f\,(2 + 9f)], \\ \rho/\rho_0 = (1+2f)^{3/2}. \end{cases}$$

These equations which are for isothermal compression express the pressure p and the ratio k_T/ρ in terms of one parameter ξ. ξ depends on third order terms in the expansion of the Helmholtz free energy, i.e. in this case the strain energy, as a Taylor series in the strains. k_0 and ξ are functions of the temperature alone. The latest experimental work of Bridgman (2) shows that there is likely to be little error in taking ξ to have its most probable value, viz. zero. To obtain values of γ, we use equation 18 (Birch (1)), viz.

$$[2.3] \qquad \gamma = -\frac{1}{6} + \frac{1}{2}\frac{d \log k}{d \log \rho} - \frac{3}{2}\rho \frac{d\sigma}{d\rho}\left[(1-2\sigma)(1+\sigma)\right]^{-1}$$

which is obtained from Debye's theory of the thermal expansion of solids. Little is known of the variation of Poisson's ratio σ with ρ, but by plotting σ against depth (found from seismic data), the graph is approximately linear between about 1000 and 2600 km. In this range σ increases by about 0.024 and ρ by 0.86. We thus take $d\sigma/d\rho$ to be approximately constant at a value of 0.0279. The initial value of γ is taken as 1.5. Finally $d \log k/d \log \rho \simeq (\partial k_T/\partial p)_T$, so that we can construct Table II.

Values of f are calculated from the depth on the assumption that the compression is adiabatic.

The values of α_0/α obtained in Table II merely reflect the changes in α due to compression and do not take into account the effect of temperature changes, since we have used the isothermal incompressibility k_T instead of the adiabatic incompressibility k. The effects of temperature will, however, be small compared to those of pressure.

TABLE II

CHANGE OF GRÜNEISEN'S RATIO AND THERMAL EXPANSION WITH COMPRESSION (USING MURNAGHAN'S THEORY OF FINITE STRAIN)

Depth, km.	f	p/k_0	γ/γ_0	$\rho k_0/\rho_0 k$	α_0/α
1000	0.0490	0.186	0.851	.678	1.735
1200	0.0590	0.234	0.823	.632	1.920
1400	0.0688	0.285	0.797	.593	2.110
1600	0.0775	0.333	0.773	.561	2.305
1800	0.0853	0.380	0.752	.534	2.490
2000	0.0930	0.428	0.731	.512	2.675
2200	0.1007	0.478	0.714	.488	2.865
2400	0.1088	0.534	0.691	.467	3.100
2600	0.1167	0.592	0.676	.447	3.310
2800	0.1271	0.672	0.659	.422	3.595

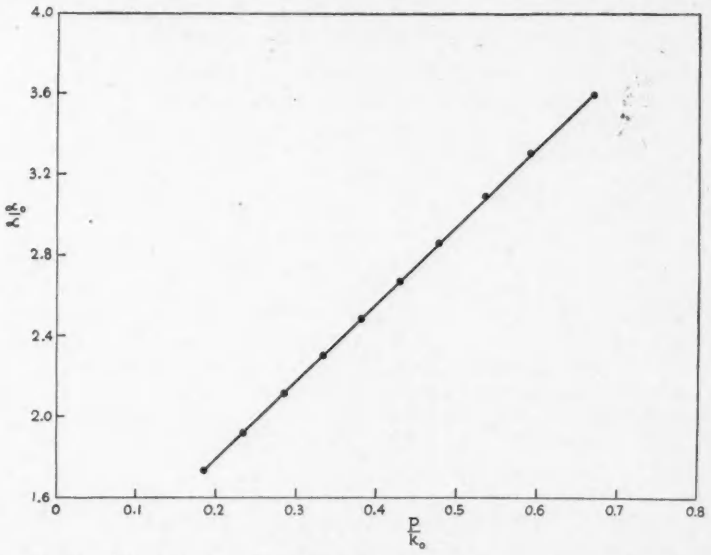

FIG. 2. The reciprocal of the volume coefficient of thermal expansion as a function of the pressure in the mantle.

Fig. 2 shows α_0/α plotted against p/k_0 and again excellent agreement is found with the linear hypothesis expressed in equation [1.2]. Using Uffen's values for α, we have from Fig. 1,

$$[2.4] \qquad \begin{cases} C = 2.4 \times 10^4 \text{ °K.}, \\ b = 6.2 \times 10^{-8} \text{ °K. cm.}^2 \text{ per dyne.} \end{cases}$$

Using Murnaghan's theory of finite strain, we have from Fig. 2

$$\frac{\alpha_0}{\alpha} = 1 + 3.92 \frac{p}{k_0},$$

[2.5] $$\text{i.e. } \frac{1}{\alpha} = \frac{1}{\alpha_0} + \frac{3.92}{\alpha_0 k_0} p.$$

Values of α_0 and k_0 are not easy to estimate precisely. Using Birch's (1) figures, we can take $\alpha_0 = 36 \times 10^{-6}$ (°K.)$^{-1}$, $k_0 = 2 \times 10^{12}$ dynes per cm.^{2} With these values, equation [2.5] can be written

$$\frac{1}{\alpha} = C + bp \text{ where}$$

[2.6] $$\begin{cases} C = 2.78 \times 10^4 \text{ °K.}, \\ b = 5.45 \times 10^{-8} \text{ °K. cm.}^2 \text{ per dyne.} \end{cases}$$

The agreement between [2.4] and [2.6] is considered good enough in view of the approximations in the theory and in the uncertainties in some of the elastic and thermal coefficients.

3. THE ADIABATIC TEMPERATURE GRADIENT

It is now possible to make an estimate of the adiabatic temperature gradient throughout the Earth. The adiabatic gradient may be written

[3.1] $$\frac{dT}{dp} = \frac{\alpha T}{\rho c_p}$$

where c_p is the specific heat at constant pressure. From [1.2] and [3.1], we may write

[3.2] $$\frac{dT}{T} = \frac{dp}{\rho\, c_p\, (C + bp)}.$$

Both Uffen (13) and Verhoogen (15) have obtained values of the ratio α/c_p in the mantle using seismic data. Uffen found that the values of c_p were approximately constant (in agreement with Bridgman's observations at relatively low pressures), and that the variations in α/c_p were almost entirely due to variations in α. Assuming that we can take c_p as constant, we have from [3.2]

[3.3] $$\log_e T = \frac{1}{c_p} \int \frac{dp}{\rho\, (C + bp)}.$$

It is estimated that variations in c_p will not affect the validity of [3.3] by more than 7% if the temperature rise is adiabatic. Since ρ is known as a function of depth (and hence of pressure), equation [3.3] can be integrated numerically. The values of C and b were taken from equation [2.4]. In order to obtain a numerical value for T at any depth, its value at some depth must be known. Taking T at 1000 km. to be 3600°K. (Uffen (13)), values of T can be estimated at greater depths. In particular the temperature at the boundary of the core and mantle is found to be 4350°K.

If we assume in addition that the relationship [1.2] is also valid in the core as Bullen postulated [1.1] to be, then we can integrate equation [3.2] throughout the core as well. It is found that the temperature at the center of the Earth is a little over 4800°K. The increase throughout the core is thus only 500°. The results of the integration are presented graphically in Fig. 3. We thus find that

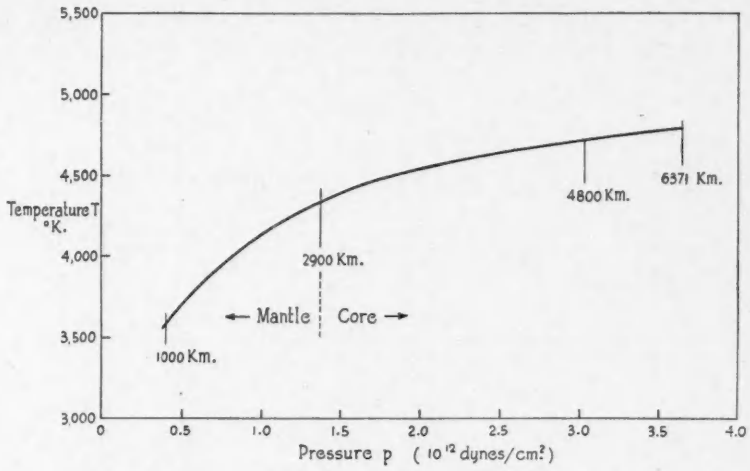

FIG. 3. Temperature distribution below 1000 km.

the temperature at the center of the Earth is of the order of 5000°K. rather than the accepted value of about 10,000°K. Valle (14) has also obtained values of the ratio α/c_p in the mantle using seismic data, and has calculated the adiabatic variation of the ratio of the temperature at any depth in the mantle to the temperature at 33 km. He has extended his theory to the core to obtain values of the ratio of the temperature at any depth in the core to its value at the boundary of the core and mantle. He obtains over 30% increase in the temperature at points halfway across the core which seems very excessive.

4. CONCLUSIONS

Bullard (3) and Elsasser (8) have considered the question of the transfer of heat from the core and examined the possibility of convection currents. Bullard found that the heat flow required to maintain convection currents was about four times greater than that available from a core with a radioactive content comparable with that of iron meteorites. He used a temperature of 10,000° in his calculation of the adiabatic gradient, and a value of 5000° would thus reduce his discrepancy by a half. Moreover, Bullard used the value of 1.6 for γ in his estimation of α. Both Uffen's work and the above analysis based on the theory of finite strain show that γ decreases with depth so that Bullard's value of 1.6 is too high. The value of γ is more likely to be about 0.8, and this would remove any discrepancy in Bullard's estimate of the heat flow.

In conclusion it must be emphasized that no physical proof of the validity of the relation [1.2] throughout the Earth's interior has been given. Two independent analyses however agree in suggesting that it may be a very fair approximation to the truth—at any rate in the mantle below 1000 km. In view of the scarcity of data on this question, the results of this paper should be of value in giving at least some indication of the behavior of α and γ with pressure.

ACKNOWLEDGMENTS

The author is indebted to the National Research Council which sponsored the present work.

REFERENCES

1. BIRCH, F. J. Geophys. Research, 57: 227. 1952.
2. BRIDGMAN, P. W. Proc. Am. Acad. Arts Sci. 76: 55. 1948.
3. BULLARD, E. C. Monthly Notices Roy. Astron. Soc., Geophys. Suppl. 6: 36. 1950.
4. BULLEN, K. E. Bull. Seismol. Soc. Am. 30: 235. 1940.
5. BULLEN, K. E. Bull. Seismol. Soc. Am. 32: 19. 1942.
6. BULLEN, K. E. Monthly Notices Roy. Astron. Soc., Geophys. Suppl. 5: 335. 1949.
7. BULLEN, K. E. Monthly Notices Roy. Astron. Soc., Geophys. Suppl. 6: 50. 1950.
8. ELSASSER, W. M. Trans. Am. Geophys. Union, 31: 454. 1950.
9. MURNAGHAN, F. D. Am. J. Math. 59: 235. 1937.
10. RAMSEY, W. H. Monthly Notices Roy. Astron. Soc. 108: 406. 1948.
11. RAMSEY, W. H. Monthly Notices Roy. Astron. Soc., Geophys. Suppl. 5: 409. 1949.
12. RAMSEY, W. H. Monthly Notices Roy. Astron. Soc., Geophys. Suppl. 6: 42. 1950.
13. UFFEN, R. J. Ph.D. Thesis, University of Western Ontario, London, Ont. 1952.
14. VALLE, P. E. Ann. Geofis. 5: 41. 1952.
15. VERHOOGEN, J. Trans. Am. Geophys. Union, 32: 41. 1951.

A DETERMINATION OF THE HALF LIVES OF SOME MAGNETIC DIPOLE γ-RAY TRANSITIONS[1]

By R. L. Graham and R. E. Bell

ABSTRACT

A number of magnetic dipole γ-ray transitions have been studied using a coincidence circuit of short resolving time ($2\tau_0 = 2 \times 10^{-9}$ sec.), a two lens single β-ray spectrometer, a pair of lens spectrometers placed end to end with coincidence counting of the focused radiations from a single source, and a scintillation spectrometer. Lifetimes have been measured using the delayed coincidence method and where feasible conversion coefficients and K/L ratios obtained. Comparison is made with theoretical estimates of the lifetime–energy relation for $M1$ γ-ray transitions.

The new results are as follows:

Nucleus	γ-Ray energy, kev.	Half life, sec.	α_K	K/L
Te^{123}	159	$(1.9 \pm 0.3) \times 10^{-10}$	—	—
Te^{125}	35.4	$(1.58 \pm 0.15) \times 10^{-9}$	—	—
Cs^{133}	81	$(6.0 \pm 0.4) \times 10^{-9}$	1.77	7.5
Cs^{135}	248	$(2.8 \pm 0.8) \times 10^{-10}$	—	7.0
Pm^{147}	91.5	$(2.44 \pm 0.08) \times 10^{-9}$	1.8	7.3
Tl^{208} (ThC″)	40 (A line)	$< 7 \times 10^{-11}$	—	—
Bi^{212} (ThC)	238 (F line)	$< 2 \times 10^{-11}$	—	—

I. INTRODUCTION

Upper limits have been reported for the lifetimes of a number of magnetic dipole, $M1$, γ-ray transitions (31) but until now actual lifetimes have been determined for only three $M1$ γ transitions. These are the 478 kev. transition in Li^7 with $T_{1/2} = (5.2 \pm 1.7) \times 10^{-14}$ sec. (12), the 14 kev. transition in Fe^{57} with $T_{1/2} = 1.1 \times 10^{-7}$ sec. (9), and the 80 kev. transition in Xe^{131} with $T_{1/2} = (4.8 \pm 2.0) \times 10^{-10}$ sec. (17).

This paper reports the results of experiments on seven other $M1$ transitions, five of which were found to have measurable half lives. Where the multipolarity was uncertain assignment has been made by one or more of the following methods: (a) comparison of the experimental K conversion coefficients with the theoretical values deduced from the calculated values of Rose *et al.* (30) and Spinrad and Keller (35), (b) comparison of the experimental K/L ratio of conversion coefficients with empirical curves of Goldhaber and Sunyar (16), (c) comparison of the experimental L_I: L_{II}: L_{III} conversion coefficient ratios with the theoretical values calculated by Gellman *et al.* (15) which have been verified in part experimentally by Mihelich and Church for γ-rays of known multipolarity (26, 27). The delayed coincidence method of measuring short half lives is reviewed. It is seen that scintillation counters employing fast organic phosphors and recently developed delayed coincidence techniques make it possible, under favorable circumstances, to measure lifetimes as short as 10^{-10} sec. with some accuracy and to set upper limits of $\sim 10^{-11}$ sec. thus bringing many $M1$ transitions within range of experimental detection.

[1] *Manuscript received October 10, 1952.*
Contribution from Physics Division, Atomic Energy of Canada Limited, Chalk River, Ontario. Issued as A.E.C.L. No. 11.

The experimental half lives of $M1$ transitions in odd A nuclei are $\sim$ 100 times longer than those predicted theoretically for "allowed" transitions and appear to be slightly longer for odd proton nuclei than odd neutron nuclei. The discrepancy between theoretical and experimental lifetimes of "forbidden" $M1$ transitions ($\Delta l = 2$ in shell model orbital assignment) in heavy odd neutron nuclei has been used by Sachs and Ross (31, 33) to provide evidence for the nonadditivity of nucleon moments and the existence of exchange moments.

II. METHOD

The measurement of short half-lives by the delayed coincidence method has been discussed fully in earlier publications (3, 17). When the lifetime is long compared to the resolving time of the coincidence circuit, the half-life $T_{1/2}$ may be deduced most accurately from the slope of the tail of the coincidence resolution curve $F(x)$ plotted on a logarithmic scale, where x is the artificially inserted delay time. When the lifetime is short compared to the resolving time, the shift of the centroid of the delayed resolution curve $F(x)$, with respect to that of a "prompt" curve, $P(x)$, is a direct measure of the mean life, τ, and may be determined from the experimental data by the methods of Bay (1) and Newton (28). Radiations are considered to be "prompt" if their lifetimes are too short to be measured by the delayed coincidence technique.

For the shortest lifetimes it is often convenient to use the more sensitive "self comparison" method in which the delayed resolution curve $F(x)$ is compared with its own inverse $F(-x)$. This method was first used (17) to place an upper limit on the lifetime of the 411 kev. excited state in Hg^{198} and is briefly as follows: A radioactive source of strength 10 to 100 μc. is placed at the center of the pair of β-ray spectrometers mentioned below. The delayed curve $F(x)$ is then obtained with the conversion line of the γ-ray transition focused in one, the north, spectrometer and a point on the β-ray spectrum just below the line focused in the other, the south, spectrometer. The inverse curve $F(-x)$ is obtained by increasing the currents in both spectrometers slightly so that the north spectrometer focuses on the β spectrum just above the line while the south focuses on the line. Among the advantages of this method are (1) it doubles the effect (the shift of the centroids of the two resolution curves is then $2\tau = 2.89\ T_{1/2}$), (2) it cancels out systematic errors, and (3) it eliminates the need for obtaining the prompt resolution curve.

III. APPARATUS

In most of the investigations described below the radiations were selected magnetically in a pair of identical lens β-ray spectrometers placed end-to-end, which have a common vacuum chamber (2, 18). This apparatus is quite flexible; with the source at the center and the two coils excited separately, radiations of different energies can be focused simultaneously on the stilbene-1P21 scintillation counters at either end of the vacuum chamber. With the source at one end, the coils connected in series, and a change in the baffle system it behaves as a single, two-lens β-ray spectrometer, focusing radiations on one counter only. As described elsewhere (2) the current in one or both coils can be made to assume

up to 35 different fixed values successively by means of a stepping switch control which may be operated automatically.

The scintillation counters were connected to a coincidence circuit (3, 4) whose resolving time, $2\tau_0$, can be varied down to 2×10^{-9} sec. or less without reducing the coincidence efficiency below 0.9. Artificial time delays were inserted between both counters and the coincidence mixer by means of the motor driven helical delay unit described in an earlier publication (3).

Almost all of the data in these experiments were recorded on Esterline Angus charts (2). A timing switch was connected to the delay unit to change the inserted delay every 10 min. After counting had proceeded for 10 min. at each of the chosen delay settings the delay unit reset itself automatically and repeated the sequence in the same order. A switch actuated by the delay unit drive mechanism and connected to the current stepping control allowed the current setting to be changed while resetting the delay unit. This was used in the self comparison determinations to rock the current back and forth after each sweep of a resolution curve.

A scintillation γ-ray spectrometer consisting of a 1 in. dia. by 1 in. NaI (Tl) crystal, a 5819 photomultiplier, and a single channel pulse height analyzer was used to measure the K conversion coefficient in two cases.

IV. ERRORS

The accuracy with which short half lives can be measured is limited by the statistics and also by certain systematic effects not all of which are completely amenable to calculation. The propagation velocity in the air spaced coaxial transmission line in the helical delay unit is very nearly that of light. A slight reduction of velocity due to the presence of the Lucite pegs supporting the central conductor is calculated to be 1%. Inaccuracies in calibration due to the mechanical dimensions of the delay unit are estimated to be less than 1% and due to the uncertainty in positioning the movable carriage less than 10^{-12} sec. The average time interval, $\bar{t}$, between the excitation of the phosphor and the emission of the first photoelectron from the photomultiplier cathode is dependent upon the energy E (kev.) of the incident electron expended in the phosphor (29). With trans stilbene as a phosphor and fairly energetic electrons we expect (3) for our counters $\bar{t} \sim (3/E) \times 10^{-8}$ sec. $\bar{t}$ is measured experimentally as the reciprocal of the slope of the sides of a prompt resolution curve plotted on a logarithmic scale and is found experimentally to be of the order estimated above indicating that the circuit responds to the first photoelectron. Corrections due to variations in $\bar{t}$ are avoided wherever possible by comparing delayed and prompt radiations of the same energy. In the case of the self comparison method the changes in $\bar{t}$ in the two counters roughly cancel since the energies of the radiations focused are increased by approximately the same small amount. For the highest accuracy, however, it is necessary to make second order corrections if the $\bar{t}$'s for the two counters are different and errors of $\sim 10^{-11}$ sec. or greater may arise. Transit time of the electrons in the spectrometer must also be considered when the current is changed in making a comparison. Since the momentum (and hence velocity) of the electrons being focused and their path

length are known this correction can be made with an accuracy usually better than 10^{-11} sec. In order to minimize errors due to other effects such as slow drift in photomultiplier characteristics and thermal changes, comparisons were made as close in time as possible. In self comparison experiments the runs were sandwiched so that these corrections would tend to cancel out. With these precautions using the self comparison method it would seem possible to set limits as small as a few times 10^{-11} sec. on lifetimes and to measure lifetimes with standard deviations of $\sim 10^{-11}$ sec. if the statistical accuracy is sufficiently good. The errors assigned to lifetimes determined by a centroid shift analysis are the combined standard deviations due to (*a*) statistics, (*b*) corrections in $\bar{t}$ whose error is estimated from the standard deviations of the points on the side of the resolution curve from which $\bar{t}$ is measured, (*c*) slow drifts in time as measured by the shift of the centroid of a particular resolution curve from day to day, and (*d*) uncertainty in the spectrometer transit time correction which is appreciable only for low electron energies. The upper limits on lifetimes quoted below are taken to be twice the total combined errors described above.

V. RESULTS

(*a*) *Te^{123}, 159 Kev. γ-Ray Transition*

The 159 kev. γ-ray transition in Te^{123} has been shown to follow the 90 day, 88.5 kev. γ-ray transition in Te^{123} by Katz, Hill, and Goldhaber (20) and has been classified as $M1$ radiation (shell model orbital $d_{3/2} \rightarrow s_{1/2}$) on the basis of its conversion coefficient and K/L ratio (19, 20). Deutsch and Wright (10) found the half life to be $< 4 \times 10^{-9}$ sec. and McGowan found it to be $< 10^{-9}$ sec. (24).

A source of neutron irradiated Te of strength $\sim 20\mu$c. was placed at the center of the pair of β-ray spectrometers. With the K 88.5 line focused in the north spectrometer and the K 159 line focused in the south spectrometer the coincidence resolution curve $F(x)$ in Fig. 1 was obtained. Two prompt comparisons were made using sources of thorium active deposit. The thorium F line transition is shown below to have a half life $T_{1/2} < 2 \times 10^{-11}$ sec. In one comparison, no changes were made in spectrometer currents so that the north spectrometer focused β-rays from ThB and the south spectrometer focused the F line which was degraded by an Al absorber placed over the source so that it corresponded in energy to the K 159 line. The results are shown as the prompt resolution curve $P(x)$ in Fig. 1. In the other case the F line was not degraded and the south spectrometer current was raised to bring the F line into focus. The centroid of the resolution curve obtained in the second case (not shown) was found to agree within the limits of statistical accuracy with that of the first comparison after correcting for the changes in transit time in the south spectrometer and in $\bar{t}$ in the south counter. The shift between the centroid of $F(x)$ and a weighted average of the two centroid determinations for $P(x)$ gives for the mean life of the 159 kev. γ-ray transition in Te^{123}, $\tau = (2.7 \pm 0.3) \times 10^{-10}$ sec. The total error in the mean life including the uncertainty in the mean life of the F line transition ($\sim 3 \times 10^{-11}$ sec.) and drift of the centroid of the

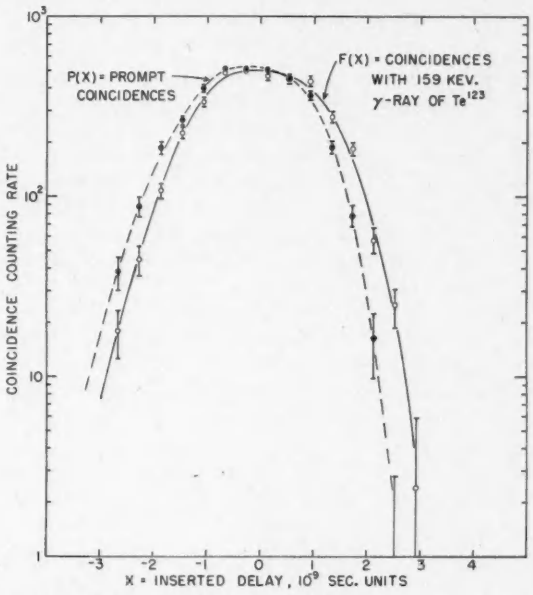
P(X) = PROMPT COINCIDENCES
F(X) = COINCIDENCES WITH 159 KEV. γ-RAY OF Te123
COINCIDENCE COUNTING RATE
X = INSERTED DELAY, 10⁻⁹ SEC. UNITS

FIG. 1. Delayed resolution curve $F(x)$ for the 159 kev. γ-ray transition of Te^{123} with a prompt curve $P(x)$ for comparison. The half life of this transition is measured by the shift of the centroid of $F(x)$ to the right. The result is $T_{1/2} = (1.9 \pm 0.3) \times 10^{-10}$ sec. The standard deviations of the points are shown by vertical bars.

resolution curves with time ($\sim 2 \times 10^{-11}$ sec. per day) is $\sim 4.7 \times 10^{-11}$ sec. Hence we conclude that the half life of the 159 kev. transition in Te^{123} is

$$T_{1/2} = (1.9 \pm 0.3) \times 10^{-10} \text{ sec.}$$

(*b*) *Te^{125} 35.4 Kev. γ-Ray Transition*

The 35.4 kev. γ-ray transition has been shown to follow the 58 day 109.7 kev. γ-ray transition in Te^{125} by Bowe and Scharff-Goldhaber (8) and has been classified as predominantly $M1$ radiation (shell model orbital $d_{3/2} \rightarrow s_{1/2}$) on the basis of its conversion coefficient and K/L ratio by Bowe and Axel (7) and also by Friedlander *et al.* (14). The half life for this transition has been shown to be $< 5 \times 10^{-9}$ sec. by Deutsch and Wright (10) and $< 2 \times 10^{-9}$ sec. by McGowan (24).

The delayed resolution curve $F(x)$ shown in Fig. 2 was obtained using the source mentioned in (*a*) above with the north spectrometer focused on the L 35.4 line and the south spectrometer focused on the L 109.7 line. The prompt resolution curve $P(x)$ shown in Fig. 2 was obtained when the Te source was replaced by a source of ThB and the current in the south spectrometer was increased in order to focus the F line. To improve the signal to noise ratio in the north counter in this experiment the photomultiplier was operated at a

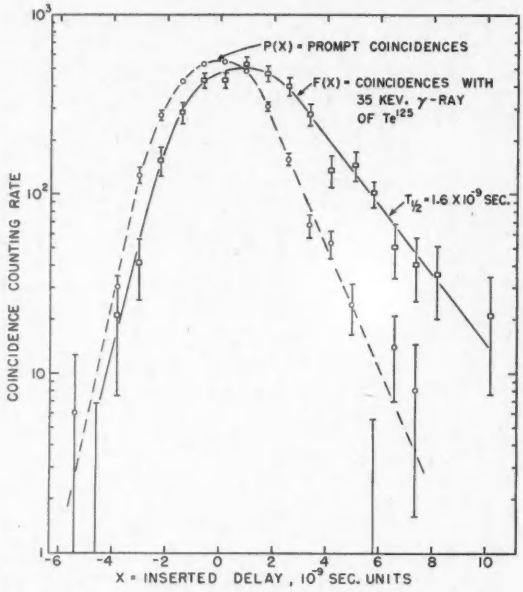
P(X) = PROMPT COINCIDENCES
F(X) = COINCIDENCES WITH 35 KEV. γ-RAY OF Te125
T½ = 1.6 X 10⁻⁹ SEC.
COINCIDENCE COUNTING RATE
X = INSERTED DELAY, 10⁻⁹ SEC. UNITS

FIG. 2. Delayed resolution curve $F(x)$ for the 35.4 kev. γ-ray transition of Te^{125} with a prompt curve $P(x)$ for comparison. The half life of this transition as measured from the shift between the centroids of $F(x)$ and $P(x)$ is $T_{1/2} = (1.58 \pm 0.15) \times 10^{-9}$ sec. The standard deviations of the points are shown by vertical bars.

lower voltage (1200 v.) than is customary (3) and the extra gain required for proper performance of the coincidence circuit was obtained by two wide band (200 Mc. per sec.) amplifiers, each of gain 10, in cascade. The half life for the 35.4 kev. transition as deduced from the slope of the tail of $F(x)$ is $\sim 1.6 \times 10^{-9}$ sec. A centroid analysis of $F(x)$ and $P(x)$ yields, after correcting for the change in transit time and $\bar{t}$ in the south spectrometer, $T_{1/2} = (1.58 \pm .11) \times 10^{-9}$ sec. To allow for the uncertainty in the F line lifetime and a possible error in the $\bar{t}$ correction of $\sim 10^{-10}$ sec. we increase the limits of error and obtain for this transition

$$T_{1/2} = (1.58 \pm 0.15) \times 10^{-9} \text{ sec.}$$

Because of the thick (~ 2 mgm. per cm.^{2}) source used in this experiment the L 35.4 line was not too well resolved in the β-ray spectrum. In order to check that the coincidences were in fact due to this transition the north spectrometer was swept over the region of the L 35.4 line and the line was clearly outlined in coincidence with the L 109.7 line focused in the south spectrometer.

(c) Cs^{133}, 81 Kev. γ-Ray Transition

5.3 day Xe^{133} decays mainly by β^- emission, 745 kev., to an 81 kev. excited state of Cs^{133} (6). The 81 kev. γ-ray transition to the ground state of Cs^{133} has been classified by Bergström and Thulin (6) as a mixture of $M1$ and

$E2$ radiation ($d_{5/2} \rightarrow g_{7/2}$) on the basis of the conversion coefficient, 2.9, and the K/L ratio of 5.9.

As a further check on the multipolarity assignment of this transition the conversion coefficient and K/L ratio were determined using a source of fission product iodine of initial strength $\sim 100\mu$c. which was allowed to stand for some days until 5.3 day Xe^{133} was the predominant activity. By comparing the areas of the ~ 32 kev. K X-ray peak and the 81 kev. γ-ray peak in the scintillation spectrum and making corrections for absorption, escape peaks, and fluorescent yield in the same manner as discussed elsewhere for the 84 kev. γ-ray transition in Yb^{170} (18) we obtain for the K conversion coefficient

$$\alpha_K = 1.77 \pm 0.15.$$

The β-ray spectrum of the source, examined at this time, showed that there was no appreciable contribution to the K X-ray peak in the scintillation spectrum due to internal conversion of other γ-ray transitions in the source. The experimental value of α_K is in good agreement with the theoretical figure for $M1$ radiation of 1.75 obtained by interpolating between the conversion coefficients calculated by Rose *et al.* (30) and the threshold value of Spinrad and Keller (35). The $K/(L + M + N)$ ratio as determined by the areas of the two peaks in the β-ray spectrum (counts/momentum vs. momentum) is 6.0. Assuming that 0.8 of the $L + M + N$ peak is due to L conversion we obtain

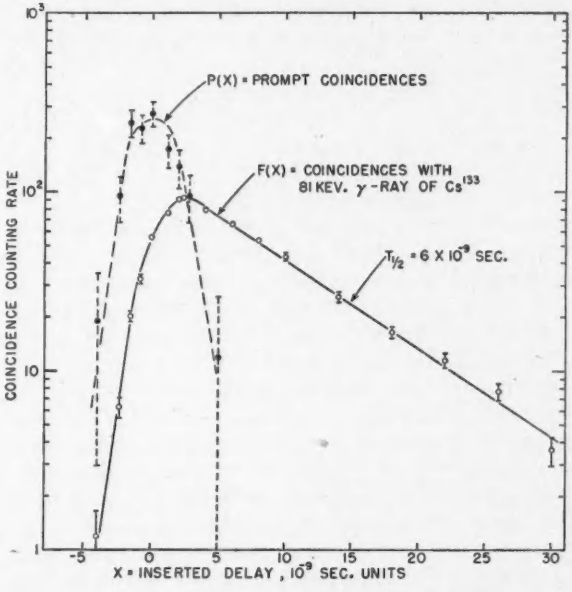

FIG. 3. Delayed resolution curve $F(x)$ for the 81 kev. γ-ray transition of Cs^{133} with a prompt curve $P(x)$ for comparison. From the slope of the tail of $F(x)$ we get for the half life $T_{1/2} = (6.0 \pm 0.4) \times 10^{-9}$ sec. Where the standard deviations of the points are larger than the radii of the circles they are shown by vertical bars.

$K/L = 7.5$ in good agreement with the value of 7.5 predicted by Goldhaber and Sunyar's empirical curve (16) and conclude that the 81 kev. γ-ray transition in Cs^{133} is predominantly $M1$ in character.

In order to measure the lifetime of this transition the source was placed directly over the crystal of the north counter which was covered with a 7 mgm. per cm.^{2} Al absorber to prevent conversion electrons from the 81 kev. γ-ray transition from being counted. The delayed coincidence resolution curve $F(x)$ Fig. 3 was obtained when the $K81$ line was focused on the south counter by the two-lens single spectrometer and only β rays were being counted in the north counter. The prompt curve $P(x)$ shows, on a magnified ($\times$ 60) scale, the results obtained when β rays just above the K 81 line were focused on the south counter. The prompt coincidences observed here are due in part to other prompt radiations of low intensity in the source and in part to electrons back-scattered from the north crystal. From the slope of the tail of $F(x)$ we obtain for the 81 kev. γ-ray transition in Cs^{133}

$$T_{1/2} = (6.0 \pm 0.4) \times 10^{-9} \text{ sec.}$$

This figure was confirmed by another delayed coincidence experiment in which the source was placed directly between the crystals of the two counters which had been removed from the spectrometer.

(*d*) *Cs^{135}, 248 Kev. γ-Ray Transition*

9.2 hour Xe^{135} decays by β^- emission, 905 kev., followed by a 248 kev. γ-ray transition in Cs^{135} (5). No estimates of the multipolarity of this transition have been reported.

The $M1$ character of this transition was deduced by measuring the areas of the K and $L + M + N$ peaks in the same fission product iodine source mentioned in (*c*) above after waiting a few hours to allow Xe^{135} to grow in from the decay of 6.7 hour I^{135}. The ratio of peak areas gives $K/(L + M + N) = 5.6 \pm 1.0$ and hence $K/L = 7.0 \pm 1.2$ if we assume that 0.8 of the $L + M + N$ peak is due to L conversion. This is to be compared with the values of 7.8 and 4.0 expected for $M1$ and $E2$ radiations respectively. No measurement of the conversion coefficient by the scintillation spectrometer method was attempted because of the presence of other γ activities in the source at this time. The experimental K/L ratio indicates that this transition is predominantly $M1$ in character but is not accurate enough to exclude some admixture of $E2$ radiation.

The lifetime of this transition was determined by the self comparison method using the K conversion line. The source was placed 1.5 cm. to the north of the center of the pair of spectrometers whose coils were connected in series. Data were collected over a period of about 60 hr. The delayed resolution curve $F(x)$ in Fig. 4 shows the results obtained when the K 248 conversion line was focused in the south spectrometer and β-rays just below the line were focused in the north spectrometer. The curve $F(-x)$ was obtained with a slightly higher spectrometer current so that the south spectrometer focused β-rays just above the line and the north spectrometer focused the K 248 line. From the shift between the centroids of $F(x)$ and $F(-x)$ we obtain for the mean life $\tau = (4.0 \pm 1.0) \times 10^{-10}$ sec. The estimated error due to differences in transit time

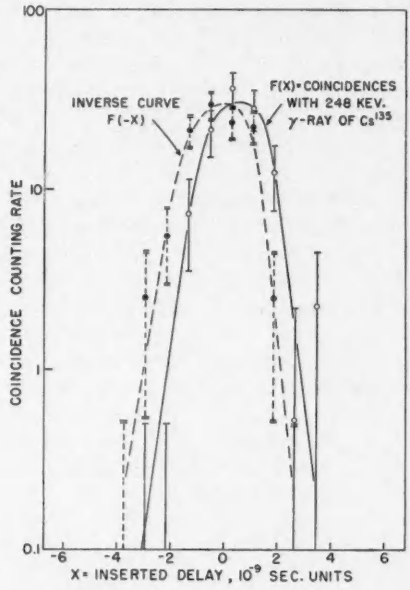

FIG. 4. Self comparison resolution curves for the 248 kev. γ-ray transition of Cs^{135}. The curve $F(-x)$ is the inverse of the delayed resolution curve $F(x)$ and its centroid should lie to the left of the centroid of $F(-x)$ by 2.89 $T_{1/2}$. The result is $T_{1/2} = (2.8 \pm 0.8) \times 10^{-10}$ sec. The standard deviations of the points are shown by vertical bars.

and $\bar{t}$ in this experiment is at most $\sim 10^{-11}$ sec. so that only the statistical error is important. Hence we conclude that the half life of the 248 kev. γ-ray transition in Cs^{135} is

$$T_{1/2} = (2.8 \pm 0.8) \times 10^{-10} \text{ sec.}$$

(e) Pm^{147}, 91 Kev. γ-Ray Transition

11 day Nd^{147} decays in part ($\sim 60\%$) by β^- emission, 825 kev., to a 91 kev. excited state in Pm^{147} (11). The 91 kev. γ-ray transition to the ground state has been classified as $M1$ or $M1 + E2$ radiation by Kondaiah (21), who found $K/L = 6.5 \pm 1.5$ and $\alpha_K \sim 0.9$, and also by Mihelich and Church (27) who found $K/L = 6.4 \pm 2.0$ and that the L conversion was predominantly L_1. These findings are to be compared with the predicted K/L ratios of 7.7 for $M1$ and 0.5 for $E2$ radiation (16), the theoretical K conversion coefficient of 1.9 for $M1$ radiation (30, 35), and the theoretical L shell conversion coefficients of Gellman *et al.* (15), which show that $M1$ radiation is converted predominantly in the L_I shell while $E2$ radiation is converted mainly in the L_{II} and L_{III} shells. Emmerich and Kurbatov (11) found that the lifetime of this transition is $\leqslant 5 \times 10^{-7}$ sec. and McGowan (23) found no β–γ decays in the region 3×10^{-8} sec. to 3×10^{-3} sec.

The β-ray spectrum was examined in the β-ray spectrometer using a source of Nd^{147} prepared from neutron irradiated neodymium oxide about two weeks

after completion of the irradiation. In this way interference from shorter lived activities was avoided. From the areas of the K, L, and M conversion lines, which were clearly resolved, we obtain $K/L = 7.3$ and $L/M = 4.0$. From the areas of the ~ 40 kev. X-ray peak and the 91 kev. γ-ray peak in the scintillation spectrum we obtain after the usual corrections $\alpha_K = 1.8 \pm 0.15$. These values are in good agreement with the theoretical values for $M1$ radiation mentioned above and verify that this transition is predominantly $M1$.

A preliminary measurement of the half life of the 91 kev. γ-ray transition with a $\sim 10\mu$c. source at the center of the pair of β-ray spectrometers gave from the slope of the tail of the delayed resolution curve (not shown) $T_{1/2} = (2.5 \pm 0.4) \times 10^{-9}$ sec. Having identified this lifetime with the 91 kev. transition the counters and source were removed from the spectrometer and the source was sandwiched between the stilbene crystals of the two counters. A 7 mgm. per cm.^{2} Al absorber was placed over the north counter to prevent conversion electrons of the 91 kev. γ transition from being counted. The delayed resolution curve of coincidences between conversion electrons counted in the south counter and β rays counted in the north counter is shown as $F(x)$ in Fig. 5. The curve

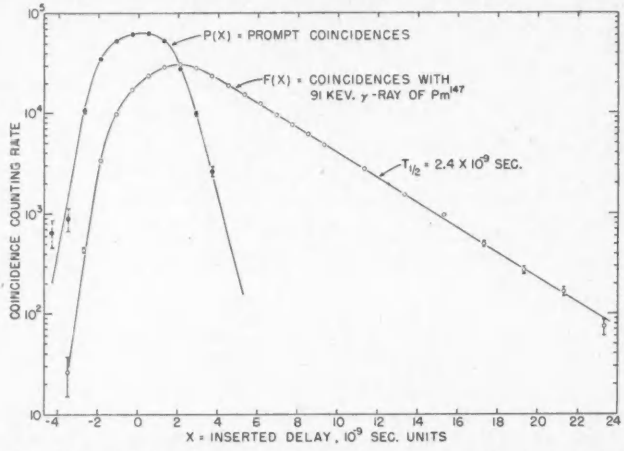
P(X) = PROMPT COINCIDENCES
F(X) = COINCIDENCES WITH 91 KEV. γ-RAY OF Pm147
T1/2 = 2.4 X 10-9 SEC.
COINCIDENCE COUNTING RATE
X = INSERTED DELAY, 10-9 SEC. UNITS

FIG. 5. Delayed resolution curve $F(x)$ for the 91 kev. γ-ray transition of Pm^{147} with a prompt curve $P(x)$ for comparison. From the slope of the tail of $F(x)$ we obtain for the half life of this transition $T_{1/2} = (2.44 \pm 0.08) \times 10^{-9}$ sec. Where the standard deviations are larger than the radii of the circles they are shown by vertical bars.

$P(x)$, obtained when the Nd^{147} source was replaced by one of thorium active deposit, illustrates the performance of the system with prompt radiations. From the slope of the tail of $F(x)$ we obtain for the 91 kev. γ-ray transition in Pm^{147}

$$T_{1/2} = (2.44 \pm 0.08) \times 10^{-9} \text{ sec.}$$

(f) Tl^{208} (ThC'') 40 Kev. γ-Ray Transition

ThC decays in part by α emission, 6.04 Mev., to a 40 kev. excited state in ThC''. The 40 kev. γ-ray transition to the ground state is highly converted in

the L shell. Ellis (32) found that the intensities of the L_I, L_{II}, and L_{III} conversion lines are respectively "very strong", "strong", and "medium" which is the sequence of intensities for $M1$ transitions and unlike that for $E2$ transitions, as shown by the conversion coefficients calculated by Gellman *et al.* (15) and the experiments of Mihelich and Church (26, 27). We therefore tentatively identify this as an $M1$ transition. The A line intensities measured by Flammersfeld (13) and the α-ray intensities of ThC measured by Lewis and Bowden (22) suggest that this transition is almost entirely internally converted. This is consistent with the high L_I conversion coefficients (> 10) calculated by Gellman *et al.* (15) for $M1$ radiation or with those deduced for $L_I + L_{II} + L_{III}$ shells using the known $M1$ conversion coefficients for the K shell (30, 35), the K/L ratio found empirically by Goldhaber and Sunyar (16), and extrapolating down to 40 kev. assuming an E^{-3} dependency.

A source of thorium active deposit of strength $\sim 10\mu$c. was placed over the stilbene crystal of the south counter and the A line conversion electrons were focused on the north counter by a two coil, single spectrometer. Despite the low energy of the A line electrons and poor signal to noise ratio due to the high voltage (2000 v.) applied to the photomultiplier it was possible to observe the line with a counting rate of 1000 to 4000 c.p.m. on a background of noise and continuous β-ray spectrum of 2000 to 4000 c.p.m. The resolution curve $F(x)$ in Fig. 6 shows coincidences between the α particles registered in the south counter

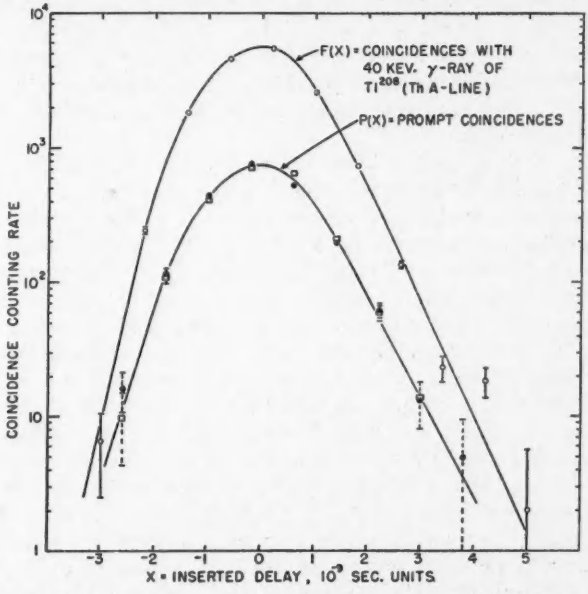

FIG. 6. Delayed resolution curve $F(x)$ for the 40 kev. γ-ray transition (A line) of Tl^{208} (ThC″) with a prompt curve $P(x)$ for comparison. From the shift between the centroids of $F(x)$ and $P(x)$ we obtain for the half life $T_{1/2} < 7 \times 10^{-11}$ sec. Where the standard deviations are larger than the dimensions of the circles or squares they are shown by vertical bars.

and the A line electrons focused in the north counter plotted on a logarithmic scale as a function of inserted delay. The prompt curve $P(x)$ in Fig. 6 is a composite of coincidences observed between F line conversion electrons in the south counter and β rays just below (solid circles) and just above (open squares) the A line after correcting for the change in spectrometer transit time and in $\bar{t}$ in the north counter. The coincidence counting rate off the line, $P(x)$, was about 1/5 that on the line, $F(x)$; the data of $F(x)$ include this prompt coincidence contribution. Analysis of the data according to the method of Bay (1) gives for the mean life of the A line transition $\tau = (-1.8 \pm 1.8) \times 10^{-11}$ sec. which also includes the lifetime of the F line transition (see below). The largest uncertainty ($\sim 5 \times 10^{-11}$ sec.) is in the $\bar{t}$ correction applicable to the south counter because of the slightly different pulse heights in the two cases. We may conclude then that the mean life of the 40 kev. (A line) γ-ray transition in Tl^{208} is less than 10^{-10} sec. and hence

$$T_{1/2} < 7 \times 10^{-11} \text{ sec.}$$

(g) Bi^{212} (ThC) 238 Kev. γ-Ray Transition

ThB decays mainly by β^- emission, 0.33 Mev., followed by a 238 kev. γ-ray transition, whose K conversion line is the well known F line, to the ground state of ThC (Bi^{212}) (36). Martin and Richardson (25) have measured the internal conversion coefficient of this transition and find that it agrees reasonably well with the theoretical coefficient for $M1$ radiation calculated by Rose (30). Moreover estimates of the K/L ratio of this transition compiled by Way (36) cluster near the value of about 7.5 found by Goldhaber and Sunyar (16) for other $M1$ transitions. However the possibility of some admixture of $E2$ radiation remains until better agreement is obtained between measured and theoretical conversion coefficients.

The upper limit in the half life of this transition was previously reported as $T_{1/2} < 10^{-10}$ sec. (3, 17). Four subsequent measurements have been made using the self comparison method and stronger sources ($\sim 200\mu$c.) of thorium active deposit in order to improve the statistical accuracy. The two spectrometer coils were connected in series in all cases. The momentum of the F line electrons in one spectrometer was degraded by about one line width (5%) by an Al absorber of 3–5 mgm. per cm.^{2} placed over the source. In one case the source position was also slightly asymmetrical. The data for each run were accumulated over a period of about 24 hr., and the shift between centroids of the two resolution curves was analyzed by the method of Bay (1) carrying the standard deviations of the points through the numerical computations. After making corrections for the small difference in $\bar{t}$ in the two counters and for the difference in spectrometer transit time in one case, we obtain a weighted average for the mean life of this transition of $\tau = (-1.3 \pm 0.4) \times 10^{-11}$ sec. or $T_{1/2} = (-0.9 \pm 0.3) \times 10^{-11}$ sec. This result indicates the presence of systematic errors of $\sim 1.3 \times 10^{-11}$ sec. which are of the order suggested in the discussion of errors given in Section IV. We may conclude, therefore, that the mean life of the 238 kev. γ-ray transition in ThC is less than 3×10^{-11} sec. and hence

$$T_{1/2} < 2 \times 10^{-11} \text{ sec.}$$

TABLE I

Nucleus	E (kev.)	$T_{1/2}$ (sec.)	K/L ratio			αK		Total α	Type	Log τ_γ	Spins		References
			Exp.	$M1$*	$E2$*	Exp.	$M1$				I_i	I_f	
Li^{7}	478	$(5.2 \pm 1.7) \times 10^{-14}$	-	-	-	-	~ 0	~ 0	$M1$	$\overline{14}.87$	$p_{3/2}$	$p_{1/2}$	12
Fe^{57}	14	1.1×10^{-7}	-	7.6	0.3	-	8.5	10	$M1$	$\overline{6}.24$	$p_{1/2}$	$p_{3/2}$	9
Te^{123}	159	$(1.9 \pm 0.3) \times 10^{-10}$	8.9	7.9	2.4	0.18	0.17	0.21	$M1$	$\overline{10}.52$	$d_{3/2}$	$s_{1/2}$	19, 20, (c)
Te^{125}	35.4	$(1.58 \pm 0.15) \times 10^{-9}$	7.3	7.3	0.1	11.4	14.8	18	$M1$	$\overline{8}.64$	$d_{3/2}$	$s_{1/2}$	7, 14, (c)
Xe^{131}	80	$(4.8 \pm 2.0) \times 10^{-10}$	7.0	7.8	0.7	1.73	~ 1.6	2.0	$M1$	$\overline{9}.32$	$s_{1/2}$	$d_{3/2}$	2, 17
Cs^{135}	81	$(6.0 \pm 0.4) \times 10^{-9}$	7.5	7.6	0.6	1.77	1.75	2.1	$M1$	$\overline{8}.43$	$d_{5/2}$	$g_{7/2}$	6, (c)
Cs^{135}	248	$(2.8 \pm 0.8) \times 10^{-10}$	7.0	7.8	4.0	-	0.07	0.1	$M1 + E2$	$\overline{10}.64$	$d_{5/2}$	$g_{7/2}$	5, (c)
Pm^{147}	91.5	$(2.44 \pm 0.08) \times 10^{-9}$	7.3	7.7	0.5	1.8	1.9	2.2	$M1$	$\overline{8}.05$	-	$d_{5/2}$	21, 27, (c)
Hg^{199}	50	$< 2 \times 10^{-10}$	-	-	-	$\sim 6(a)$	$\sim 10(a)$	8	$M1$	$< \overline{8}.20(b)$	$p_{3/2}$	$f_{5/2}$	3, 17, 34
Hg^{199}	209	$< 2 \times 10^{-10}$	5.4	7.8	0.9	0.54	1.14	0.64	$M1 + E2$	$< \overline{10}.76(b)$	$p_{3/2}$	$p_{1/2}$	3, 17, 34
Tl^{203}	40	$< 7 \times 10^{-11}$	-	-	-	High	$\sim 18(a)$	~ 22	$M1$	$< \overline{9}.40$	-	-	(c)
Bi^{212}	238	$< 2 \times 10^{-11}$	6.7–8.3	7.8	1.0	0.38–0.45	0.44	0.5	$M1$	$< \overline{11}.66$	-	-	23, 36, (c)

* *From empirical curves of Goldhaber and Sunyar* (16).

(a) *L conversion coefficients.*

(b) *Deduced using relative γ-ray intensities by Sherk and Hill* (34).

(c) *Present work.*

VI. DISCUSSION

The information obtained above together with other available information about $M1$ γ-ray transitions is compiled in Table I. Since the measure of the K/L ratio seems to be a sensitive test for the presence of an admixture of $E2$ radiation, the experimental values were compared with Goldhaber and Sunyar's empirical curves for $M1$ and $E2$ transitions (16). τ_γ is here defined as the mean life in seconds for photon emission and is deduced from the experimental half life after correcting for internal conversion using the adopted total conversion coefficient listed in the table. Where possible shell model orbital assignments for the initial and final states are given.

Some additional information on $M1$ transitions has been included from the case of Hg^{199} based on the upper limit for the half life of the 209 kev. excited state previously reported (3) and the disintegration scheme for the decay of Au^{199} proposed by Sherk and Hill (34) which has been borne out by coincidence spectrometer studies in this laboratory (3). A 50 kev. and a 209 kev. γ-ray transition both proceed from the same excited state; the upper limit in the mean life for each transition is deduced using the ratio of γ-ray intensities found by Sherk and Hill.

The estimate of the K conversion coefficient (~ 14) used by Goldhaber and Sunyar (16) for the 14 kev. γ-ray transition in Fe^{57} is probably high. The value, $\alpha_K = 8.5$, used here was deduced from the threshold value for $Z = 26$ (35) assuming an E^{-3} dependency.

In Fig. 7 log τ_γ is plotted as a function of γ-ray energy on a logarithmic scale. For comparison, Weisskopf's relation (37) for magnetic multipole transitions,

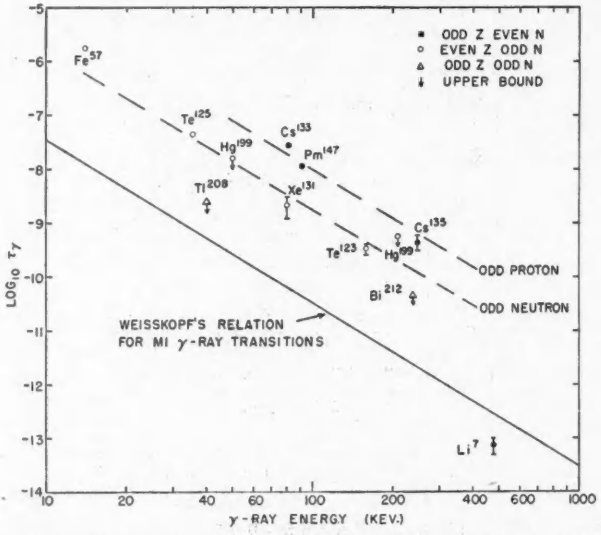

FIG. 7. Lifetime vs. energy for $M1$ γ-ray transitions. Where the standard deviations are larger than the dimensions of the points they are shown by vertical bars.

which for $M1$ transitions becomes $\log_{10} \tau_\gamma = -13.48 - 3 \log_{10} E$ (in Mev.), is shown as a solid straight line. Sachs and Ross (33) give a relation for $M1$ transition probability $(1/\tau_\gamma)$ which is proportional to a matrix element $|\mu|^2$ where μ has the dimensions of a magnetic moment. For ordinary "allowed" $M1$ transitions (shell model orbital $\Delta l = 0$) μ will be the magnetic moment of the odd neutron or proton and this relation becomes for the neutron case $\log \tau_\gamma = -13.39 - 3 \log E$ and for the proton case $\log \tau_\gamma = -13.72 - 3 \log E$, which are in reasonable agreement with Weisskopf's relation.

Most of the experimental lifetimes are ~ 100 times longer than any of the theoretical estimates and may be called empirically forbidden. The transitions in odd neutron nuclei appear to obey an empirical relation $\log \tau_\gamma \cong -11.7 - 3 \log E$ while the three odd proton transitions indicate an empirical relation $\log \tau_\gamma \cong -11.0 - 3 \log E$, i.e. lifetimes about five times longer than in the odd neutron nuclei. These empirical relations are indicated as dashed lines in Fig. 7 and must, of course, be used with caution in predicting $M1$ lifetimes in other nuclei. A similar plot of $\log [\tau_\gamma/(2 I_i + 1)]$ against γ-ray energy (not shown) did not improve the scatter of the experimental points from similarly drawn, E^{-3} slope empirical lines.

According to the shell model orbital assignments most of the empirically forbidden transitions are also theoretically forbidden, i.e. they involve a change of 2 in the orbital angular momentum l of the odd nucleon ($\Delta l = 2$). The transition in Li^7 (proton orbital $p_{1/2} \rightarrow p_{3/2}$) is both empirically and theoretically ($\Delta l = 0$) allowed. Of interest are the two competing transitions in Hg^{199}. According to the shell model assignments (34) the 209 kev. transition is theoretically allowed (neutron orbital $p_{3/2} \rightarrow p_{1/2}$) while the 50 kev. transition is theoretically forbidden (neutron orbital $p_{3/2} \rightarrow d_{5/2}$). The relative transition probabilities are, however, very nearly the same after correcting for energy, and the two transitions are probably both empirically forbidden (see Fig. 7). The orbital assignments for the two (odd neutron) states in Fe^{57} ($p_{1/2} \rightarrow p_{3/2}$) are the only ones which are consistent with the known decay scheme (36) and the shell model. This transition is thus another example of a theoretically allowed odd neutron transition which is empirically forbidden. It is interesting to note that the lifetimes of the two transitions in odd–odd nuclei are both distinctly shorter than any of the forbidden transitions.

ACKNOWLEDGMENTS

The authors are indebted to Dr. L. Yaffe and Dr. F. Brown for preparation of sources, and to Dr. L. G. Elliott for valuable discussions.

REFERENCES

1. BAY, Z. Phys. Rev. 77: 419. 1950.
2. BELL, R. E. and GRAHAM, R. L. Phys. Rev. 86: 212. 1952.
3. BELL, R. E., GRAHAM, R. L. and PETCH, H. E. Can. J. Phys. 30: 35. 1952.
4. BELL, R. E. and PETCH, H. E. Phys. Rev. 76: 1409. 1949.
5. BERGSTRÖM, I. Phys. Rev. 82: 111. 1951.
6. BERGSTRÖM, I. and THULIN, S. Phys. Rev. 79: 538. 1950.
7. BOWE, J. C. and AXEL, P. Phys. Rev. 85: 858. 1952.
8. BOWE, J. C. and SCHARFF-GOLDHABER, G. Phys. Rev. 76: 437. 1949.
9. DEUTSCH, M. Private communication to K. Way. Nuclear data. Natl. Bur. Standards (U.S.), Circ. 499. 1950.

10. DEUTSCH, M. and WRIGHT, W. E. Phys. Rev. 77: 139. 1950.
11. EMMERICH, W. S. and KURBATOV, J. D. Phys. Rev. 83: 40. 1951.
12. ELLIOTT, L. G. and BELL, R. E. Phys. Rev. 76: 168. 1949.
13. FLAMMERSFELD, A. Z. Physik, 114: 227. 1939.
14. FRIEDLANDER, G., PERLMAN, M. L., and SCHARFF-GOLDHABER, G. Phys. Rev. 80: 1103. 1950.
15. GELLMAN, H., GRIFFITHS, B. A., and STANLEY, J. P. Phys. Rev. 85: 944. 1952.
16. GOLDHABER, M. and SUNYAR, A. W. Phys. Rev. 83: 906. 1951.
17. GRAHAM, R. L. and BELL, R. E. Phys. Rev. 84: 380. 1951.
18. GRAHAM, R. L., WOLFSON, J. L., and BELL, R. E. Can. J. Phys. 30: 459. 1952.
19. HILL, R. D. Phys. Rev. 76: 333. 1949.
20. KATZ, R., HILL, R. D., and GOLDHABER, M. Phys. Rev. 78: 9. 1950.
21. KONDAIAH, E. Phys. Rev. 81: 1056. 1951.
22. LEWIS, W. B. and BOWDEN, B. V. Proc. Roy. Soc. (London), A, 145: 235. 1934.
23. MCGOWAN, F. K. Oak Ridge Rept. ORNL-481, 30. 1949.
24. MCGOWAN, F. K. Phys. Rev. 85: 142. 1952.
25. MARTIN, D. G. E. and RICHARDSON, H. O. W. Proc. Phys. Soc. (London), A, 63: 223. 1950.
26. MIHELICH, J. W. Phys. Rev. 87: 646. 1952.
27. MIHELICH, J. W. and CHURCH, E. L. Phys. Rev. 85: 690. 1952.
28. NEWTON, T. D. Phys. Rev. 78: 490. 1950.
29. POST, R. F. and SCHIFF, L. Phys. Rev. 80: 1113. 1950.
30. ROSE, M. E., GOERTZEL, G. N., SPINRAD, B. I., HARR, J., and STRONG, P. Phys. Rev. 83: 79. 1951.
31. ROSS, M. Phys. Rev. 88: 935. 1952.
32. RUTHERFORD, E., CHADWICK, J., and ELLIS, C. D. Radiations from radioactive substances. Cambridge University Press, London. 1930.
33. SACHS, R. G. and ROSS, M. Phys. Rev. 84: 379. 1951.
34. SHERK, P. M. and HILL, R. D. Phys. Rev. 83: 1097. 1951.
35. SPINRAD, B. I. and KELLER, L. B. Phys. Rev. 84: 1056. 1951.
36. WAY, K. Nuclear data. Natl. Bur. Standards (U.S.), Circ. 499. 1950.
37. WEISSKOPF, V. F. Phys. Rev. 83: 1073. 1951.

THE SOUND FIELD OF A PISTON SOURCE[1]

By Ernest W. Guptill

ABSTRACT

An exact solution is presented for the sound field between two infinite walls when the source is a piston in one of the walls. A method is also outlined for the case of a source having any amplitude distribution which is a function only of radial distance from the center of the source. Several graphs are shown and they are intended to illustrate how the pressure on a receiving crystal would vary when the wall separation is changed.

The sound field from an acoustical source set in a rigid and infinite wall has been investigated theoretically by King (3), Rayleigh (4), Stenzel (5), Williams (7, 8), and others. It seems quite improbable that an exact solution to this problem in terms of presently known functions is possible. Approximate solutions have been obtained (5, 7, 8) and the velocity potential plotted for special cases. Not a great deal of emphasis, however, has been placed upon the difficulties facing the experimenter who attempts to measure the velocity of propagation with some precision. Williams and others (7) have given the deviation from the plane wave front by averaging the velocity potential over a circular area which would coincide with the receiving crystal. There is some question as to the usefulness of this procedure since it assumes that all the incident energy is absorbed by the receiver.

The theory set forth here attempts to simulate more nearly experimental conditions by adding a second infinite and rigid wall (parallel to the first) in lieu of the receiver. The theoretical advantage of doing this is considerable since it makes possible an exact solution of the field between the two walls. In actual experiment the size of the "infinite" walls may be quite finite, depending on the directivity

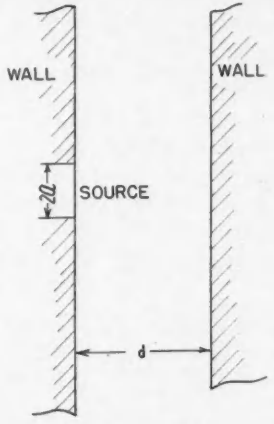

Fig. 1. A schematic diagram of the circular source set in one of two parallel and rigid walls.

[1] *Manuscript received October 6, 1952.*
Contribution from the Department of Physics, Dalhousie University, Halifax, N.S.

of the transmitter and the separation of the walls. Receiving may be effected by drilling a small hole in the second wall and placing a crystal one half wave length behind the first face of this wall. Preliminary tests indicate that this technique is very successful.

Consider first the so-called piston source of radius a set in a rigid flange with a second flange a distance d in front of the source (Fig. 1). The velocity potential which is a solution of the wave equation is then subject to the following boundary conditions

$$[1] \qquad \begin{aligned} \left(\frac{\partial \phi}{\partial z}\right)_{z=0} &= 0 && \rho > a, \\ &= e^{-i\omega t} && \rho < a, \\ \left(\frac{\partial \phi}{\partial z}\right)_{z=d} &= 0 && 0 < \rho < \infty \end{aligned}$$

where ρ and z are the parameters of the cylindrical coordinate system.

It is obvious that there will be waves travelling in the negative as well as the positive z-direction, and the integral solution of the wave equation given by King (3) must be altered to include both these waves, thus:

$$[2] \qquad \phi = e^{-i\omega t} \int_0^\infty \left[A(\lambda) e^{i\mu(z-d)} + B(\lambda) e^{-i\mu(z-d)} \right] \frac{J_0(\lambda\rho)\ \lambda\ d\lambda}{i\mu}$$

where $\mu = \sqrt{k^2 - \lambda^2}$, $z < d$, and k is a propagation constant with a positive imaginary part. The integration is conducted along the positive real axis but may be deformed into the complex plane of λ, provided the contour remains on that branch of the function μ which maintains the imaginary part of μ positive. $A(\lambda)$ and $B(\lambda)$ are functions of the integration variable λ and must be adjusted so that the derivatives of ϕ satisfy the boundary conditions. If $A(\lambda)$ and $B(\lambda)$ are evaluated using the Fourier–Bessel transform (6) and Equation [1], one obtains for ϕ (the harmonic time variation will be omitted henceforth)

$$[3] \qquad \phi = a \int_0^\infty \frac{\cos \mu(z-d)}{\mu \sin \mu d} J_1(\lambda a)\ J_0(\lambda\rho)\ d\lambda$$

which is a solution of the wave equation satisfying the given boundary conditions. The integrand in [3] is a single-valued function of λ, and it will be shown that the integral may be evaluated by integrating along a properly chosen contour in the complex plane if the Bessel functions are expressed as a sum of Hankel functions.

Two solutions of the integral are possible, one for each of the two substitutions:

$$2J_0(\lambda\rho) = H_0^1(\lambda\rho) + H_0^2(\lambda\rho)$$

and

$$2J_1(\lambda a) = H_1^1(\lambda a) + H_1^2(\lambda a).$$

The former will yield ϕ for $\rho > a$ and the latter ϕ for $\rho < a$. In the first instance we have

$$[4] \qquad \phi_1 = \frac{a}{2} \int_0^\infty f(\mu)\ J_1(\lambda a)\ H_0^1(\lambda\rho)\ d\lambda + \frac{a}{2} \int_0^\infty f(\mu)\ J_1(\lambda a)\ H_0^2(\lambda\rho)\ d\lambda$$

where $f(\mu)$ has been written for $\cos \mu(z-d)/\mu \sin \mu d$.

The second integral of Equation [4] may be written in terms of a Hankel function of the first kind for

$$\frac{a}{2}\int_0^\infty f(\mu)\ J_1(\lambda a)\ H_0^2(\lambda\rho)\ d\lambda = -\frac{a}{2}\int_0^\infty f(\mu)\ J_1(\lambda a)\ H_0^1(\lambda\rho e^{i\pi})\ d\lambda$$

$$= -\frac{a}{2}\int_0^\infty f(\mu)\ J_1(\lambda a e^{i\pi})\ H_0^1(\lambda\rho e^{i\pi})\ d(\lambda e^{i\pi})$$

$$= \frac{a}{2}\int_{-\infty}^0 f(\mu)\ J_1(\lambda a)\ H_0^1(\lambda\rho)\ d\lambda$$

and Equation [4] becomes

$$[5] \qquad \phi_1 = \frac{a}{2}\int_0^\infty f(\mu)\ J_1(\lambda a)\ H_0^1(\lambda\rho)\ d\lambda + \frac{a}{2}\int_{-\infty}^0 f(\mu)\ J_1(\lambda a)\ H_0^1(\lambda\rho)\ d\lambda.$$

The path of integration for the second integral of Equation [5] must be obtained from the path of the first integral by its reflection on the origin. The contour must then extend the entire length of the real axis. Since there is no contribution from the half circuit about the origin, the contour may be deformed into any path in the top half of the λ-plane which does not cut the line of singularities occurring at $\mu d = n\pi$. Along this line μ is wholly real and on crossing, the imaginary part changes sign. If the path is folded to the dotted path in Fig. 2, $\phi_1/2\pi i$ is the sum of the enclosed residues which are all at simple poles:

$$[6] \qquad \phi_1 = -i\pi \sum_{n=0}^{\infty}{}' \cos n\pi z/d \frac{J_1(\lambda_n a)\ H_0^1(\lambda_n\rho)}{d\lambda_n}$$

where $\lambda_n = k\sqrt{1 - (n\pi/kd)^2}$.

(The dash above the summation sign indicates henceforth that the $n = 0$ term is to be multiplied by 1/2.)

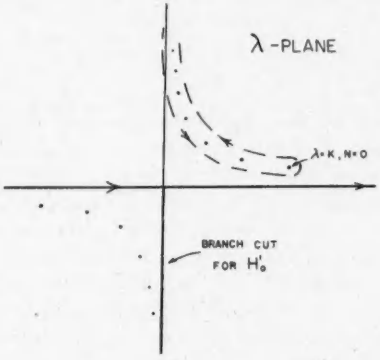

FIG. 2.

The series converges rapidly for small values of kd but the convergence deteriorates as kd becomes larger. For purposes of computation the series may be closed at that value of n which makes the argument of the Hankel function

imaginary, that is, when $n\pi$ exceeds kd. Interpreted physically, this means that when the separation is less than one half wave length, only one of the family of cylindrical waves is propagated radially outwards. The others ($n = 1, 2$, etc.) are evanescent waves which attenuate rapidly with increasing ρ. When the wall separation increases to two half wave lengths, the cylindrical waves effectively propagated increase by one.

If for $2J_1(\lambda a)$ we now put $H_1^1(\lambda a) + H_1^2(\lambda a)$, a second integral for ϕ is obtained, namely,

$$[7] \qquad \phi_2 = \frac{a}{2}\int_{-\infty}^{\leftarrow 0} f(\mu)\ J_0(\lambda\rho)\ H_1^1(\lambda a)\ d\lambda + \frac{a}{2}\int_{\epsilon\rightarrow 0}^{\infty} f(\mu)\ J_0(\lambda\rho)\ H_1^1(\lambda a)\ d\lambda.$$

The Hankel function of order one has a singularity of the same order at the origin as well as a branch point. From this it follows that the contour must be indented upwards if it is to be closed in the top half of the λ-plane (Fig. 3). Otherwise the contour is the same as for ϕ_1. On evaluation of the residues ϕ_2 becomes

$$[8] \qquad \phi_2 = a\left[\frac{\cos k(z-d)}{ka \sin kd} - i\pi \sum_{n=0}^{\infty}{}' \cos n\pi z/d\ \frac{J_0(\lambda_n\rho)\ H_1^1(\lambda_n a)}{\lambda_n d}\right].$$

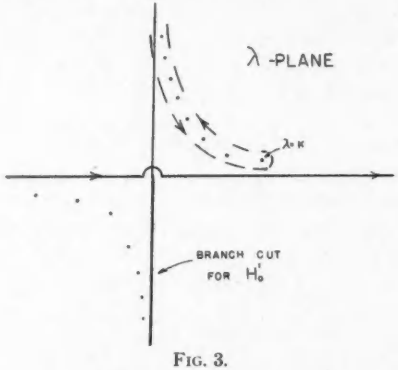

FIG. 3.

The first term of Equation [8] is the velocity potential of a plane wave normally incident on a rigid wall. The series again represents a family of outward bound cylindrical waves with the attenuation of the evanescent ones increasing as ka increases. It is interesting to note the form of the ϕ_2 (which is proportional to the pressure) in the plane of the source, that is, at $z = 0$. If the wall separation is one quarter wave length, the plane wave component contributes nothing to this pressure, and the principal contribution from the series is the first term which gives a variation in the radial direction of $J_0(k\rho)$.

It is apparent from the form of Equations [6] and [8] that the former must be used for $\rho > a$ and the latter for $\rho < a$, and it will now be shown that the two values of ϕ are identical when $\rho = a$.

The Wronskian determinant of the two solutions $J_0(z)$ and $H_0^1(z)$ of Bessel's equation has the value $i2/\pi z$, that is,

$$J_1(\lambda_n a)\ H_0^1(\lambda_n a) = J_0(\lambda_n a)\ H_1^1(\lambda_n a) + \frac{i2}{\pi\lambda_n a}$$

which relation gives for ϕ_1 at $\rho = a$,

$$\phi_1 = -i\pi a \sum_{n=0}^{\infty}{}' \cos n\pi z/d \left[\frac{J_0(\lambda_n a)\, H_1^1(\lambda_n a)}{\lambda_n d} + \frac{i2}{\pi \lambda_n a \lambda_n d} \right]$$

$$[9] \qquad = a\left[\frac{2kd}{ka} \sum_{n=0}^{\infty}{}' \frac{\cos n\pi z/d}{(kd)^2 - (n\pi)^2} - i\pi \sum_{n=0}^{\infty}{}' \cos n\pi z/d \, \frac{J_0(\lambda_n a) H_1^1(\lambda_n a)}{\lambda_n d} \right].$$

The first sum of [9] is the series expansion of $[\cos k(z - d)]/ka \sin kd$ about the points $kd = n\pi$, and therefore the identity of ϕ_1 and ϕ_2 at $\rho = a$ is established.

Equation [8] has been plotted for a few special cases. In Fig. 4, z has been put equal to d, $ka = 10$, $\rho = 0$, and $|\phi/a|$ plotted for wall separations up to one wave length. It will be noticed that the velocity potential becomes large as kd approaches $n\pi$. At this separation the height of the curve depends upon the imaginary part of k, that is α, and in these curves it has been assumed that α is much less than the real part of k.

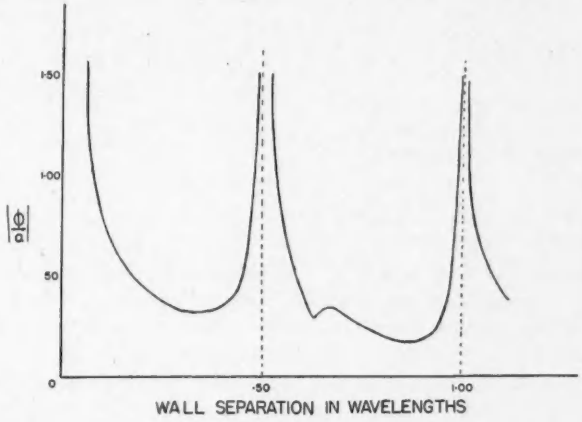

FIG. 4. The piston source. A graph showing the modulus of velocity potential vs. wall separation for $ka = 10$, $z = d$, and $\rho = 0$ (Equation [8]).

The amplitude and frequency of the undulations occurring just beyond the half wave length separations are very sensitive functions of ka. As the value of ka increases, their amplitude and frequency increase, as may be seen in Fig. 5 where the value of ka has been increased to 25 while the other parameters are the same as in Fig. 4. Apparently these undulations merge into a single smooth curve in the limiting case of $ka \to \infty$.

In the case of a cylindrical boundary a solution with inward bound cylindrical waves is necessary and may be obtained by writing Equation [3] in terms of $H_0^2(\lambda\rho)$ and $H_1^2(\lambda a)$ instead of $H_0^1(\lambda\rho)$ and $H_1^1(\lambda a)$. The contours of Figs. 2 and 3 must then be closed in the bottom half of the λ-plane since the branch cut of the Hankel function of the second kind lies along the positive imaginary axis.

The value of ϕ_2 averaged over a receiving surface of radius b at $z = d$ is easily calculated:

$$\langle \phi_2 \rangle = \frac{1}{\pi b^2} \int_0^b \phi_2 \, 2\pi\rho \, d\rho$$

$$= a\left[\frac{1}{ka \sin kd} - 2\pi i \frac{kd}{kb} \sum_{n=0}^{\infty}{}' \frac{(-1)^n J_1(\lambda_n b) H_1^1(\lambda_n a)}{(kd)^2 - (n\pi)^2}\right]. \quad [10]$$

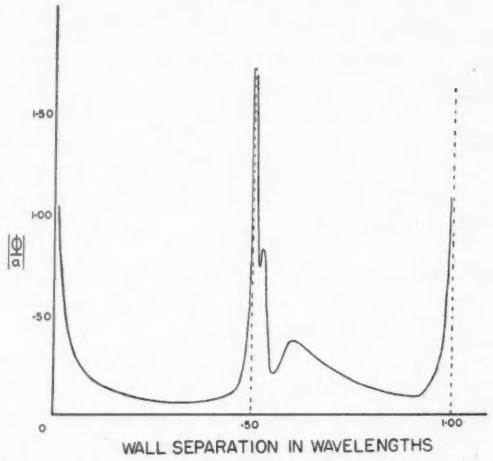

FIG. 5. The piston source. A graph showing the modulus of velocity potential vs. wall separation for $ka = 25$, $z = d$, and $\rho = 0$ (Equation [8]).

Fig. 6 shows a plot of $|\langle \phi_2 \rangle / a|$ for $ka = 25$ and $kb = 5$. The points for this graph were easily computed. In fact, when $ka > 10$ and $kb > ka/5$ only one term in the series is important and even this may be omitted when kd is not near $m\pi$.

The field between the walls may be calculated for a source having any amplitude distribution $g(\rho)$ which is a function of ρ only. $g(\rho)$ may be expanded in the range $0 < \rho < a$ thus:

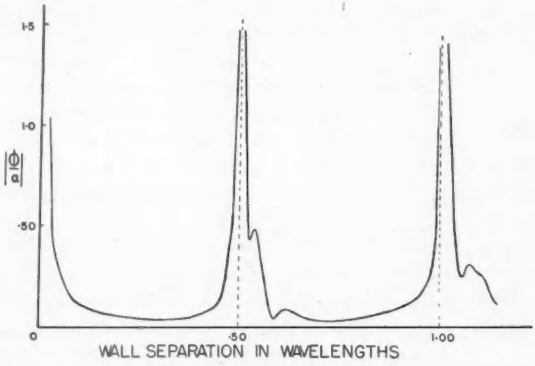

FIG. 6. The piston source. A graph showing the modulus of velocity potential averaged over a surface which is coaxial with the source and which has a radius b; $ka = 25$, $kb = 5$, and $z = d$ (Equation [10]).

[11] $$g(\rho) = A_1 J_0(\gamma_1 \rho) + A_2 J_0(\gamma_2 \rho) + \ldots$$

where $\gamma_l a$ is the l^{th} root of the zero order Bessel function and A_l a coefficient determined by (*vide* (1))

$$A_l = \int_0^a g(\rho)\ J_0(\gamma_l \rho)\ \rho\ d\rho.$$

What this series yields for $\rho > a$ is not relevant. We may now obtain the velocity potential for any term in the series by using the boundary conditions

$$\left(\frac{\partial \phi_l}{\partial z}\right)_{z=0} = 0 \qquad \rho > a,$$

$$= A_l\ J_0(\gamma_l \rho) \qquad \rho < a,$$

$$\left(\frac{\partial \phi_l}{\partial z}\right)_{z=d} = 0 \qquad 0 < \rho < \infty.$$

For the solution of ϕ_l one may proceed in the same manner as for the piston source. In place of Equation [3] we have (dropping the subscript l on γ, ϕ, and A)

$$\phi = -\ A\ \gamma a\ J_1(\gamma a) \int_0^\infty f(\mu)\ \frac{J_0(\lambda a)\ J_0(\lambda \rho)\ \lambda}{\lambda^2 - \gamma^2}\ d\lambda$$

and in place of [6] and [8]

$$\phi = -\ \frac{2A}{H_0^1(\gamma a)} \sum_{n=0}^{\infty}{}' d \cos n\pi z/d\ \frac{J_0(\lambda_n a)\ H_0^1(\lambda_n \rho)}{(kd)^2 - (n\pi)^2 - (\gamma d)^2}$$

for $\rho > a$ and

[12]

$$\phi = A\left[\frac{J_0(\gamma\rho)\cos\beta(z-d)}{\beta \sin \beta d} - \frac{2}{H_0^1(\gamma a)} \sum_{n=0}^{\infty}{}' d \cos n\pi z/d\ \frac{J_0(\lambda_n \rho)\ H_0^1(\lambda_n a)}{(kd)^2 - (n\pi)^2 - (\gamma d)^2}\right]$$

for $\rho < a$ ($\beta = \sqrt{k^2 - \gamma^2}$).

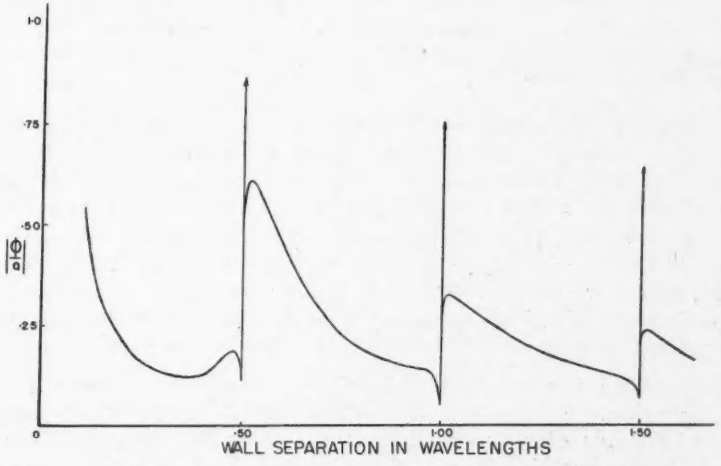

FIG. 7. A graph showing the modulus of velocity potential from a source with an amplitude distribution equal to $J_0(\gamma\rho)$. $ka = 10.2$, $\gamma a = 5.52$, $\rho = 0$, and $z = d$ (Equation [12]).

Figs. 7 and 8 show a plot of the modulus and phase of ϕ/a for $ka = 10.2$, $\rho = 0$, $\gamma a = 5.52$, and $z = d$. Once again the height of the curves at the half wave position depends upon the imaginary part of k. One important difference between the graph in Fig. 7 and the corresponding case for the piston source (Fig. 4) is worth noting. In the former the half wave length points are always marked by a sharp rise in the velocity potential, whereas for the piston source the same places are marked by an outstanding maximum.

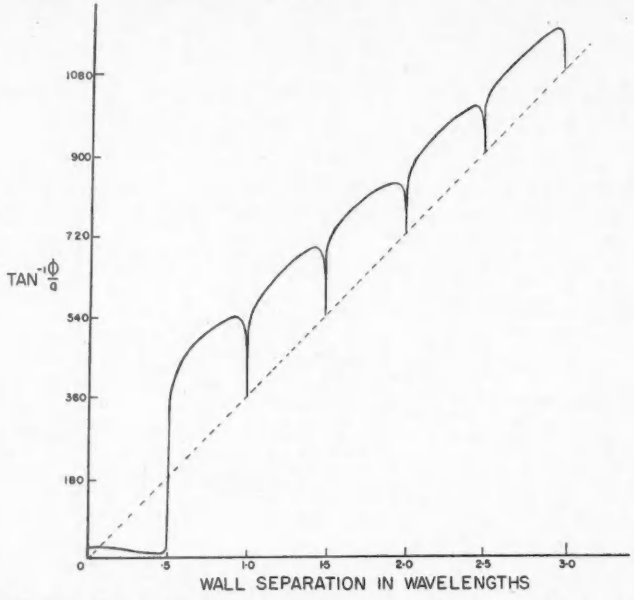

FIG. 8. A graph showing the phase of the velocity potential. The modulus of this velocity potential is shown in Fig. 7.

In Fig. 8 the slope of the curve is surprisingly linear for separations which are not close to an integral number of half wave lengths. The average slope is, however, considerably less than that for a plane wave, the phase of which is represented by the dotted line. This average slope gives a phase velocity very nearly equal to $\omega/\sqrt{k^2-\gamma^2}$, and the distance between two consecutive points of equal phase is then $[1-(\gamma a/ka)^2]^{-\frac{1}{2}}$ times the free space wave length. If $\gamma a = 2.40 \ll ka$, the factor becomes $1 + 2.88/(ka)^2$. This result compares well with the approximate solution in (2), although it is doubtful whether the comparison means much since the boundary conditions in (2) were slightly different.

The author is indebted to the University of Toronto's Computation Centre which provided the computations used in Figs. 7 and 8. He also wishes to express appreciation for the benefit derived from frequent discussions with his colleague, Dr. A. D. MacDonald.

REFERENCES

1. BYERLY, W. E. Fourier's series and spherical harmonics. Ginn and Company, Boston. 1893. p. 228.
2. GUPTILL, E. W. and MACDONALD, A. D. Can. J. Phys. 30: 119. 1952.
3. KING, L. V. Can. J. Research, 11: 135. 1934.
4. RAYLEIGH, J. W. S. (3rd Baron). Theory of sound. Dover Publications, New York. 1945. p. 162.
5. STENZEL, H. Ann. Physik, 41: 245. 1942.
6. STRATTON, J. A. Electromagnetic theory. McGraw-Hill Book Co. Inc., New York and London. 1941. p. 369.
7. WILLIAMS, A. O. J. Acoust. Soc. Am. 23: 1. 1951.
8. WILLIAMS, A. O. and CARTER, A. H. J. Acoust. Soc. Am. 23: 179. 1951.

THE MAXIMUM AGE OF THE ELEMENTS AND THE AGE OF THE EARTH'S CRUST[1]

By C. B. Collins, R. D. Russell, and R. M. Farquhar

ABSTRACT

Estimates are given of a maximum time of formation of the elements of 5.5 billion years and of the time of formation of the earth's crust at 3.5 billion years. These estimates were based on the isotopic constitution of lead ores dated from isotopic analyses of radiogenic leads from uranium minerals. Methods of calculation are described.

Experimental measurements of the isotopic constitution of lead from mass spectrograms of lead tetramethyl are reported with examples.

A number of papers dealing with the age of the earth's crust and setting a limit on the time of formation of the elements have been published in the past ten years. Most of these estimates have been based on variations in the isotopic constitution of leads which have been separated as lead ores from the earth's crust at different times. These variations are believed to result from additions of

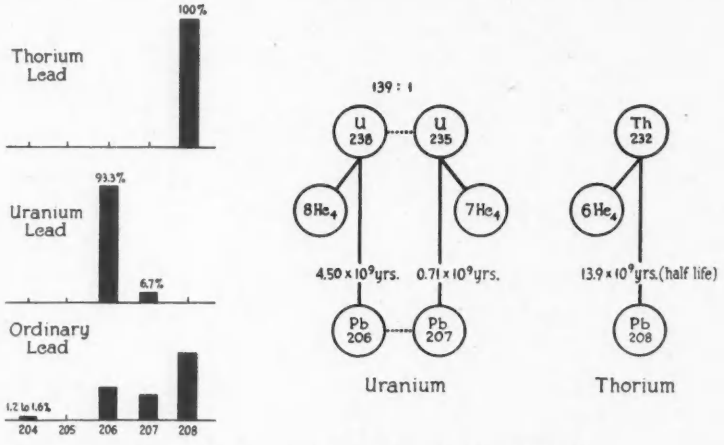

Fig. 1. Common and radiogenic lead. (After Bullard.)

radiogenic lead to ordinary lead. Ordinary lead is assumed to be a mixture of radiogenic lead from uranium and thorium combined with lead formed by other processes at the time of formation of the elements (see Fig. 1).

Estimates of the age of the earth's crust by Holmes (9), 3.35 billion years, and by Bullard and Stanley (4), 3.29 billion years, have been reported. Alpher

[1] *Manuscript received September 11, 1952.*
Contribution from the Department of Physics, Geophysics Laboratory, University of Toronto, Toronto, Ont. This work was supported by the National Research Council and by the Research Council of Ontario.

and Herman (2) assigned a value of 5.3 billion years ago as the earliest time of formation of the elements. These authors based their calculations on a set of isotopic analyses of common leads by Nier (12, 15). Nier also reported the ages of uranium minerals from various localities (13). These ages were used to date the time of mineralization of the common leads.

All the investigators who have used Nier's analyses have pointed out that more data were needed to avoid the possibility of gross errors in their calculations. We have analyzed a number of common leads from lead ores, some of which have been dated from Nier's ages (13), and from isotopic analyses of radiogenic leads in our laboratory. New estimates of the age of the earth's crust and the maximum limit on the time of formation of the elements have been calculated from our data combined with those reported previously by Nier (12, 15).

EXPERIMENTAL

The measurement of the isotopic constitution of lead (which is a solid at room temperature) has always presented a problem in mass spectrometer analysis. Since the usual procedure is to produce ions in a mass spectrometer by electron bombardment of gaseous atoms or molecules, ionization of solids has been carried out by raising the temperature of the solid until a vapor is given off which can be ionized in an electron beam like any other gas. Analysis of solids is generally much more difficult than that of gases. To avoid the problems associated with solid sample analysis recent investigations in the use of gaseous lead tetramethyl for the isotopic analysis of lead have been made by Collins *et al.* (5, 6). Dibeler and Mohler (7) reported similar studies of organometallic compounds including lead tetramethyl. Both groups arrived at the conclusion that the measurement of the isotopic abundances of lead from mass spectrograms of lead tetramethyl is feasible.

Lead tetramethyl dissociates on bombardment by 70 v. electrons to produce Pb^+, $Pb(CH_3)_2^+$, and $Pb(CH_3)_3^+$ ions. A low abundance of molecular $Pb(CH_3)_4^+$ ions was also observed. Dibeler and Mohler (7) reported the abundances of all ions observed from lead tetramethyl from C^+ to $Pb(CH_3)_4^+$. Calculation of the abundances of the lead isotopes is complicated by the presence of hydrides, by the loss of from one to three hydrogen atoms, and by the C^{13} effect. For isotopic abundance measurements, spectrograms of the Pb^+ and $Pb(CH_3)_3^+$ ion groups are the most useful.

The magnitude of the abundances of PbH^+ ions in the Pb^+ spectrogram, and of the C^{13} effect in the $Pb(CH_3)_3^+$ spectrogram given in this report are not the same as those reported by Dibeler and Mohler (7). Presumably the difference arises in the observed abundances of PbH^+ ions because of different ion source conditions; their ion source was maintained at a temperature of 285°C., while ours was operated at room temperature. The validity of the analysis is not believed to be dependent on source conditions, providing that these conditions are maintained constant throughout the analysis.

The interpretation of the Pb^+ spectrogram is best illustrated by the following example.

PbH^+ EFFECT IN THE Pb^+ SPECTROGRAM

Mass number	Ions
204	Pb^{204}
205	$Pb^{204}H$
206	Pb^{206}
207	$Pb^{207} + Pb^{206}H$
208	$Pb^{208} + Pb^{207}H$
209	$Pb^{208}H$

RELATIVE ISOTOPIC ABUNDANCES OF LEAD FROM THE Pb^+ SPECTROGRAM

Mass number	Relative ion intensity	Lead isotope	Relative abundance, %
204	1.448 ± 0.003	204	1.574 ± 0.005
205	0.135 ± 0.003		
206	20.31 ± 0.02	206	22.07 ± 0.03
207	23.23 ± 0.02	207	23.33 ± 0.03
208	50.65 ± 0.03	208	53.02 ± 0.05
209	4.23 ± 0.01		

It will be noted that the PbH^+ ions present accounted for 8.3% of the total signal from the Pb^+ ion group. Furthermore, the fraction of PbH^+ ions present could be expected to vary depending on the temperature of the mass spectrometer ion source (16) and the energy of the bombarding electrons, although under constant ionization conditions no change in this fraction was observed. No problem exists in the measurement of the isotopic abundances of ordinary lead where Pb^{208} is the most abundant isotope, and a good measure of $Pb^{208}H^+$ ions at mass number 209 is possible. But uranium lead has an abundant 206 isotope, a low 207, and little or no lead 208. Here a satisfactory measure of the PbH^+ fraction is not possible and therefore radiogenic lead abundances calculated from this spectrogram could be in error. These difficulties are largely avoided in the $Pb(CH_3)_3^+$ spectrogram.

In the interpretation of the $Pb(CH_3)_3^+$ spectrogram, corrections have been made for the loss of one hydrogen atom, and for the C^{13} effect. Dibeler and Mohler (7) reported signals due to $Pb(C_3H_{10})^+$ ions amounting to 0.33% of the total signal from the $Pb(CH_3)_3^+$ ions. This figure was obtained (by Dibeler and Mohler) by subtracting the contributions of ions containing C^{13} atoms and assigning the residue to $Pb(C_3H_{10})^+$ ions. The relative abundances of the carbon isotopes vary according to the source of the carbon (11), so any correction based on the abundance of C^{13} is uncertain. To account for our observed signal at mass 254 in the $Pb(CH_3)_3^+$ spectrogram on the basis of C^{13} effect, an abundance of 1.125% for this isotope would be required. If the abundance of C^{13} for carbon from limestone of 1.11% (14) is used, then the $Pb(C_3H_{10})^+$ ions would amount to about 0.08% of the $Pb(C_3H_9)^+$ ions. This figure applies to analysis when the mass spectrometer ion source is operated at room temperature. However, the calculation of the relative abundances of the lead isotopes is not

C^{13} AND $Pb(C_3H_8)^+$ EFFECTS IN THE $Pb(CH_3)_3^+$ SPECTROGRAM

Mass number	Ions
248	$Pb^{204}(C^{12}H_3)_2(C^{12}H_2)$
249	$Pb^{204}(C^{12}H_3)_3$
250	$Pb^{204}(C^{12}H_3)_2(C^{13}H_3) + Pb^{206}(C^{12}H_3)_2(C^{12}H_2)$
251	$Pb^{206}(C^{12}H_3)_3 + Pb^{207}(C^{12}H_3)_2(C^{12}H_2)$
252	$Pb^{207}(C^{12}H_3)_3 + Pb^{206}(C^{12}H_3)_2(C^{13}H_3) + Pb^{208}(C^{12}H_3)_2(C^{12}H_2)$
253	$Pb^{208}(C^{12}H_3)_3 + Pb^{207}(C^{12}H_3)_2(C^{13}H_3)$
254	$Pb^{208}(C^{12}H_3)_2(C^{13}H_3)$

RELATIVE ISOTOPIC ABUNDANCES OF LEAD FROM THE $Pb(CH_3)_3^+$ SPECTROGRAM

Mass number	Relative intensity	Lead isotope	Relative abundance, %
248	0.01 ± 0.005		
249	1.505 ± 0.005	204	1.569 ± 0.005
250	0.23 ± 0.01		
251	21.26 ± 0.02	206	21.97 ± 0.03
252	23.56 ± 0.02	207	23.41 ± 0.03
253	51.67 ± 0.03	208	53.04 ± 0.05
254	1.77 ± 0.005		

The errors listed for Pb^+ *and* $Pb(CH_3)_3^+$ *spectrograms described above apply to reproducibility of the measurements; the absolute error is believed to be less than 1%.*

changed by the presence of a small fraction of $Pb(C_3H_{10})^+$ ions whose contribution may be combined with that of C^{13} and measured from the ion current at mass number 254.

Either the Pb^+ or $Pb(CH_3)_3^+$ spectrogram is suitable for measuring the abundances of the isotopes of common lead. The Pb^+ spectrogram is probably the less reliable because of Hg^{204} which adds to the Pb^{204} peak, and because the PbH^+/Pb^+ fraction is dependent on the energy of the ionizing electron beam and the temperature of the ion source. In the analysis of radiogenic lead made up chiefly of Pb^{206} with a low Pb^{207} and little or no Pb^{208} or Pb^{204}, no direct measure of the PbH^+ contribution is possible. In the $Pb(CH_3)_3^+$ spectrogram the largest correction is for the contribution of ions containing a C^{13} atom, whose magnitude is not critically dependent on the energy of the ionizing electrons or the temperature of the mass spectrometer ion source. The contribution from ions which have lost one atom of hydrogen is of the order of 1%, and any small variation in this quantity would not change the calculated abundances of the lead isotopes by an appreciable amount. For these reasons the isotopic constitution of uranium lead determined from the $Pb(CH_3)_3^+$ spectrogram of lead tetramethyl is believed to be reliable. Spectrograms of lead tetramethyl are shown in Figs. 2 and 3. By analyzing both ordinary and radiogenic lead it was possible to check the various isotopic contributions which gave rise to the ion currents at the different mass numbers.

Lead was extracted from uranium samples by standard chemical methods, and the preparation of lead tetramethyl was carried out with the assistance of

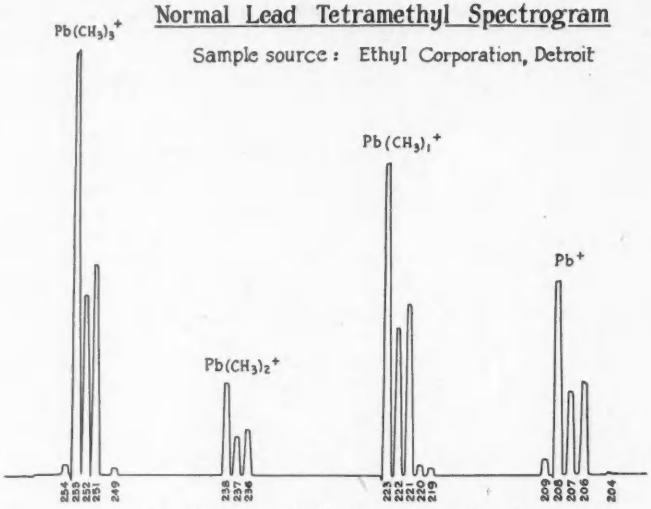

FIG. 2. Normal lead tetramethyl spectrogram.

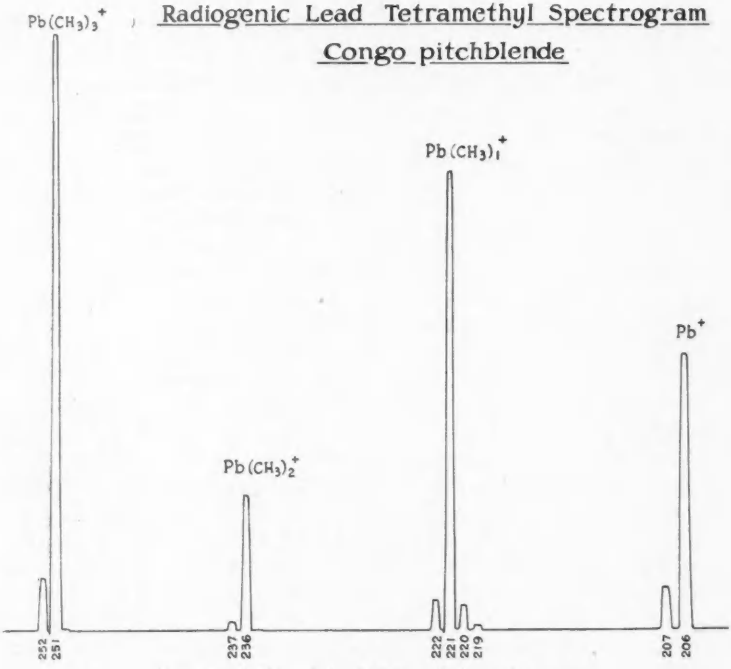

FIG. 3. Radiogenic lead tetramethyl spectrogram.

Prof. G. F Wright and Mr. H. L. Cohen of the Department of Chemistry of the University of Toronto. The method of preparation has been reported (5). Our first preparations required about 50 mgm. of lead chloride, but a revised method now being investigated using less than 10 mgm. of lead chloride has already yielded adequate samples of lead tetramethyl for mass spectrometer analysis.

ISOTOPIC CONSTITUTION OF RADIOGENIC AND ORDINARY LEADS

The relative abundances of the isotopes of common leads from various localities have been determined by the analysis techniques described in the preceding section. A number of these leads have been assigned ages from dated uranium minerals which occurred in the same geographical and geological areas, and which are believed to have been deposited at approximately the same time as the common leads.

All the ages were determined from the ratio of radiogenic Pb^{207} to Pb^{206} for lead extracted from uranium minerals, according to the well-known relation used by Nier (13)

$$\frac{N(Pb^{207})}{N(Pb^{206})} = \frac{N(U^{235})\ (\exp \lambda(U^{235})t - 1)}{N(U^{238})\ (\exp \lambda(U^{238})t - 1)}.$$

$N(Pb^{207})$, etc., refer to the number of atoms of the indicated isotope. $\lambda(U^{235})$ and $\lambda(U^{238})$ are the decay constants of the uranium isotopes. The ratio of the abundances of the uranium isotopes at the present time is 1/139. Numerical values for the ratio of Pb^{207} to Pb^{206} were taken from the isotopic analysis of uranium lead after correcting for the presence of ordinary lead on the basis of the abundance of Pb^{204}, which is not derived from uranium or thorium. This correction was small as may be seen in Table I, so that any uncertainty in the assumed isotopic constitution of ordinary lead would introduce a negligibly small error.

In Table I, both our determinations and Nier's have been listed for samples of uranium bearing minerals from Wilberforce, Katanga, and Great Bear Lake. The uraninite from Wilberforce, Ont., was exceptionally fine unaltered material free from ordinary lead; the agreement in age values is within 1%. Pitchblendes and uranium minerals formed by alteration are less suitable for age determinations. For seven samples from Katanga, Nier reported values from 620 to 665 million years, as compared to a spread of from 615 to 655 million years for five samples analyzed in this laboratory. Nier's single value for Great Bear Lake pitchblende falls within our age spread for samples from the same deposits. These comparisons provide a rough check between our values and Nier's; they also show the spread in values that can be expected for determinations made on uraninites and on the less reliable pitchblende ores.

All the ages listed in Table I have been used in an endeavor to date the ordinary lead samples whose isotopic analyses appear in Table II. Where Nier's analyses of ordinary leads have been quoted, his sample numbers have been given. As the main source of uncertainty in calculations based on the isotopic constitution of lead ores is in the assignment of the age or time of deposition of

TABLE I

ISOTOPIC ANALYSES OF RADIOGENIC LEADS AND AGES OF URANIUM MINERALS

No.	Mineral and locality	Isotopic abundances, %				Radiogenic $Pb^{207}/Pb^{206}(\%)$	Age in 10^6 years
		204	206	207	208		
1	Uraninite, Wilberforce, Ont., Canada	0.00 ±0.006	89.43	6.60	3.98	7.38 ± 0.07	1040 ± 15 *
2	" "	0.00 ±0.006	89.67	6.56	3.76	7.31 ± 0.03	1030 ± 10 *
3	" "	0.01 ±0.002	87.98	6.59	5.42	7.33 ±	1035 **
4	Pitchblende, Katanga, Belgian Congo	(Seven samples)				6.00 to 6.13	620 to 665**
5	" "	0.035 ±0.015	93.90	5.76	0.32	5.99 ± 0.04	615 ± 20 *
6	" "	0.02 ±0.01	93.68	5.82	0.51	5.99 ± 0.06	615 ± 20 *
7	" "	0.024 ±0.015	94.09	5.79	0.11	6.10 ± 0.02	655 ± 15 *
8	" "	0.05 ±0.015	92.96	6.02	0.97	6.05 ± 0.03	637 ± 20 *
9	" "	0.015 ±0.008	93.94	5.79	0.25	6.05 ± 0.03	637 ± 20 *

10	Pitchblende, Great Bear Lake, N.W.T., Canada	0.056 ±0.0016	89.02	8.69	2.23	8.88	1420 **
11	" "	0.02 ±0.01	90.63	8.29	1.10	8.83 ± 0.30	1410 ± 30 *
12	" "	0.056 ±0.007	89.47	8.47	1.78	8.93 ± 0.25	1430 ± 30 *
13	" "	0.07 ±0.03	88.90	8.43	2.61	8.39 ± 0.20	1330 ± 40 *
14	" "	0.07 ±0.015	89.57	8.44	1.90	8.59 ± 0.25	1350 ± 50 *
15	Uraninite, Huron Claim, Man., Canada	0.018 ±0.0036	81.50	13.18	5.31	15.9	2465 **
16	Monazite, Huron Claim, Man., Canada	0.010 ±0.02	10.20	1.86	87.94	17.0	2580 ± 70 **
17	Lepidolite, Huron Claim, Man., Canada	(Age based on rubidium to strontium decay)					2400 ***
18	Uraninite, Rex property, Great Slave Lake, Canada	0.073 ±0.015	86.83	10.67	2.44	11.2 ± 0.3	1850 ± 40 *
19	Pitchblende, Ace Mine, Lake Athabaska, Canada	0.00 ±0.015	89.69	9.96	0.37	11.02 ± 0.2	1820 ± 40 *
20	Pitchblende, Nicholson #4 property, Lake Athabaska, Canada	0.00 ±0.015	89.49	9.88	0.66	11.0 ± 0.2	1800 ± 40 *
21	Pitchblende, Fish Hook Bay, Lake Athabaska, Canada	0.03 ±0.015	88.18	10.35	1.46	11.30 ± 0.3	1850 ± 50 *
22	Radium Hill, Australia	0.21 ±0.015	78.70	10.34	10.78	9.30 ± 0.40	1510 ± 100*

*Analyses carried out by the authors.

**These analyses were taken from Nier's papers (13, 15). Nier's ages have been revised using the new half-life value for U^{235} of 7.07×10^8 years reported by Fleming, Ghiorso, and Cunningham (8).

***Age by Ahrens (1).

the ore, all Nier's specimens from one locality believed to be the same age have been combined, as was done by Bullard and Stanley (4), to avoid giving excessive weight to lead from any one locality. The ages assigned by Bullard and Stanley to Nier's leads of post-Cambrian age have been listed without change, and with them has been included sample No. 5 from Bolivia, believed like most deposits there to be Tertiary in age. Hence it has been given the same approximate mid-Tertiary age of 25 million years as sample No. 1 from the Casapalca Mine, Peru.

TABLE II

RELATIVE ISOTOPIC ABUNDANCES OF LEADS FROM LEAD ORES OF KNOWN AGE

Nier's Nos.	Our No.	Source	Geological age in 10^6 years	Isotopic abundances ($Pb^{204} = 1.00$)		
				206	207	208
16, 17	1	Casapalca Mine, Peru	25	18.76	15.55	38.39
11, 23	2	Arizona, U.S.A.	25	18.81	15.85	38.63
24	3	Freiberg, Saxony	25	18.07	15.40	38.0
21	4	Durango, Mexico	25	18.71	15.70	38.5
	5	Bolivia	25	18.94	15.86	39.70
9, 10	6	Washington, Idaho, U.S.A.	60	17.67	15.42	37.38
5, 6, 12, 18, 19.	7	Saxony, etc.	220	18.01	15.54	37.89
4	8	Yancey Co., N.C., U.S.A.	220	18.43	15.61	38.2
20	9	Franklin, N.J., U.S.A.	400	17.15	15.45	36.53
	10	Katanga, Belgian Congo	630	17.58	15.94	38.34
15	11	Tetraulte Mine, Que., Canada	1030	16.27	15.16	35.6
	12	Frontenac Co., Ont., Canada	1030	16.79	15.40	36.49
2, 3	13	Broken Hill, N.S. Wales	1500	16.00	15.35	35.38
1	14	Great Bear Lake, N.W.T., Canada	1400	15.93	15.30	35.3
	15	Negus Mine, Great Slave Lake, N.W.T., Canada	1850	14.63	15.27	34.46
	16	Rex, Stark Lake, N.W.T., Canada	1850	16.37	15.65	36.34
	17	Sioux Lookout, Ont., Canada	2480	14.05	14.92	33.85

Two methods have been used to date the Pre-Cambrian specimens. The common lead samples from Katanga and Great Bear Lake came from veins or mines containing uranium ores, and the ages determined for the latter have been used. In the other cases no dates are known for the deposits themselves and it has been necessary to assume that the deposits are of approximately the same age as the geological provinces in which they occur. It has been pointed out for several Pre-Cambrian shield areas that patterns of foliation, major fault zones, changes in rock types, and kinds of mineralization enable different provinces to be distinguished. It has also been found for those provinces within which there are many localities dated by radioactive minerals that all the pegmatite deposits have ages lying within a range of a very few hundreds of millions of years. Although some mineralization has undoubtedly occurred at later dates, this method probably roughly fixes the age of the majority of ores of a province.

Sample No. 11, Table II, from the Tetraulte Mine, Quebec, and sample No. 12, from Frontenac Co., Ontario, are considered to be in the Grenville geological province whose best dated locality is Wilberforce, Ont., at 1030 million years. Sample No. 13 was dated from the Radium Hill age of 1500 million years (No.

22, Table I). The value of 1850 million years, representing the maximum age of the uranium samples from Goldfields, Lake Athabaska, and from the Rex property on Great Slave Lake, has been taken as dating ordinary lead samples Nos. 15 and 16. The age value of 2480 million years for No. 17 has been estimated by averaging the two values for the Huron Claim reported by Nier with a value determined by Ahrens (1) using the rubidium–strontium method.

The relative abundances of the isotopes of common leads from ores of unknown age are given in Table III. Several of these leads have isotopic constitutions quite different from any previously reported. They will be discussed in the last section of this paper.

TABLE III

RELATIVE ISOTOPIC ABUNDANCES OF COMMON LEADS OF UNKNOWN AGE

Nier's No.	Our No.	Source	Isotopic abundances (Pb^{204} = 1.00)		
			206	207	208
13	18	Ivigtut, Greenland	14.65	14.65	34.5
	19	Horseshoe Island, Yellowknife, N.W.T., Canada	14.16	15.08	34.28
	20	Upper Canada Mine, Ont., Canada	19.60	15.22	33.62
	21	Rosetta Mine, South Africa	12.65	14.27	32.78
	22	Box Mine, Goldfields, Sask., Canada	20.88	15.74	35.39
	23	Matachewan, Ont., Canada	15.83	15.41	34.88
	24	Delhi Twp., Ont., Canada	16.07	15.47	35.17
	25	Garson Mine, Sudbury, Ont., Canada	23.35	16.98	45.57
	26	Worthington Mine, Sudbury, Ont., Canada	26.00	16.94	52.21

A LIMIT ON THE TIME OF FORMATION OF THE ELEMENTS

At the time Nier (12, 15) reported the isotopic constitution of 25 lead ores, he pointed out that the abundances of Pb^{206}, Pb^{207}, and Pb^{208} relative to Pb^{204} tended to be smaller in older ores, and suggested that this variation might be attributed to contributions of radiogenic lead from uranium and thorium. Later Alpher and Herman (2), by using certain simplifying assumptions, were able to deduce an approximate mathematical representation of this effect, and to evaluate the parameters involved.

To permit such a calculation to be made, it must be assumed that since the time of formation of the elements lead produced from the decay of uranium and thorium has been continuously added to the original lead. It is further assumed that *on the average* the relative amounts of lead, uranium, and thorium in the earth have remained the same everywhere except for the change due to the steady decay of uranium and thorium to lead. At the time of a lead mineralization a sample of lead was concentrated from a body of rock. The resulting lead ores contain negligible amounts of uranium and thorium and so constitute a permanent record of the isotopic constitution of lead in the earth's crust at the time of formation of the mineral.

If these assumptions are true, the isotopic composition of lead at t_m years before the present can be represented by the equations

$$x_m = a - \alpha V(e^{\lambda t_m} - 1),$$

[1] $$y_m = b - V(e^{\lambda' t_m} - 1),$$

and $$z_m = c - W(e^{\lambda'' t_m} - 1).$$

x_m, y_m, and z_m are the abundances of Pb^{206}, Pb^{207}, and Pb^{208} relative to Pb^{204} at time t_m, and a, b, and c are the corresponding abundances of the respective lead isotopes in the earth's crust at the present time. V and W are the present relative abundances of U^{235} and Th^{232} with respect to Pb^{204}. α is the present ratio of U^{238} to U^{235}, and λ, λ', and λ'' are the decay constants of U^{238}, U^{235}, and Th^{232} respectively. According to our assumptions, V and W are not functions of time or of the particular sample concerned.

A least squares analysis has been used to calculate the values of a, b, c, V, and W which give the closest agreement between equations [1] and the isotopic constitution of the lead ores of known age listed in Table II. This was done in the following way.

Define

$$\delta = \sum_m \{x_m - a + \alpha V(e^{\lambda t_m} - 1)\}^2 + \sum_m \{y_m - b + V(e^{\lambda' t_m} - 1)\}^2 + \sum_m \{z_m - c + W(e^{\lambda'' t_m} - 1)\}^2.$$

For the best fit, δ is a minimum, and therefore

$$\frac{\partial \delta}{\partial a} = \frac{\partial \delta}{\partial b} = \frac{\partial \delta}{\partial c} = \frac{\partial \delta}{\partial V} = \frac{\partial \delta}{\partial W} = 0.$$

The application of these conditions results in five independent linear equations in five unknowns:

$$\sum_{m=1}^{n} x_m - na + \alpha V \sum_{m=1}^{n} (e^{\lambda t_m} - 1) = 0,$$

$$\sum_m^n y_m - nb + V \sum_m (e^{\lambda' t_m} - 1) = 0,$$

$$\sum_m z_m - nc + W \sum_m (e^{\lambda'' t_m} - 1) = 0,$$

$$\alpha \sum_m x_m(e^{\lambda t_m} - 1) + \sum_m y_m(e^{\lambda' t_m} - 1) - a\alpha \sum_m (e^{\lambda t_m} - 1) - b \sum_m (e^{\lambda' t_m} - 1) + V \sum_m \{\alpha^2(e^{\lambda t_m} - 1)^2 + (e^{\lambda' t_m} - 1)^2\} = 0,$$

$$\sum_m z_m(e^{\lambda'' t_m} - 1) - c \sum_m (e^{\lambda'' t_m} - 1) + W \sum_m (e^{\lambda'' t_m} - 1)^2 = 0.$$

Using

$$\lambda = 0.154 \times (10^9 \text{ years})^{-1},$$
$$\lambda' = 0.980 \times (10^9 \text{ years})^{-1},$$
$$\lambda'' = 0.0499 \times (10^9 \text{ years})^{-1},$$
$$\alpha = 139,$$

and the isotopic abundances listed in Table II, it was found that

$$a = 18.45,$$
$$b = 15.61,$$
$$c = 38.40,$$
$$V = 0.0714,$$
$$W = 38.2(8).$$

These values are for the present time. On substituting the above numerical values in equations [1], it was then possible to plot the curves shown in Fig. 4. These curves show the mean isotopic composition of lead distributed throughout the earth's crust as a function of the time before the present.

The mathematical calculations give no unique starting points for the curves shown in Fig. 4, and therefore no unique value for the time at which uranium

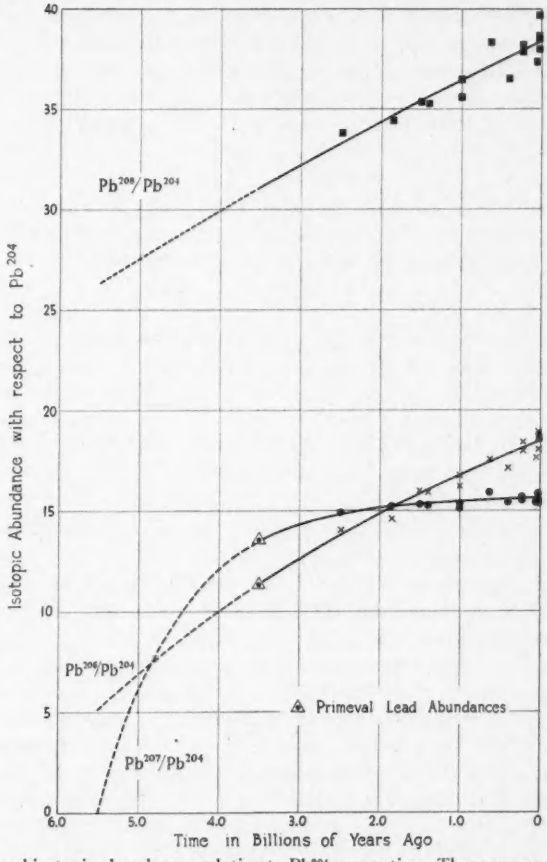

FIG. 4. Lead isotopic abundances relative to Pb^{204} versus time. These curves were obtained from a least squares fit of the data in Table II.

first began contributing to the lead isotopes. However, if we assume that equations [1] can be used to extrapolate the curves backward in time (as shown in the dotted portions of the curves of Fig. 4) a limit on the time of formation of the elements can be taken as the time at which the abundance of one of the three lead isotopes becomes negative, for this surely represents an impossible physical situation. It can be shown from either Fig. 4 or equations [1] that the abundance of Pb^{207} becomes zero 5.5×10^9 years ago. This figure may be considered a limit to the time of formation of the elements.

The figure of 5.5 billion years given as a limit to the time of formation of the elements may be in error owing to the use of incorrect physical constants, owing to the relatively few points used for determining the curves, or owing to a failure of the basic assumptions. The present uncertainty in the relative abundances of the uranium isotopes, U^{238}/U^{235}, is about 1%. The uncertainty in the decay constant of U^{235} is of the order of 1.5%, while the uncertainty in the U^{238} decay constant is only about 0.25%. It is fortunate that the position and intercepts of the Pb^{207} curve (Fig. 4) are less sensitive to changes in parameters than those of the other two. This effect can be seen by comparison of the curves reported by Alpher and Herman (2). The data used to calculate the curves were appreciably different, as was the decay constant of U^{235} for which Alpher and Herman used $0.920 \times (10^9 \text{ years})^{-1}$, and although the Pb^{206} and Pb^{208} curves shown in their paper are quite different from those of Fig. 4, the Pb^{207} curve is almost the same. Gross errors arising from the failure of basic assumptions will be discussed in the last section of this paper.

THE AGE OF THE EARTH'S CRUST

In 1946 Holmes (9) suggested an ingenious method for estimating the age of the earth's crust from the isotopic constitution of lead from lead ores of known age. More recently Bullard and Stanley (4) have modified Holmes' method, treating the experimental data by a least squares analysis rather than by Holmes' more laborious approach. Both authors used Nier's isotopic analyses of common leads (12, 15), and reported values close to 3.3 billion years (Holmes −3.35 billion; Bullard and Stanley −3.29 billion years) for the age of the earth's crust. This calculation has been repeated by the present authors using the least squares method of Bullard and Stanley (4), and basing the calculation on the experimental data given in Table II. These calculations all depend on the behavior of lead, uranium, and thorium in the outer part of the earth as set down by Holmes (9).

Holmes' method depends on several basic assumptions. It is assumed that the materials now found in the outer parts of the earth were initially so thoroughly mixed that the four isotopes of lead were present in the same relative proportions everywhere. When the crust solidified, physical and chemical processes produced small differences in the relative amounts of lead, uranium, and thorium from place to place. The lead which crystallized in the earth's crust at that time has been called *primeval lead*. As time passed, part of the uranium and thorium decayed to lead, which added to primeval lead, and changed its isotopic constitution by an amount depending on the relative proportions of lead, uranium,

and thorium present in that particular part of the crust. At a later time a sample of lead was concentrated from a body of rock to form a lead mineral containing a negligible amount of uranium and thorium. This lead provided a permanent record of the isotopic constitution of lead in the crust at that time.

In the ideal case, the isotopic constitution of lead in the crust at time t_m (and hence the isotopic composition of a lead mineral formed at time t_m) can be represented by the mathematical expressions

$$x_m = a_0 + \alpha V_m(e^{\lambda t_0} - e^{\lambda t_m})$$

[2]

and

$$y_m = b_0 + V_m(e^{\lambda' t_0} - e^{\lambda' t_m}).$$

where x_m and y_m respectively are the abundances of Pb^{206} and Pb^{207} relative to Pb^{204} at t_m years before the present, a_0 and b_0 are the corresponding abundances of primeval lead, t_0 is the time of solidification of the crust, and V_m is the abundance of U^{235} with respect to Pb^{204}. α is the present ratio of U^{238} to U^{235}, and λ and λ' are the decay constants of U^{238} and U^{235} respectively. It is assumed that V_m is a function of the particular lead mineral, but is not a function of time.

Equations [2] can be combined to obtain

$$\frac{x_m - a_0}{y_m - b_0} = \frac{\alpha(e^{\lambda t_0} - e^{\lambda t_m})}{(e^{\lambda' t_0} - e^{\lambda' t_m})}. \qquad [3]$$

The unknown parameters a_0, b_0, and t_0 must be chosen so that equation [3] most nearly fits the experimental data in Table II. This is done in the following way.

Define
$$\delta = \sum_{m=1}^{n} \omega_m\{\alpha(y_m - b_0)(e^{\lambda t_0} - e^{\lambda t_m}) - (x_m - a_0)(e^{\lambda' t_0} - e^{\lambda' t_m})\}^2$$
$$= \sum_m \omega_m \epsilon_m^2$$

where the summation extends over the n samples. ω_m is a weight that is calculated for each sample. As Bullard and Stanley (4) pointed out, the use of properly calculated ω_m provides unique solutions for a_0, b_0, and t_0 that are independent of the manner in which δ is defined, and that are the most probable solutions. For this calculation

$$\omega_m = 1/(X_m^2 + Y_m^2 + T_m^2),$$

where
$$X_m = -(e^{\lambda' t_0} - e^{\lambda' t_m})\,\delta x_m,$$
$$Y_m = \alpha(e^{\lambda t_0} - e^{\lambda t_m})\,\delta y_m,$$

and
$$T_m = \{\lambda'(x_m - a_0)\,e^{\lambda' t_0} - \alpha\lambda(y_m - b_0)\,e^{\lambda t_0}\}\,\delta t_m,$$

and where δx_m, δy_m, and δt_m are the uncertainties in x_m, y_m, and t_m.

For the present calculation, δx_m and δy_m were taken to be $\pm$ 0.1 in all cases, and δt_m was taken as $\pm$ 0.2 $\times$ 10^9 years in all but four cases. Samples Nos. 11, 12, and 14 (Table II) were believed to be better dated than the others. For these samples δt_m was taken to be $\pm$ 0.15, $\pm$ 0.10, and $\pm$ 0.10, respectively, all in

10^9 years. The age of sample No. 15 was assigned an uncertainty of $\pm 0.30 \times 10^9$ years. The assignment of these uncertainties is necessary in the least squares treatment of the data to avoid giving undue weight to younger samples. This procedure can be justified physically on the basis of uncertainties in the isotopic abundance measurements, and in the assignment of ages to lead ores from dated uranium minerals supposedly deposited at the same time.

ϵ_m is not linear in the unknowns. However, if approximate values a_0, b_0, and t_0 are chosen, we can say that

$$\epsilon \cong \bar{\epsilon} + \frac{\partial \bar{\epsilon}}{\partial a_0} \Delta a_0 + \frac{\partial \bar{\epsilon}}{\partial b_0} \Delta b_0 + \frac{\partial \bar{\epsilon}}{\partial t_0} \Delta t_0$$

which is linear in Δa_0, Δb_0, and Δt_0. Where $\Delta a_0 = a_0 - \bar{a}$, $\Delta b_0 = b_0 - \bar{b}$, $\Delta t_0 = t_0 - \bar{t}_0$, and the derivatives are evaluated for the approximate solutions. Then

$$\delta = \sum_m \omega_m \left\{ \bar{\epsilon} + \frac{\partial \bar{\epsilon}}{\partial a} \cdot \Delta a + \frac{\partial \bar{\epsilon}}{\partial b} \cdot \Delta b + \frac{\partial \bar{\epsilon}}{\partial t_0} \cdot \Delta t_0 \right\}^2.$$

For the best fit between the observed values and the theoretical equation δ is a minimum and

$$[4] \qquad \frac{\partial \delta}{\partial (\Delta a_0)} = \frac{\partial \delta}{\partial (\Delta b_0)} = \frac{\partial \delta}{\partial (\Delta t_0)} = 0.$$

Using the data in Table II and taking

$$\alpha = 139,$$
$$\lambda = 0.154 \times 10^{-9} \text{ years}^{-1},$$

and

$$\lambda' = 0.980 \times 10^{-9} \text{ years}^{-1},$$

equations [4] were solved to give

$$a_0 = 11.33,$$
$$b_0 = 13.55,$$
$$t_0 = 3.5 \times 10^9 \text{ years}.$$

DISCUSSION

The possibility of gross errors in the results which have been presented must be considered. Our value of 5.5 billion years as a limit on the time of formation of the uranium isotopes was obtained by extrapolation from the isotopic constitution of common leads, the oldest of which was dated at 2.5 billion years. Such an extrapolation is valid only if the relative amounts of lead, uranium, and thorium in the earth's crust have remained the same, except for radioactive decay, from the time of formation of the elements to the present. This difficulty has already been pointed out by Alpher and Herman (2) who wrote as follows: "It is generally believed that there was a marked increase in the amounts of uranium and thorium relative to lead in the earth's crust at the time of its formation. This implies the possibility of error in an extrapolation of the curves shown in Fig. 1 [our corresponding curves are shown in Fig. 4] to times earlier than that of crustal formation."

Our value of 3.5 billion years for the time of formation of the earth's crust is slightly higher than the 3.29 billion figure of Bullard and Stanley (4) and the 3.35 billion value of Holmes (9), but the change is not large in view of the

additional data used in our calculation. From this comparison of estimates by different investigators using different methods of calculation and in this paper additional experimental data, it seems probable that an answer of the order of 3.5 billion years is likely to be obtained as long as the calculation is based on the fundamental assumptions of Holmes' method. Alpher and Herman (2) expressed doubts about the validity of Holmes' method, but agreed that his figure of 3.35 billion years for the time of formation of the earth's crust was reasonable in view of Behr's (3) figure of 3.8 billion years from nebular recession data for the start of the expansion. Bullard and Stanley (4) pointed out that a likely cause of gross error in Holmes' method was a failure of the basic assumption that the rocks were isolated when the crust solidified, and then developed undisturbed until the time of deposition of the lead ore. The anomalous isotopic constitutions of the Sudbury leads (Nos. 25 and 26, Table III) support this criticism, although it is not easy to estimate the effect of such samples on the age of the earth's crust calculation.

Holmes assumed that all lead everywhere had the same isotopic constitution at the time of solidification of the earth's crust. He called this lead primeval lead. According to this argument, no lead found at any subsequent time could have lower isotopic abundances relative to the 204 isotope than primeval lead. We have reported one common lead from the Rosetta Mine, South Africa, listed in Table IV, whose isotopic abundances fall within the limits set on the calculated isotopic constitution of primeval lead as shown in Table IV. Primeval lead must then have isotopic abundances relative to Pb^{204} not greater than those listed for the Rosetta sample.

TABLE IV

ISOTOPIC CONSTITUTION OF PRIMEVAL LEAD

Sample	Isotopic abundances relative to $Pb^{204} = 1.00$		
	206	207	208
Rosetta Mine, South Africa	12.65	14.27	32.78
Primeval lead, calculated by Holmes (9)	10.945 $\pm$ 8 to 10%	13.51 $\pm$ 8 to 10%	
Primeval lead, calculated by Bullard and Stanley (4)	11.86 $\pm$ 1.47	13.86 $\pm$ 0.56	
Primeval lead, calculated by the present authors	11.33	13.55	
Isotopic constitution of lead from Fig. 4 at $t = 3.5 \times 10^9$ years	11.35	13.46	31.1

In Table IV are listed the abundances of the lead 206 and 207 isotopes calculated by the present authors for primeval lead at the time of formation of the earth's crust, 3.5 billion years before the present. A comparison of the isotopic abundances of the same isotopes has been made by taking values from the curves of Fig. 4 at a time 3.5 billion years before the present. The good agreement shows that the primeval lead abundances derived from the age of the earth's crust calculation fall on the extrapolated average curves drawn from the independent limit on the time of formation of the elements calculation. This check indicates that the two independent calculations are consistent with each other, but does not prove that either or both are valid.

The calculations carried out in this paper have been based on a set of leads of known isotopic constitution taken from lead ores of known age. While the two calculations are different in principle, they both depend on the total effect of all the determinations rather than on any individual one. Single samples such as Rosetta Mine, No. 22, Table III, can not be safely dated from the average curves of Fig. 4, or by subtracting the primeval lead abundances (which have rather large errors) from the isotopic abundances of the sample and then considering the Pb^{207}/Pb^{206} ratio of the remainder. This difficulty arises because of the varying amounts of lead, uranium, and thorium present in any one locality at different times in the earth's history, a fact that is well illustrated by the isotopic constitution of several of the leads in Table III which do not fit the curves of Fig. 4. A recent attempt was made by McCrady (10) to set up a time scale from which the age of ordinary leads could be obtained from relative isotopic abundance versus time curves, on the assumption that the relative amounts of uranium, thorium, and lead have remained constant (except for radioactive decay) everywhere throughout the earth's history. This assumption does not fit the experimental data given in Table III, as has already been pointed out in the preceding discussion. In the authors' opinion, no general method of dating the time of mineralization of individual lead ores from their isotopic constitution is likely to give more than very approximate ages. But investigations based on a number of isotopic analyses of leads from different localities in any particular geological province would almost certainly provide a sound basis for fixing the time of mineralization of the lead. Such studies are also likely to provide specific information about the origin of lead ores, and about the chemical and physical processes by which galena is concentrated as a mineral in nature.

ACKNOWLEDGMENTS

The authors are indebted to Prof. F. G. Smith, whose valuable discussions and contributions of samples have greatly assisted in this investigation. The authors also wish to express their thanks to Prof. J. T. Wilson and Prof. G. F Wright for their assistance in this research, and to Prof. W. H. Watson for reading the manuscript.

REFERENCES

1. Ahrens, L. H. and Gorfinkle, L. G. Nature, 166: 149. 1950.
2. Alpher, R. A. and Herman, R. C. Phys. Rev. 84: 1111. 1951.
3. Behr, A. Astron. Nachr. 279: 97. 1951.
4. Bullard, E. C. and Stanley, J. P. Suomen Geodeettisen Laitoksen Julkaisuja, Veröffentlichungen des Finnischen Geodätischen Institutes, No. 36, 33. 1949.
5. Collins, C. B. and Freeman, J. R. Trans. Roy. Soc. Can. (3d. ser.) IV, 45: 23. 1951.
6. Collins, C. B., Freeman, J. R., and Wilson, J. T. Phys. Rev. 82: 966. 1951.
7. Dibeler, V. H. and Mohler, F. L. J. Research Natl. Bur. Standards, 47 (No. 5): 337. 1951.
8. Fleming, E. H., Jr., Ghiorso, A., and Cunningham, B. B. Phys. Rev. 82: 967. 1951.
9. Holmes, A. Nature, 157: 680. 1946; 159: 127. 1947; 163: 453. 1949.
10. McCrady, E. Trans. Am. Geophys. Union. 33: No. 2. 1952.
11. Murphey, B. F. and Nier, A. O. Phys. Rev. 59: 771. 1941.
12. Nier, A. O. J. Am. Chem. Soc. 60: 1571. 1938.
13. Nier, A. O. Phys. Rev. 55: 153. 1939.
14. Nier, A. O. Phys. Rev. 77: 789. 1950.
15. Nier, A. O., Thompson, R. W., and Murphey, B. F. Phys. Rev. 60: 112. 1941.
16. Reese, R. M., Dibeler, V. H., and Mohler, F. L. J. Research Natl. Bur. Standards, 46 (No. 2): 79. 1951.

FISSION YIELDS OF THE STABLE AND LONG-LIVED ISOTOPES OF CESIUM, RUBIDIUM, AND STRONTIUM AND NUCLEAR SHELL STRUCTURE[1]

By D. R. Wiles,[2] B. W. Smith,[3] R. Horsley,[4] and H. G. Thode

ABSTRACT

The relative yields of the isotopes of cesium, rubidium, and strontium from thermal neutron fission of U^{235} have been determined mass spectrometrically. The cesium isotope yields are combined with those obtained previously for the xenon isotopes to give high precision yields for mass chains from 131 to 137. In this work neutron capture reactions have been considered and corrections made where these take place to an appreciable extent. The results give further evidence of abnormal yields in the 82 neutron shell region. The half-life of Cs^{137} was determined and found to be 33 ± 2 years.

INTRODUCTION

Previous mass spectrometer investigations (14, 8) of the stable and long-lived isotopes of xenon and krypton, formed from the fission of U^{235}, revealed for the first time the existence of "fine structure" in the mass yield curve. Kr^{84}, Xe^{133}, and Xe^{134} were found to have abnormally high yields—Xe^{134} having a yield about 30% above the smooth curve drawn through adjacent points. These high yields are undoubtedly due to the mass chains in question having members with 50 and 82 neutrons. It should be pointed out that "fine structure" in the Kr^{84} mass range is not certain, in view of the steepness of the yield curve at this point and the relatively low yields. Glendenin (3) has suggested a chain branching mechanism to explain these yields. He has postulated that nuclides with 83 neutrons, one more than a closed shell, will have a certain probability of emitting neutrons when formed as a primary fission product. This mechanism does explain qualitatively some of the yield values obtained between masses 131 and 136. The fission yields of the cesium, rubidium, and strontium isotopes, which fall in mass chains overlapping and adjacent to the mass chains of xenon and krypton studied previously, are of considerable interest. If the abnormal yields of certain mass chains are due completely or in part to chain branching, then adjacent chains will also have abnormal yields (yields differing from the interpolated values of the smooth fission yield curve). The fission chains in the two mass regions being studied are given in Tables I and II. It is seen that mass chains 133, 135, and 137 end in stable or long-lived isotopes of cesium, and mass chains 85, 87, 88, and 90 end in stable or long-lived isotopes of rubidium and strontium respectively.

Inghram, Hess, and Reynolds have already reported (7) on the abundances of the cesium isotopes from fission measured mass spectrometrically. Their results indicated high relative yields for Cs^{135} and Cs^{137}. If their relative abundance data for Cs^{133} and Cs^{137} are normalized to 7.43% for the 133 mass chain yield determined

[1] *Manuscript received September 8, 1952.*
Contribution from the Department of Chemistry, Hamilton College, McMaster University, Hamilton, Ont.
[2] *Present address: Department of Chemistry, Massachusetts Institute of Technology, Cambridge, Mass., U.S.A.*
[3] *Present address: Isotope Products Ltd., Oakville, Ont.*
[4] *Present address: Department of Physics, University of Saskatchewan, Saskatoon, Sask.*

TABLE I

FISSION PRODUCT CHAINS AND CHAIN BRANCHING IN THE HIGHER MASS RANGE

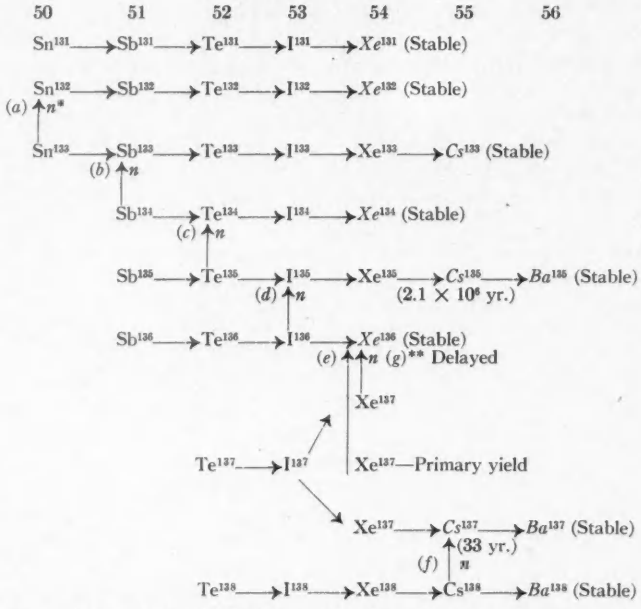
NUCLEAR CHARGE
50
51
52
53
54
55
56
Sn131 → Sb131 → Te131 → I131 → Xe131 (Stable)
Sn132 → Sb132 → Te132 → I132 → Xe132 (Stable)
(a) n*
Sn133 → Sb133 → Te133 → I133 → Xe133 → Cs133 (Stable)
(b) n
Sb134 → Te134 → I134 → Xe134 (Stable)
(c) n
Sb135 → Te135 → I135 → Xe135 → Cs135 → Ba135 (Stable)
(d) n
(2.1 × 10⁶ yr.)
Sb136 → Te136 → I136 → Xe136 (Stable)
(e) n (g)** Delayed
Xe137
Te137 → I137
Xe137—Primary yield
Xe137 → Cs137 → Ba137 (Stable)
(33 yr.)
(f) n
Te138 → I138 → Xe138 → Cs138 → Ba138 (Stable)

Vertical arrows lettered (a) to (f) indicate the branching of a chain by instantaneous emission of a neutron from a primary fission product having 83 neutrons.

***Delayed neutron activity (g) is 0.2% of fission.*

TABLE II

FISSION PRODUCT CHAINS AND CHAIN BRANCHING IN THE LOWER MASS RANGE

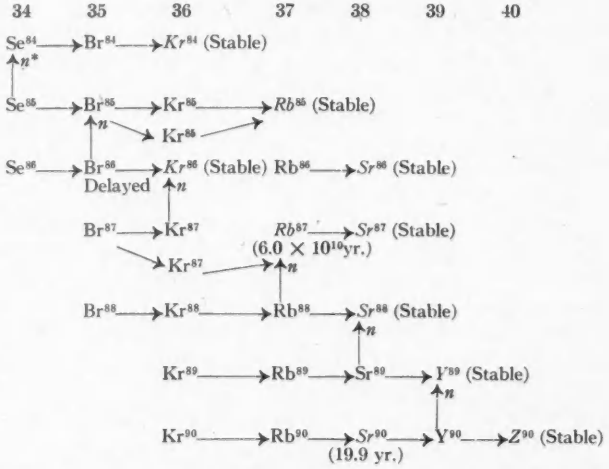

Vertical arrows indicate the branching of a chain by emission of a neutron from a primary fission product having 51 neutrons.

in this laboratory for Xe^{133}, then the yields of these chains become 7.43, 9.18, and 6.94% respectively (8, 1). (See footnote on page 423.)

This high yield indicated for Cs^{135} cannot be satisfactorily explained by the Glendenin mechanism and it does not seem to be consistent with other fission yield data. Because of this, and because Inghram, Hess, and Reynolds were unable in their work to correct for the presence of normal Cs^{133} contamination, which may have been introduced in their extraction process, we have repeated their work on a number of different samples of uranium irradiated under different conditions. In addition we have measured the Rb^{85}/Rb^{87} and Sr^{88}/Sr^{90} ratios in fission product rubidium and strontium to determine whether there is any evidence of abnormal yields in this mass range. We have also had occasion to determine the half-life of Cs^{137} using the mass spectrometer abundance data from four samples of different ages.

EXPERIMENTAL

Cesium and Rubidium

The procedure for the simultaneous isolation of carrier-free cesium and rubidium from irradiated uranium was as follows. The uranium was dissolved in nitric acid (6*N*) and the solution was evaporated to crystals. The crystals were dissolved in diethyl ether and the fission products separated from this solution by several extractions with small portions of dilute nitric acid. Ferric ion was added to the aqueous portion and precipitated as the hydroxide with ammonia gas, the supernatant liquid containing the rubidium, cesium, barium, and strontium and void of all the hydroxide forming elements. To the supernatant liquid was added ammonium ion and the subsequent precipitation of the ammonium chloroplatinate carried down only the cesium and rubidium. The supernatant solution at this point was used for subsequent isolation and purification of strontium. The chloroplatinate crystals were dissolved in hot water and the platinum was removed by reduction with formic acid. The carrier-free cesium and rubidium were then converted to the nitrate by repeated evaporation with nitric acid. The resultant nitrates were in a satisfactory form for mass spectrometer analysis.

In order to determine the amount of contamination of natural cesium and rubidium a blank was prepared in the following manner. Two disks of equal weight were cut from an uranium rod and after irradiating one of them, both were dissolved in equal volumes of nitric acid. Half of the volume of one of these samples was combined with half of the volume of the other to make a synthetic sample having twice as much stable rubidium and cesium contamination as the original active solution.

The simultaneous separation of rubidium and cesium was then carried through with both samples as in the procedure outlined above. The comparison of the abundances of the isotopes in the two samples makes possible the determination of the fission product isotope abundances.

Strontium

The isolation of carrier-free strontium was completed by the following process. The strontium solution, after the chloroplatinate precipitation just described,

was evaporated to dryness and fumed. Contaminants at this point were silica, platinic chloride, some organic matter, and small amounts of iron and uranium. The residue was dissolved in dilute hydrochloric acid, and 2 mgm. of ferric ion were added. This was precipitated as ferric hydroxide at pH 9 with ammonium carbonate. This caused the quantitative sorption of strontium carbonate and/or strontium hydroxide. In this way the desired component was separated from all substances soluble in basic solutions.

Mass Spectrometer Analysis

Two instruments were used in this work—(*a*) a double focusing mass spectrometer (2), with a "Shaw type" (12) ion source, and (*b*) a conventional sector type mass spectrometer with a heated filament ion source (6). The double focusing mass spectrograph, recently converted to a mass spectrometer, employs an ion source of the Shaw type in which a tungsten or columbium crucible is filled with the sample to be analyzed. The crucible is heated by electron bombardment from a tungsten filament which surrounds the crucible. Positive ions formed inside the crucible at elevated temperatures are accelerated through a pin-point hole in the cap covering the crucible to the hole in the shield by the same potential which attracts the electrons to the crucible. A further accelerating voltage of 3000 to 6000 v. is applied between the shield and the entrance slits.

Analyses were made by measuring singly-charged ions emitted from the oxide of the element under study. The oxides were used because they were found to give steadier emission than any other compounds investigated. The crucible temperature of cesium and rubidium analyses was estimated at between 600 and 700°C. Strontium analyses required much higher temperatures in the range between 1700 and 1800°C.

Identical analyses were conducted with the 90 degree mass spectrometer using a heated filament ion source. Ions of cesium and rubidium were produced from the oxides at filament temperatures estimated to be between 600 and 650°C. using an optical pyrometer.

Sample Size

It was found that satisfactory ion currents could be obtained with very small samples of material. For cesium and rubidium these samples amounted to the order of 0.1 and 0.02 μgm. respectively, whereas for strontium samples of the order of 0.5 to 1 μgm. were required. This high efficiency of ion production required that the crucibles and filaments used for heating the samples be free from small traces of impurities, which might give rise to ion currents in the mass range being studied. In practice each crucible and filament was tested under operating conditions for residual ion currents before the addition of a sample.

Isotope Fractionation

Experiments were carried out to determine the amount of isotope fractionation, if any, which occurred during the thermal emission from the samples. Microgram samples of cesium and rubidium were analyzed continuously for six to eight hours using both the heated crucible source in the double focusing

mass spectrometer and the filament source in the conventional spectrometer. In one case using surface ionization from a heated filament, isotopic ratios Cs^{133}/Cs^{137} were obtained over a period of three days, the total running time being about sixteen hours. In this case there was an apparent isotope fractionation. The average result obtained over the first two hours differed from that of the last two hours by about 2%. In all other cases with both the heated filament and Shaw type crucible sources isotope fractionation was less than the error of the measurement. In general, the isotope ratios obtained over a six-hour period were averaged to give a final result. It seems reasonable to assume that under the conditions of our experiments any error in isotopic ratios due to isotope fractionation at the ion source is less than ± 1%.

RESULTS

Cesium

Table III gives the irradiation data available for the five samples investigated. Eight separate determinations were made, three on sample 1, two on sample 2,

TABLE III

URANIUM IRRADIATION DATA

Sample No.	Reactor	Time in reactor	Thermal neutron flux, neutron/cm.²/sec.*	Xe 136/132 ratio	Gain in Xe^{136} due to neutron capture of Xe^{135}
1	Oak Ridge	Nov. 17–Dec. 5, 1945, 18 days	5.9×10^{11}	1.530	6.0%
2	N.R.X. Chalk River	Aug. 11, 1948	—	—	—
3	N.R.X. Chalk River	Aug. 9–18, 1950 201 hr.	2.2×10^{12}	—	11% est.
4	N.R.X. Chalk River	Dec. 6–27, 1949 21 days	—	1.430	0%
5	N.R.X. Chalk River	April 3–6, 1951 56.8 hr.	2.1×10^{12}	1.565	9.5%

**Flux was estimated from data contained in Chalk River Report No. C.R.E. 414—"Some Data on Pile Irradiation" by I. L. Wilson.*

and one each on samples 3, 4, and 5—sample 4 being irradiated in a sheath of cadmium. The results are given in Table IV. Column 4 gives the cesium isotope ratios obtained with the two mass spectrometers described above. Columns 5 and 6 give the same ratios corrected for β decay and neutron absorption, respectively. Finally, column 7 gives the absolute yields of the Cs^{133}, Cs^{135}, and Cs^{137} chains normalized at 7.43* % for the 133 chain.

In correcting the yields for neutron absorption only the reaction

[1] $$Xe^{135} + n \rightarrow Xe^{136}$$

has been considered. The extent of this reaction can be determined from a study of the xenon isotope yields and will depend on the neutron flux density.

**Values were normalized at 7.43 for 133 mass chain. The previous 6.3% yield for Xe^{133} (8) has been revised in accordance with the recently reported 3.28% I^{131} yield (1, 9) and a further small correction upward has been made to take care of some side reaction which occurs at high flux values. Unpublished work in this laboratory.*

TABLE IV

YIELDS OF CESIUM ISOTOPES IN THERMAL NEUTRON FISSION OF U^{235}

Sample run	Time after irradiation, years	Cesium isotope	Mass spec. isotope ratio	Ratio corrected for Cs^{137} decay*	Ratio corrected for neutron capture	Absolute fission yield,†%
1–1	4.60	133	1.215	1.110	1.110	7.43
		135	1.090	0.995	1.045	7.10
		137	1.000	1.000	1.000	6.72
1–2	4.64	133	1.215	1.110	1.110	7.43
		135	1.100	1.005	1.070	7.16
		137	1.000	1.000	1.000	6.72
1–3	5.65	133	1.225	1.095	1.095	7.43
		135	1.115	0.995	1.060	7.16
		137	1.000	1.000	1.000	6.78
2–1	2.1	133	1.115	1.070	1.070	7.43
		135	1.045	1.005	—	—
		137	1.000	1.000	1.000	6.94
2–2‡	2.1	133	1.120	1.075	1.075	7.43
		135	1.400	1.000	—	—
		137	1.000	1.000	1.000	6.94
3–1	0.4	133	1.105	1.095	1.095	7.43
		135	0.950	0.940	1.055	7.16
		137	1.000	1.000	1.000	6.78
4–1§	1.48	133	1.135	1.100	—	7.43
		135	1.100	1.065	—	7.21
		137	1.000	1.000	—	6.78
5–1	0.25	133	1.100	1.100	1.100	7.43
		135	0.975	0.975	1.075	7.27
		137	1.000	1.000	1.000	6.78

Absolute yields, %

Mass	This work average	Inghram, Hess, and Reynolds (7)**
133	7.43	7.43
135	7.18	9.18
137	6.81	6.94

Correction based on Cs^{137} half-life of 35 years.

†*Values normalized at 7.43 for 133 mass chain. See footnote on page 423.*

‡*Sample 2-2 was the same as sample 2-1 with added uranium and reagents to determine Cs^{133} contamination.*

§*Cs isotopes extracted from uranium metal irradiated inside a sheath of cadmium. Neutron energies >1 ev.*

**It is now apparent that Inghram, Hess, and Reynolds (7) were unable to make satisfactory correction for neutron capture reactions. Private communication.*

Insofar as the Xe^{136} yield is increased by reaction 1, the yield of Xe^{135} and, therefore, of Cs^{135} will be decreased by an equivalent amount. Sample 4 irradiated in a sheath of cadmium would not be expected to show much burning of Xe^{135} to Xe^{136}. The correction for neutron adsorption for this sample is, therefore, taken as zero. For the other samples the correction is made by comparing the ratio Xe^{136}/Xe^{132} obtained with that found for the cadmium shielded sample. In this way the percentage increase in Xe^{136} due to neutron absorption (reaction 1) is determined. The Xe^{136}/Xe^{132} ratios obtained previously (15) are plotted in Fig. 1 as a function of neutron flux. The base level value for the cadmium shielded sample is also shown. In the case of samples 1 and 5 the extent of burning of Xe^{135} was determined directly from xenon isotope measurements. In the other cases the neutron flux used had to be estimated and the correction read from Fig. 1.

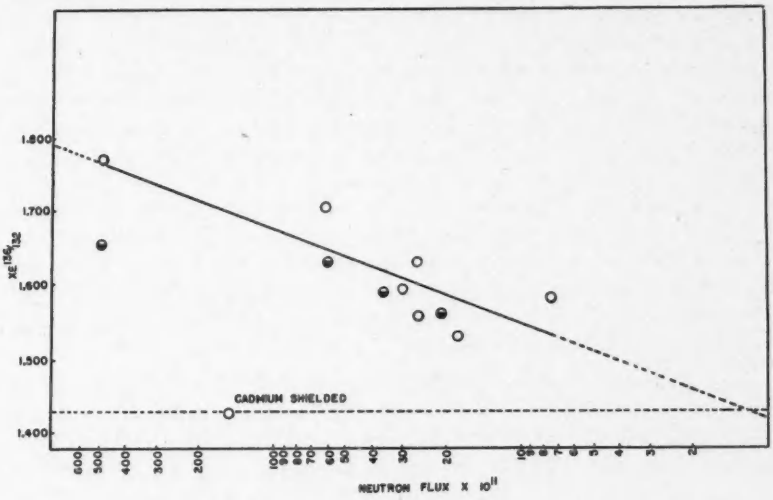

FIG. 1. Xe^{136}/Xe^{132} versus neutron flux.

It might be argued that the above procedure for correcting the cesium yields for neutron absorption is not justified as cadmium shielded samples irradiated with epithermal and fast neutrons might have a totally different distribution of isotopes. However, a large number of samples have been investigated to date and only the relative yields Xe^{136} and Cs^{135} seem to change appreciably in the low flux range, depending on the extent of cadmium shielding.* The relative yields of the isotopes Kr^{83}, Kr^{84}, Kr^{86}, Xe^{131}, Xe^{132}, Cs^{133}, and Cs^{137} remained constant within 1 or 2 %.

Finally, if the extent of reaction 1 is determined from our measurements as indicated above then the thermal neutron capture cross section of Xe^{135} can be

**It has been observed recently that the yields of Kr^{86} and Xe^{134} do vary to some extent with irradiation conditions (unpublished work of R. K. Wanless and H. G. Thode).*

calculated if the flux is known. The fact that these calculations lead to reasonable values of the capture cross section is further evidence that the method used to correct the cesium isotope fission yields for neutron absorption is satisfactory.

Cs^{133} Contamination

Because the Cs^{133} is used as the point of normalization for the 135 and 137 chains, the possibility of Cs^{133} contamination in either or both of the reagents and the original uranium metal is extremely important.

The results of the analyses of the blank samples (See Table IV, Samples 2-1, and 2-2) indicate no contamination in either the reagents or the metal used in this sample. In the other analyses the same sources of uranium metal and reagents were used, but nevertheless the Cs^{133}/Cs^{137} ratios indicate a slightly higher Cs^{133} content. This is difficult to account for inasmuch as the entire set of results show a uniformity for the Cs^{133}/Cs^{137} ratios (as corrected for Cs^{137} decay, see column 5, Table IV), which would not be expected if the original uranium samples contained appreciable amounts of stable Cs^{133}.

Further substantiation for the nonexistence of stable contamination is indicated by the agreement between the Cs^{137} half-life calculated from the mass spectrometer data of Table IV as compared to that obtained by radiochemical means. Since the Cs^{133}/Cs^{137} ratio is used in the calculations, any extraneous Cs^{133} will be reflected in the value obtained. For example, if the Cs^{133}/Cs^{137} ratio of sample 5-1 should be altered by a 3% increase in the Cs^{133} content (i.e. from 7.4 to 7.6) then the half-lives resulting would be of the order of 42 to 46 years. These values differ markedly with the published half-life with which our other results agree. From our results we believe the upper limit for stable Cs^{133} contamination to be of the order of 1% of the absolute yield.

Half-life of Cs^{137}

Cs^{137} is reported to have a half-life of from 33 to 37 years (9, 11). The Cs^{133}/Cs^{137} ratio will, therefore, increase with time. The data of Table IV may be used to calculate the half-life of Cs^{137}. The results of these calculations are given in Table V. It should be pointed out that some variation in the 133 mass yield

TABLE V

Cs^{137} HALF-LIFE FROM MASS SPECTROMETRIC ABUNDANCE DATA

Sample run	Decay time, years	Cs 137/133 ratio	Ratio N/N_0*	Elapsed time, years	Half-life $T_{1/2}$, years
1–2 (*a*)	4.64	.8230	(*a*)/(*c*)	4.24	31
1–3 (*b*)	5.65	.8163	(*a*)/(*d*)	4.39	31
3–1 (*c*)	0.4	.9050	(*b*)/(*c*)	5.25	35
5–1 (*d*)	0.25	.9090	(*b*)/(*d*)	5.4	35
				Average	33 ± 2

See Table IV.

**From decay equation* $\frac{Cs^{137}}{Cs^{133}}(a) \Big/ \frac{Cs^{137}}{Cs^{133}}(c) = \frac{N}{N_0} = e^{-0.693\, t/T_{1/2}}$ *where* t = *difference in decay time between samples* (*a*) *and* (*c*), *etc.*

may occur owing to neutron capture reactions, etc., which would introduce an error in the half-life determinations, particularly for samples irradiated at high flux values. (See footnote p. 425.)

Rubidium

The mass spectrometer abundance data for the rubidium isotopes extracted from sample 2, Table IV, are given in Table VI. In the case of the cesium isotopes,

TABLE VI

RELATIVE YIELDS OF RUBIDIUM ISOTOPES FROM U^{235} FISSION

Rb isotope	Relative abundance F.P. Sample 2	Relative abundance F.P. sample+blank	Relative abundance corrected for normal contamination	Relative abundance corrected for Kr^{85} decay	Fission yield, %
85	0.442	0.506	0.374	0.475	1.3*
87	1.00	1.00	1.00	1.00	2.75

**Normalized at 1.3 for mass 85 from mass fission yield curve.*

blank experiments showed little or no contamination with normal Cs^{133} from the uranium or reagents. However, the fission product rubidium was found to contain normal rubidium as an impurity. The mass spectrometer data for sample 2 and for sample 2 plus blank in columns 2 and 3 indicate the extent of this contamination. The corrected isotopic ratios given in column 4 were calculated as follows:

Let the ratio of the fission yields of Rb^{85} and Rb^{87} be $1/a$.
If x is the amount of contamination of Rb^{87},
then 2.6 x* will be the amount of contamination of Rb^{85}.
Let R = ratio Rb^{85}/Rb^{87} from Fission Product Sample 2.
Let R^1 = ratio Rb^{85}/Rb^{87} from Sample 2 + blank
(blank = equal weight of unirradiated uranium + reagents).
The measured ratio for F. P. Sample 2 then is given by

$$R = \frac{1 + 2.6x}{a + x} = 0.442$$

and

$$R^1 = \frac{1 + 5.2x}{a + 2x} = 0.506.$$

Hence $1/a = 0.374$.

The isotopic ratio given in column 5 has been corrected to allow for the decay of 9.4-year Kr^{85}. It is assumed that 25% of the 85 mass chain decays through this isomer and 75% through the independent 4.38-hr. Kr^{85} (16).

Strontium

Three fission product samples of strontium were investigated mass spectrometrically, the results are tabulated in Table VII. It was not necessary to run

**Normal isotopic abundance of Rb^{85}/Rb^{87} taken as 2.6.*

TABLE VII

RELATIVE YIELDS OF STRONTIUM ISOTOPES FROM FISSION ($U^{235} + n$)

Sample	Age, years	Mass	Mass spectrometer ratio	Ratios corrected for Sr^{90} decay
1	5.65	88 90	0.87 1.00	0.71 1.00
2	4.66	88 90	0.80 1.00	0.71 1.00
3	2.12	88 90	0.65 1.00	0.61 1.00
Average		88 90		0.68 1.00

blanks to determine the extent of normal strontium in the fission product material since of the natural isotopes of strontium only one, Sr^{88}, is produced in fission. Thus an accurate measure of Sr^{88} in the sample from normal contamination can be calculated from the amount of Sr^{86} present. The ratios of Sr^{88} to Sr^{90} given in Table VII are corrected for normal contamination in this way. The relative yield of 19.9-year Sr^{90} (10) was obtained by extrapolating to zero time to correct for decay.

DISCUSSION

The relative fission yields of the rubidium and strontium isotopes are in fair agreement with interpolation values from the mass vs. yield curve. These results taken together with the yield data reported earlier for the krypton isotopes indicate little or no "fine structure" in the 50 neutron shell range for U^{235} slow neutron fission.

It is just possible that some "fine structure" does exist in this mass range owing to closed shell effects, but that it does not show up because of the steepness of the curve and the relatively low yields at this point. In this case the "fine structure" should be more evident for U^{233} slow neutron fission since the krypton, rubidium, and strontium isotopes then appear near the top of the yield curve.

Nuclear Shell Structure in Fission

The high precision mass spectrometer yields obtained in the xenon and cesium isotope range (masses 131 to 137) are given in Table VIII, column 3. It is clear from Fig. 2 that the mass spectrometer yield values do not fall on a smooth mass vs. yield curve. Masses 133 and 134 are for example highly favored in the fission process. If we assume that the distribution of both charge and mass fundamentally follow simple probability laws, then any "fine structure" is due to other effects superimposed on the elementary fission process. It has been suggested earlier that these abnormal yields are due to closed shell effects in atomic nuclei, since the mass chains in question have members with 82 neutrons, a most stable configuration. If this is true then either nuclides with 82 neutrons are favored in fission according to some rule depending on their stability, or

TABLE VIII

MASS SPECTROMETER FISSION YIELDS IN NEIGHBORHOOD OF THE 82 NEUTRON SHELL ($U^{235} + n$)

Mass chain	Isotope measured	M.S. yields, %	Departure† from smooth curve (%absolute amount)	Departure predicted by Glendenin mechanism, %
131	Xe^{131}	3.28*	—	—
132	Xe^{132}	4.92	—	—
133	Xe^{133}, Cs^{133}	7.43	1.3 high	1.1 high
134	Xe^{134}	8.64	1.7 high	1.1 high
135	Cs^{135}	7.16	—	—
136	Xe^{136}	7.10	0.2 low	0.8 low
137	Cs^{137}	6.83	0.6 low	1.2 low

Values were normalized at 3.28 for the 131 mass chain (9, 1).
†Smooth curve arbitrarily drawn (solid line Fig. 2).

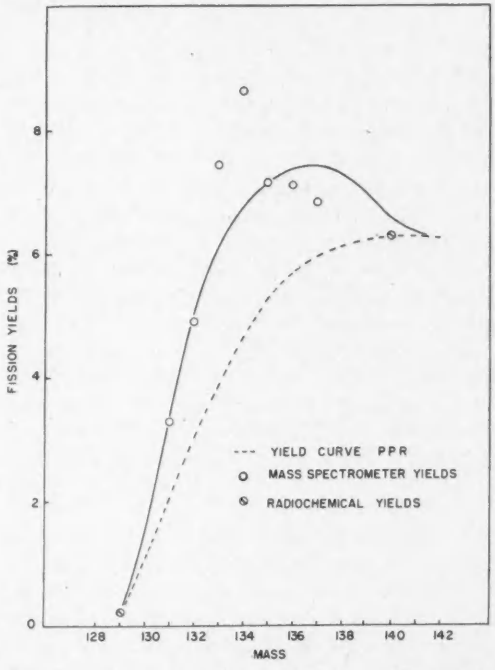

FIG. 2. Mass spectrometer fission yields for masses 131 to 137 ($U^{235} + n$).

nuclides with loosely held neutrons, one more than a closed shell, emit neutrons immediately after fission thereby changing the yields of various mass chains. This latter scheme was first suggested by Glendenin. According to his suggested mechanism, nuclides with 83 neutrons, or a certain fraction of these, when

formed as primary fission products will have sufficient energy to boil out the loosely held 83rd neutron. Table I shows the chain branching that would result in the mass region studied.

In order to estimate the extent of these side reactions, "*a*" to "*f*", Table I, it is necessary, therefore, to know something about the primary, or independent, yields. Although little is known about the primary yields of the individual members of a chain, Coryell, Edwards, and Glendenin (4) have proposed a theory of equal charge displacement, which seems to fit the available primary yield data fairly well. Using this theory Glendenin has estimated the extent of reactions "*a*" to "*f*" (Table I). As a result of this chain branching, the yields of the mass chains in question will be high or low according to column 5 (Table VIII). The departure of the experimental yields from an arbitrarily drawn solid line smooth curve (Fig. 2) is given in column 4 for comparison. Although the position of the smooth curve is arbitrary, it is quite evident that masses 133 and 134 are high and masses 136 and 137 are low as predicted by the Glendenin mechanism.

The Glendenin mechanism requires, however, that yields greater than the smooth curve values must be counterbalanced exactly in their totals, by yields in other chains, which are below the smooth curve. If the solid curve in Fig. 2 were raised in the 135–137 mass range, then this would be very nearly true. However, the curve is already well above the smooth yield curve of the Plutonium Project Report and must fall sharply after mass 136. In this connection there has been a continual revision upward in the yield of I^{131} (9, 1), which in turn results in the much higher yields for masses 131 to 137, whose relative values have been determined mass spectrometrically. The revised yields are given in Table VIII and plotted in Fig. 2. The yields in this mass range are now much higher than those given by the smooth curve in the Plutonium Project Report. The result is a decided hump on the side of the fission yield curve.

To explain these facts it was suggested in this laboratory (17) that in addition to the Glendenin effect, nuclides with 82 neutrons are favored in the primary fission process, that is in the process which occurs before the fission neutrons are boiled off. Such an effect would only be appreciable for the masses 133, 134, 135, and 136 since the increased yield of the primary fragment with 82 neutrons would certainly be a function of its displacement from the Bohr–Wheeler stability curve.

One would expect that the Glendenin effect, which depends on the instability of nuclides with 83 neutrons, would decrease from mass chains 131 to 138, as the member of the chain with 83 neutrons approaches the Bohr–Wheeler stability curve (see Table I), whereas the primary fission process effect which depends on the extra stability of the 82 neutron shell would increase.

The "fine structure" and high total yields found for the mass range in question would seem to result from a combination of the two effects discussed above. By establishing empirically the functional relationship between the two effects and nuclear stability, the results can be accounted for fairly well.

Since this work (13, 17) was done, Glendenin, Steinberg, Inghram, and Hess (5) have reported abnormally high yields in the mass 98–100 range. They point

out that the high yield at Mo^{100} suggests a preference for this mass in the fission act, perhaps as the complement of a preferred 82-neutron shell in the heavy fragment, since mass 100 is the complement of mass 133 and/or 134, both of which have high yields. This result then would seem to confirm our suggestion of a preference for nuclides with 82 neutrons in the initial fission process. If the high yields at masses 133 and 134 were wholly due to a neutron boil-off process after fission, the complement mass would be unaffected.

Experiments are in progress to determine the extent of "fine structure" in the mass yield curve in the neighborhood of closed shells for the fission of Pu^{239}, U^{233}, U^{238}, and Th^{232} with thermal and fast neutrons. These experiments should give us a crucial test for the Glendenin mechanism, as any fine structure in the yield curve due to this mechanism will be shifted, depending upon the number of neutrons in the isotope undergoing fission, whereas fine structure due to closed shell effects in the primary process would not be shifted. On the other hand with very high energy neutron fission, one might expect the preferential formation of 82-neutron fragments to decrease and the fission process to become less selective.

ACKNOWLEDGMENTS

We wish to acknowledge financial assistance from the National Research Council of Canada and from the Atomic Energy of Canada Limited who made this work possible. Also, we wish to thank R. H. Tomlinson who assisted with several of the final samples, and to thank T. Church and L. Yaffe for their co-operation in connection with sample irradiations.

REFERENCES

1. Bartholomew, Rosalie M., Brown, F., Hawkings, R. C., Merritt, W. F., Thode, H. G., and Yaffe, L. Forthcoming publication.
2. Dempster, A. J. Proc. Am. Phil. Soc. 75: 755. 1935.
3. Glendenin, L. E. Ph.D. Thesis, Mass. Inst. Technol. Cambridge, Mass. 1949.
4. Glendenin, L. E., Coryell, C. D., and Edwards, R. R. Radiochemical studies: the fission products. Book 1, Paper 52, *edited by* Coryell, C. D. and Sugarman, N. McGraw-Hill Book Company, Inc., New York and London. 1951.
5. Glendenin, L. E., Steinberg, E. P., Inghram, M. G., and Hess, D. C. Phys. Rev. 84: 860. 1951.
6. Graham, R. L., Harkness, A. L., and Thode, H. G. J. Sci. Instruments, 24: 119. 1947.
7. Inghram, M. G., Hess, D. C., and Reynolds, J. H. Phys. Rev. 76: 1717. 1949.
8. Macnamara, J., Collins, C. B., and Thode, H. G. Phys. Rev. 78: 129. 1950.
9. Pappas, A. of Mass. Inst. Technol. at XII International Congress of Pure and Applied Chemistry, Section II, Paper 20. September, 1951.
10. Powers, R. I. and Voigt, A. F. Phys. Rev. 79: 175. 1950.
11. Seaborg, G. T. and Perlman, I. Revs. Modern Phys. 20: 585. 1948.
12. Shaw, A. E. MDDC 308, Atomic Energy Commission, 1946.
13. Smith, B. W. M.Sc. Thesis, McMaster University, Hamilton, Ont. 1951.
14. Thode, H. G. and Graham, R. L. Can. J. Research, A, 27: 1. 1947.
15. Thode, H. G., Macnamara, J., and Collins, C. B. Chalk River Rept. CL-172, April 8, 1949; also, CR-PRG-49, October, 1948.
16. Thode, H. G. and Shields, R. B. Repts. Progress Phys. 12: 1. 1949.
17. Wiles, D. R. M.Sc. Thesis, McMaster University, Hamilton, Ont. August, 1950.

RESONANT SCATTERING OF SLOW NEUTRONS[1]

By B. N. Brockhouse

ABSTRACT

A method is described for measurement, as a function of neutron energy, of the scattering cross section for slow neutrons of materials having high absorption. The necessary corrections are discussed. The results are normalized to a vanadium scattering cross section of 5.07 barns inferred from the measured total cross section, $\sigma_T = 5.07 + 5.29(0.025/E(\text{ev.}))^{\frac{1}{2}}$. Measurements are presented for the low energy neutron resonances in cadmium, samarium, gadolinium, dysprosium, europium, rhodium, and indium. The single level Breit-Wigner formula is accurately obeyed for cadmium and samarium but not for gadolinium in which two resonances contribute. The scattering results indicate that the absorption cross sections of cadmium and samarium at resonance are higher than the values previously accepted. This has been confirmed by total cross section measurements on cadmium for which the Breit-Wigner parameters are $E_0 = 0.180$ ($\pm .003$) ev., $\Gamma = 0.113$ ev., $\sigma_{a0} = 7750$ barns, $\sigma_P = 4.7$ barns, $a_R = 7 \times 10^{-13}$ cm. The spin of the compound nucleus is unity. For Sm^{149} the spin of the compound nucleus (0.096 ev. resonance) is $i + \frac{1}{2}$. The scattering cross section of europium for neutrons of energy 0.03 ev. to 0.15 ev. is 8 barns, almost independent of the energy. The scattering cross section of dysprosium is 100 barns at 0.03 ev. and decreases slowly with increasing energy, thus confirming the existence of a level at negative neutron energy. The spin of the compound nucleus for the 1.26 ev. resonance in Rh^{103} is found to be unity and that for the 1.45 ev. resonance in In^{115} is found to be four.

INTRODUCTION

Scattering and absorption of neutrons with energies near a resonance energy are described in terms of the single level Breit-Wigner dispersion formulas (10). These expressions have been compared with experiment individually on different resonances (1, 27) but at the time this work was begun they had not been checked simultaneously and in detail on the same resonance. In this paper measurements of the total cross section and the ratio of scattering cross section to absorption cross section for the low energy cadmium resonance are presented which are in excellent agreement with the Breit-Wigner theory. Less detailed examination of several other resonances confirms this agreement.

Preliminary accounts by Brockhouse, Hurst, and Bloom (7, 5) of part of this work have already appeared. Since these publications the apparatus and the method of treatment of the results have been improved and the measurements on cadmium, samarium, and gadolinium described in (7) and (5) have been repeated using the new arrangements.

Tittman and Sheer (31) at Columbia University have measured the ratio of the scattering and total cross sections for the 4.87 ev. resonance in gold. Their measurements extended over a wider range of energy than was used in this work. They obtained good agreement with the Breit-Wigner formulas but, because of inadequate resolution, they were unable to measure the total cross sections in detail over the same resonance and had to rely on the self-indication cross section and resonance integrals, with which their measurements agreed well.

[1] *Manuscript received December 8, 1952.*

Contribution from Physics Division, Chalk River Laboratories, Atomic Energy of Canada Ltd., Chalk River, Ontario, Canada. Issued as A.E.C.L. No. 36. This paper was presented at the Quebec meeting of the Royal Society of Canada, June, 1952.

The results of Brockhouse, Hurst, and Bloom and of Tittman and Sheer must be corrected for the change of neutron energy on scattering. The former authors gave no detailed resonance parameters but some of the parameters given by Tittman and Sheer are in error, probably by about 10%. The necessary correction is discussed below.

The resonances investigated in this work are the low lying resonances which determine the properties of the nucleus for thermal neutrons. The detailed resonance parameters are therefore of some interest in themselves; in particular, the spin of the compound nucleus is the spin of the capture state for thermal neutrons, of interest in such experiments as those of Kinsey and Bartholomew (16) on capture γ-ray spectra.

EXPERIMENT

Apparatus

The apparatus shown in Fig. 1 was mounted on the arm of the spectrometer previously described (13). Monochromatic neutrons, reflected from the 200 plane of a sodium chloride crystal, entered the scattering chamber through a

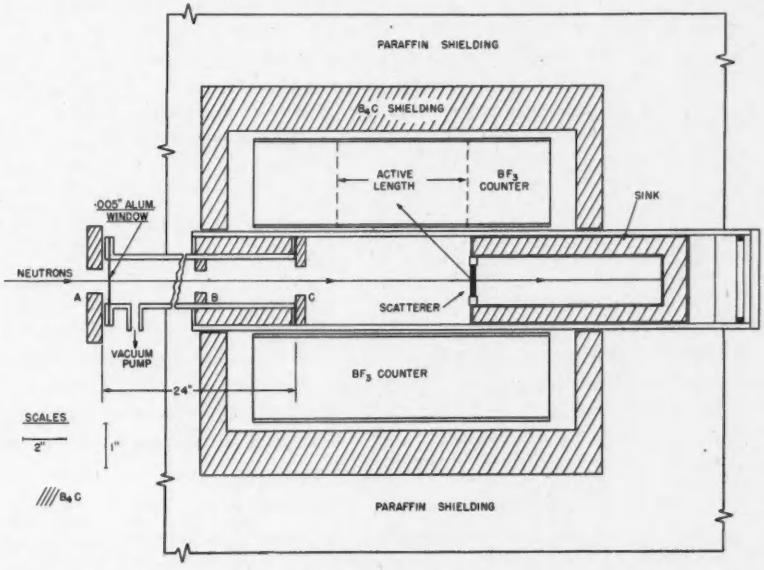

FIG. 1. Apparatus. The horizontal dimensions are compressed relative to the vertical in the ratio 2: 1.

collimating system. Neutrons scattered backwards from the specimen were detected in an annular bank of six BF_3 (enriched in B^{10}) counters which surrounded the scattering chamber. Neutrons which were not scattered were captured in a boron carbide sink. To reduce background the scattering chamber

and collimator were evacuated and the apparatus was shielded with thick layers of boron carbide and paraffin.

The counting rate with a specimen was compared with that from a vanadium standard scatterer. The background counting rate was taken with an empty sample holder in position and subtracted from the counting rates of the specimen and the standard. The background was principally due to neutrons leaking through the shield and to counter contamination and was independent of whether or not a sample was in position. A thin BF_3 counter monitored the neutron beam and all counting rates were normalized to a common beam intensity.

Collimator and Sink

The incoming neutron beam, which had an angular divergence of about 12 min. of arc in the horizontal direction and 45 min. in the vertical direction, was stopped down to $\frac{1}{2}$ in. diameter by an aperture in a boron carbide (B_4C) plate (A). The beam passed through a second $\frac{1}{2}$-in. aperture (B) at a distance of 19 in. from the first. Neutrons scattered by the boron carbide were prevented from reaching the counters by a third boron carbide stop (C) with an aperture $\frac{5}{8}$ in. in diameter, through which the $\frac{1}{2}$ in. beam passed without interference.

At the specimen position the fraction of the beam lying outside a $\frac{3}{4}$ in. diameter circle was less than 1/30,000. Hence the aluminum sample holders which were $\frac{3}{4}$ in. inside diameter contributed little to the background.

The neutron beam was caught in a sink of boron carbide contained in a thin (~ 0.010 in.) aluminum can. The sink was designed so that no singly scattered and few multiply scattered neutrons could reach the counter.

As a result of these precautions the background from the beam was nearly unmeasurable, being about one per hundred thousand countable neutrons in the thermal region.

The boron carbide parts were molded from boron carbide powder using a small amount of sodium silicate as binder. A mixture of boron carbide and just enough sodium silicate (diluted 50%) to wet it was kneaded into an aluminum mold and then compressed by an arbor press or hammering. The mold was then heated slowly to 300° C. and held there for several hours. Parts made in this way have fair mechanical strength and good shielding properties and can be made in comparatively complex forms.

Theory of the Experiment

In this experiment the scattering by a specimen of unknown scattering cross section (σ_s) but known total cross section (σ_T), for which $\sigma_s \ll \sigma_a \simeq \sigma_T$, was compared with that by a standard specimen of vanadium which was almost "thin". It was impracticable to use a "thin" specimen of the unknown scatterer and hence it was necessary to take self-absorption into account. For the standard vanadium scatterer self-absorption and multiple scattering produced small effects which were calculated.

Because of the cylindrical symmetry of the apparatus and scatterers it was possible to compute the scattering for a highly absorbing sample under the

condition that $\sigma_s \ll \sigma_a$. The approximation used is believed to take good account of self-absorption and to take partial account of multiple scattering. It is shown in the appendix that, for $\sigma_s \ll \sigma_a$, the counting rate from the absorbing sample is

$$[1] \qquad N = C_0 \frac{\sigma_s}{\sigma_a}\left\{1 - C_1 \frac{\sigma_s}{\sigma_a}\right\} \Big/ H(T)\left\{1 + C_2 \frac{\sigma_a' - \sigma_a}{\sigma_a}\right\}$$

where C_0, C_1, and C_2 are constants which were computed from the geometry of the apparatus and the angular variation of the counter sensitivity, T is the transmission of the specimen, and $H(T)$ is a function which is very slowly varying for $T < 0.5$ and which is also computed from the geometry. In taking account of self-absorption in the specimen consideration is given to the fact that the energy of the neutron after scattering is, in general, not the same as before scattering and hence that the absorption cross section (σ_a') for the neutron leaving the specimen after scattering is not equal to the absorption cross section (σ_a) for the neutrons entering the specimen. In the formula the quantity $(\sigma_a' - \sigma_a)/\sigma_a$ is averaged over the energy distribution of the neutrons after scattering, taking account of the energy dependence of the counter sensitivity.

In an approximation which takes explicit account of multiple scattering, the counting rate from the standard scatterer is shown to be

$$[2] \qquad N_v = C_v \sigma_{sv} G(E)$$

where σ_{sv} is the scattering cross section of vanadium, and C_v is another constant computed from the geometry of the apparatus. $G(E)$ is a slowly varying function, computed from the geometry of the apparatus, which takes account of self-absorption in the vanadium scatterer and has the value unity when the absorption is zero. Combining Equations [1] and [2], the ratio of the scattering and absorption cross sections of the absorbing sample is

$$[3] \qquad \frac{\sigma_s}{\sigma_a} = C \sigma_{sv} \frac{N}{N_v} H(T)\, G(E)\left\{1 + C_1 \frac{\sigma_s}{\sigma_a}\right\}\left\{1 + C_2 \frac{\sigma_a' - \sigma_a}{\sigma_a}\right\}.$$

Equation [3] shows that, in addition to measuring the ratio N/N_v and the transmission of the sample, it is necessary to know the absorption cross section as a function of energy and the distribution-in-energy of the neutrons after scattering, in order to obtain σ_s/σ_a.

Calibration of the Apparatus

Cross Sections of Vanadium

To determine the cross sections of vanadium the total cross section of the standard scatterer (which contained 1.784×10^{22} atoms/cm.^{2}) was measured as a function of the neutron energy from 0.02 to 5 ev. and is shown in Fig. 2. A least squares fit to the measurements gave

$$\sigma_{Tv} = 5.07 + 5.29\sqrt{\frac{0.025}{E}} \text{ barns.}$$

The constant term was assumed to be the scattering cross section (σ_{sv}), and the term proportional to $E^{-\frac{1}{2}}$ the absorption cross section (σ_{av}). Scattering

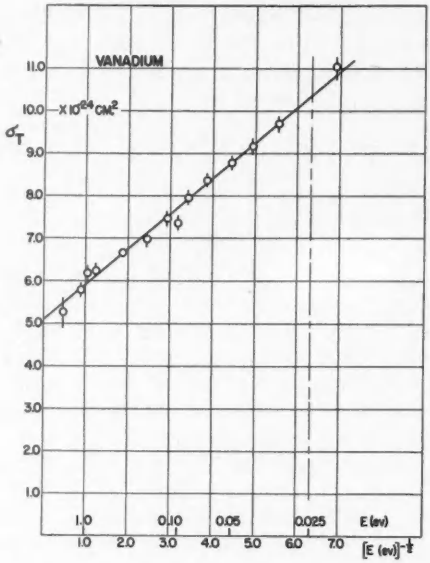

FIG. 2. Total cross section of vanadium plotted as a function of the inverse square root of the energy. The intercept on the ordinate axis gives the value of the free scattering cross section.

cross sections of 5.0 (12) and 4.7 (8) barns have been previously reported without accuracy assignments. The uncertainty in the value 5.07 barns is about ± 0.15 barns.

The absorption cross section of 5.29 barns is somewhat higher than the value of 4.7 barns obtained by Pomerance (26) from pile oscillator measurements, the difference being outside the probable errors in the two measurements. The vanadium used in the standard scatterer was supplied by the Vanadium Corp. of America and had a nominal purity of 99.7%, the stated impurities being innocuous from the point of view of neutron cross sections. The material was examined spectrographically for boron and found to contain about 10 p.p.m., insufficient to affect the results.

In the calculations for this experiment the cross sections $\sigma_{sv} = 5.07$ and $\sigma_{av} = 5.29$ barns were used. Since the absorption cross section affects only the function $G(E)$, small errors in σ_{av} do not affect the results appreciably. The cross section ratio is, however, directly proportional to σ_{sv} and hence the uncertainty in σ_{sv} is reflected in the ratio σ_s/σ_a.

Counter Sensitivity Function

By shielding the counters from the vanadium scatterer with a set of cadmium rings which were removed one at a time, the counter sensitivity was determined experimentally as a function of angle. It was necessary to correct the measurements for the fact that normally some neutrons were scattered

by the walls of the counters and scattering chamber before being counted, and part of these were absorbed by the cadmium rings. The correction produced about 7% change in the angular distribution. The constants are however relatively insensitive to the detailed form of the counter sensitivity function, and this correction produced only about 1% change in the final result. The counter sensitivity $q(\theta)$ was found by dividing the corrected experimental angular distribution by the scattering $I_v(\theta)$ expected from the vanadium scatterer. Neutrons of two different energies (0.05 and 0.11 ev.) were used and the counter sensitivity functions obtained for the two energies were in agreement within the experimental error. The function $q(\theta)$ is shown in Fig. 3. It is approximately what would be predicted from the geometry of the apparatus.

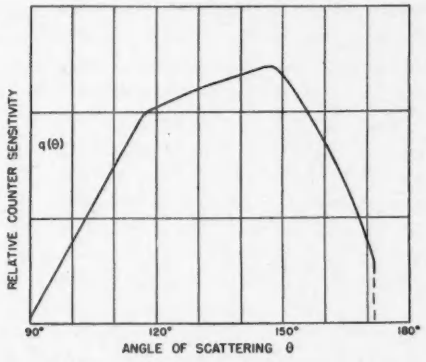

FIG. 3. The relative counter sensitivity per unit solid angle $q(\theta)$ as a function of the angle of scattering θ.

Accuracy of Calibration

The over-all accuracy of the calibration is estimated to be 5%, of which about half is due to the vanadium cross section. The remainder arises from errors in the angular sensitivity function and from the approximations used in obtaining the constants in Equation [3]. A further error, which varies from one specimen to another but is never large, is introduced by the correction for the change of neutron energy on scattering and by the effects of binding on the scattering by the standard and the specimen.

TREATMENT OF RESULTS

Correction for Background and Variations in Incident Flux

Measured counting rates included a contribution from background. This background had two components, one proportional to the reactor flux and one independent of reactor operation. Counting was carried out for a convenient time (t_R) with the appropriate specimen, and the number of signal counts N_{RO} and monitor counts N_{RM} registered. Similar data were taken with the standard scatterer (t_S, N_{SO}, N_{SM}) and with an empty cassette for back-

ground (t_B, N_{BO}, N_{BM}). The reactor independent background was measured with the reactor off. The signal and monitor counts were each corrected for reactor independent background and the signal counts normalized to unit monitor count. The ratio N/N_v, corrected for background and for variations in incident flux, is then

$$[4] \quad \left(\frac{N}{N_v}\right)_0 = \left\{\frac{N_{RO} - xt_R}{N_{RM} - Xt_R} - \frac{N_{BO} - xt_B}{N_{BM} - Xt_B}\right\} \Big/ \left\{\frac{N_{SO} - xt_S}{N_{SM} - Xt_S} - \frac{N_{BO} - xt_B}{N_{BM} - Xt_B}\right\}$$

where x is the reactor independent background counting rate in the signal counter and X in the monitor counter.

Correction for Contamination in the Beam

In addition to neutrons of the desired energy the beam diffracted by a crystal from the continuous reactor spectrum contains neutrons of 2nd and higher orders which satisfy the Bragg condition, i.e. neutrons of four times, nine times, etc., the desired energy. For primary energies of 0.05 to 0.125 ev. this order contamination was negligible. Below 0.05 ev. the second order content increased rapidly and below 0.02 ev. it became overwhelming. In this region the second order content (γ) was determined by boron absorption as described by Sturm (30). From 0.150 to 0.40 ev. the order content (γ) was determined by removing the first order neutrons with cadmium and extrapolating the residual transmission for various thicknesses of cadmium back to zero thickness. Above 0.40 ev. the order content was estimated from the residual transmission of samples of various elements at their resonance energies.

The neutron beam was also contaminated with neutrons diffusely scattered from the crystal. These had predominantly energies in the thermal region with a mean at about 0.07 ev. The content (δ) of diffusely scattered neutrons was determined by turning the monochromating crystal slightly out of the Bragg position. The ratio $(N/N_v)_0$ was corrected for contamination by means of the equation

$$[5] \quad \frac{N}{N_v} = \frac{(N/N_v)_0 - \gamma(N/N_v)_2 - \delta(N/N_v)_T}{1 - \gamma - \delta}$$

where $(N/N_v)_2$ is the value of the ratio at the second order energy and $(N/N_v)_T$ is its value at the mean energy of the diffusely scattered neutrons. The quantities γ and δ in Equation [5] include effects of the energy dependence of the counter sensitivity and of the scattering power of the standard scatterer, and hence were determined in the scattering apparatus using the vanadium scatterer and the annular counters as the detector. In order to keep the correction for contamination small, the specimens were made as thin as was consistent with a small correction for sample transmission.

Correction for Change of Neutron Energy on Scattering and for Crystal Effects

To apply formula [3] it is necessary to determine the distribution of neutron energies after scattering by the polycrystalline samples and standard. This question has been investigated experimentally and compared with the theory for Einstein crystals by Brockhouse and Hurst (6). The formula for the

Einstein crystal (Reference (6), Equation (3)) was found to be in agreement with experiment under conditions applicable in this work and was used to obtain the energy distributions over which the averages in Equation [3] were carried out.

The procedure is illustrated by Fig. 4 in which the energy distributions computed for cadmium (Einstein temperature 129° K.) for incident neutron energies of 0.100 ev., 0.175 ev., and 0.275 ev. are shown. The absorption cross section of cadmium is also shown. This is the cross section seen by the neutron when entering the specimen. The cross section which is effective for the neutron leaving the specimen is the average of the absorption cross section over the energy distribution, shown as a dashed line.

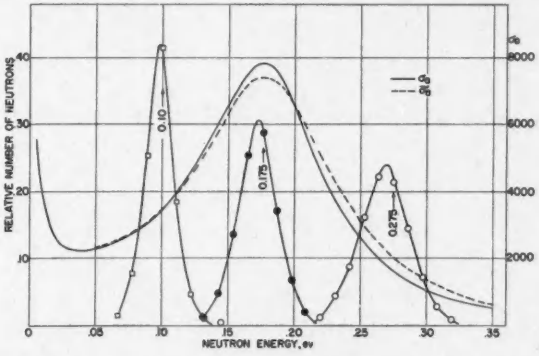

FIG. 4. The energy distributions of neutrons of initial energy 0.10, 0.175, and 0.275 ev. after scattering by cadmium through an angle of 135°, computed according to an Einstein crystal model. The thick solid line shows the absorption cross section of cadmium as a function of energy. The dashed line shows the effective absorption for the scattered neutrons.

Because both the mean loss of energy and the width of the distribution increase with neutron energy, the correction becomes difficult to handle at high neutron energies and this may set an upper limit on the neutron energy at which this method of measuring scattering cross sections can be used.

Under the conditions holding in this experiment, the differential scattering cross section for the Einstein crystal is nearly equal to that of the free atom. Since the mean angle of scattering in this experiment was 130°–135° the measured differential cross section was somewhat lower (31) than $1/4\pi$ times the free cross section. This reduction, however, was almost exactly compensated by the increase of the counter sensitivity due to the decrease in mean neutron energy so that no corrections were made. The counters had very nearly a $1/v$ dependence on the neutron energy.

Vanadium was chosen as a standard scatterer because it gives virtually no coherent scattering and hence shows no crystal effects. Crystal effects were also of little importance in the specimen scatterers because of the comparatively high temperature, large angle of scattering, and large solid angle. The first two result in reduction of the size of the Bragg peaks through the Debye

Waller temperature factor. The large solid angle includes many Debye-Scherrer rings, the resultant average scattering approaching that from a single bound atom.

Corrections for Resolution and Doppler Effect

The quantity measured in these experiments is the ratio of the scattering and absorption cross sections individually averaged over the Doppler motion, the ratio being itself averaged over the instrument resolution. Though σ_s and σ_a are rapidly changing functions of the energy in the neighborhood of a resonance, they behave in much the same way and their ratio is not nearly as energy dependent as the quantities themselves. Hence Doppler effect and resolution of the apparatus were taken into account only for resonances well above the thermal region.

BREIT-WIGNER FORMULAS

The absorption and scattering cross sections for neutrons having energies near a resonance energy are given by the single level Breit-Wigner dispersion formulas (10)

$$[6] \qquad \sigma_a = g f\,(\pi/kk_0)\;\Gamma_a\,\Gamma_{n0}\,[(E-E_0)^2+\Gamma^2/4]^{-1},$$

$$[7] \qquad \sigma_s = \sigma_P + \pi g f\,[\Gamma_{n0}{}^2/k_0{}^2 + 4\Gamma_{n0}(E-E_0)\,a_R/k_0]\,[(E-E_0)^2+\Gamma^2/4]^{-1}.$$

In these formulas E is the neutron energy and $k = \sqrt{2ME}/\hbar$ is the neutron wave number, Γ_a is the γ-ray or absorption width, $\Gamma_n = \Gamma_{n0}(k/k_0)$ is the neutron width, $\Gamma = \Gamma_n + \Gamma_a$ is the total width, f is the isotope abundance, i is the nuclear spin, a_R is the potential scattering length of the resonant spin state of the resonant isotope, and σ_P is the so-called potential scattering cross section and includes the scattering due to the nonresonant isotopes, the nonresonant spin state of the resonant isotope, and the potential scattering by the resonant spin state of the resonant isotope. The subscript 0 on any quantity indicates its value at resonance. The spin weight factor g has two possible values

$$[8] \qquad g = \frac{1}{2}\left\{1 \pm \frac{1}{2i+1}\right\}$$

corresponding to

$$[9] \qquad I = i \pm \tfrac{1}{2}$$

for the spin of the compound nucleus.

The ratio σ_s/σ_a is

$$[10] \qquad \sigma_s/\sigma_a = (k/k_0)\;(\Gamma_{n0}/\Gamma_a) + 4(E-E_0)k\,a_R/\Gamma_a + \sigma_P/\sigma_a\,.$$

The first term of this expression is due to the purely resonant scattering, the last term to the potential scattering, and the middle term arises from interference between the potential and resonant scattering and is zero at resonance.

If $\sigma_s/\sigma_a \ll 1$, as was the case in the present work, then

$$[11] \qquad \Gamma_{n0}/\Gamma_a = k_0{}^2\,\sigma_{a0}/(4\pi g f - 2\sigma_{a0}\,k_0{}^2)\,.$$

Where the isotopic assignment of the resonance has been made and the total cross section has been determined, the only parameters available to fit the

scattering measurements are σ_P, a_R, and g, which can therefore be determined unambiguously in most cases.

The corrected scattering measurements and the theoretical formulas apply to free nuclei at rest while measured total cross sections apply to nuclei having the motion of atoms in the appropriate solid at room temperature. Parameters obtained from total cross section data must be corrected for Doppler effect before being used in the above equations. This was done using the methods of Lamb (18). In some cases a set of curves given by Wallace (33) was used.

RESULTS AND DISCUSSION

Measurements of σ_s/σ_a over a range of energies in the low energy region have been made on specimens of cadmium, samarium oxide, gadolinium oxide, europium oxide, and dysprosium oxide. In addition measurements have been made on isolated resonances in indium and rhodium.

Cadmium

A series of foils of different thicknesses were rolled from Johnson Matthey "specpure" cadmium metal. The foil having its transmission nearest 0.15 at the energy in question was used for the measurements. This thickness was

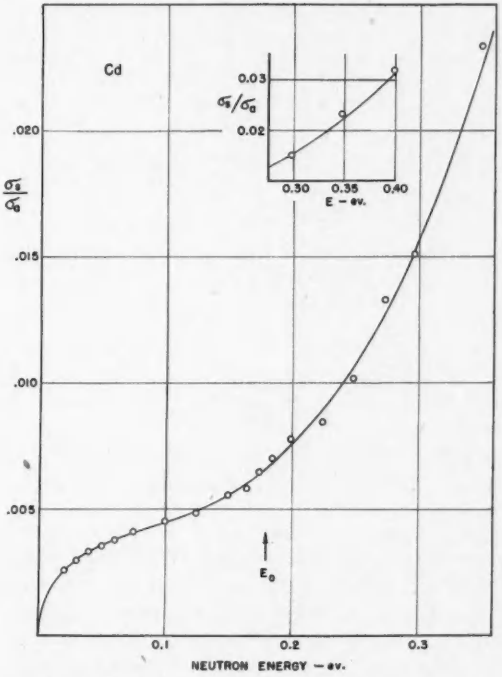

FIG. 5. The ratio σ_s/σ_a for cadmium as a function of neutron energy. The solid line shows the best fitting Breit-Wigner curve, calculated with $E_0 = 0.180$ ev., $\Gamma_a = 0.113$ ev., $\Gamma_{n0}/\Gamma_a = 0.00603$, $\sigma_P = 4.7$ barns, $a_R = 7 \times 10^{-13}$ cm., $I = 1$.

about optimum from the point of view of the corrections for specimen transmission and beam contamination.

The measured values of the ratio σ_s/σ_a for cadmium, all corrections made, are shown in Fig. 5 as circles. An attempt was made to fit the measurements to a Breit-Wigner formula using the parameters of Rainwater *et al.* (27) obtained from total cross section measurements. It was not possible to obtain a fit within what was believed to be the accuracy of the measurements. The total cross section at resonance given by Rainwater *et al.* was 7200 barns. Early work at this laboratory (32) had indicated that the cross section was about 10% higher than this value and suggested the desirability of remeasuring the total cross section.

The transmission of the cadmium foils was measured at an energy of 0.175 ev., close to the resonance energy. The results are shown in Fig. 6, plotted on a

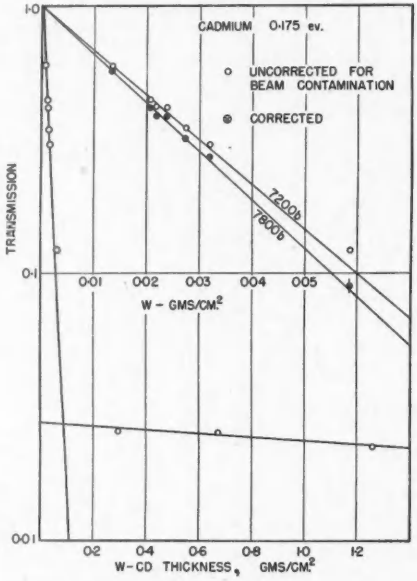

FIG. 6. Transmission of cadmium foils at 0.175 ev. plotted against cadmium thickness (lower scale). Presence of 2nd order component in beam is indicated. The same points are plotted on a more extended scale of cadmium thicknesses (upper scale) to show the effect of correction for the 2nd order contamination.

logarithmic scale as a function of the foil thickness in gm./cm.^{2} The transmissions fall along two well-defined straight lines corresponding to the primary neutron energy of 0.175 ev. and the higher order components in the beam. The transmissions of the thinner foils are also shown plotted on a more extended scale of thickness together with the values obtained after correction for contamination in the beam. The corrected values correspond to a total

cross section of 7800 barns at 0.175 ev. Another, independent, set of measurements gave the same value.

Similar though less extensive measurements were made at five energies below 0.175 ev. Above this energy the correction for contamination became large and difficult to handle but at 0.30 and 0.35 ev. the second order component was eliminated by rhodium and indium filters. Extensive sets of measurements were made at these two energies. After a small (~1% estimated) correction for instrument resolution was applied and the small scattering cross section was subtracted, the measurements were fitted to a Breit-Wigner formula with the result

$$[12] \qquad \sigma_a = 24.7_5\sqrt{0.180/E}\,[(E-0.180)^2+0.00319]^{-1}\times 10^{-24}\text{cm}^2$$

corresponding to $E_0 = 0.180 \pm .003$ ev.,
$\sigma_{a0} = 7750 \pm 150 \times 10^{-24}$ cm.^{2},
$\Gamma = 0.113 \pm .002$ ev.

The abundance of the resonant isotope Cd^{113} is 0.1230 and its spin is 1/2 (25). Beeman (2) found that $g = 0.75$ corresponding to spin 1 for the compound nucleus. This is in agreement with the present work. After correcting σ_{a0} for Doppler effect Γ_{n0}/Γ_a is found from Equation [11] to be 0.0060. Using these values for the parameters the measurements of Fig. 5 were fitted to Equation [10]. The best fitting expression of this form is shown (Fig. 5) and corresponds to

$$a_R = 7.0 \pm 1.0 \times 10^{-13} \text{ cm.},$$
$$\sigma_P = 4.7 \pm 0.5 \text{ barns.}$$

The value of a_R is close to the geometrical radius of cadmium (6.8×10^{-13} cm.) taken to be $1.42 \times 10^{-13}A^{\frac{1}{3}}$ cm., where A is the atomic weight. The potential scattering cross section agrees satisfactorily with the value 5.2 ± 0.7 barns found by Rainwater *et al.* on the high energy wing of the resonance.

The theoretical expressions for σ_a and σ_s (Equations [6], [7]) are compared with the values obtained from the measurements of σ_s/σ_a and σ_T in Fig. 7.

Rare Earths

Measurements were made on specimens of the sesquioxides of samarium, gadolinium, dysprosium, and europium (Johnson Matthey "specpure"). The oxides were heated in air for two hours at 800° C. to remove water and carbon dioxide. They were then transferred in a dry box to small aluminum sample holders. The specimens and holders were then heated in vacuum at 350° C. for several hours.

The oxides were contained between 0.002 in. aluminum foils. Since only the front foil contributed to the scattering, background measurements were made using a holder with one foil.

In computing the energy distribution the Einstein temperature was assumed to be 0.025 ev., i.e. equal to room temperature. This is consistent with the very scanty specific heat data in the literature (15), and fortunately the energy distribution is not very sensitive to the Einstein temperature. The contri-

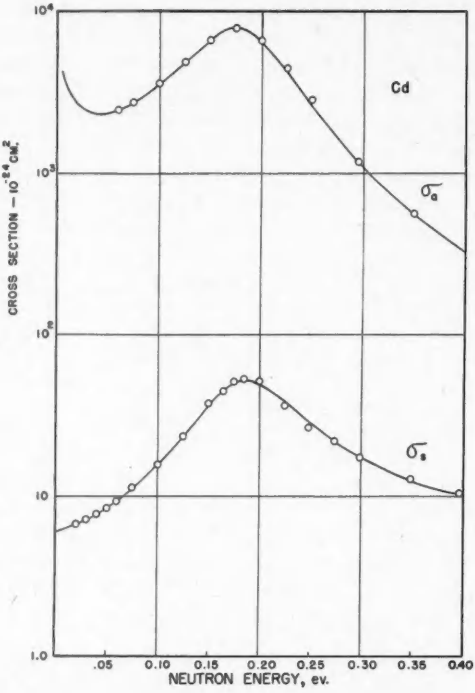

FIG. 7. Absorption and scattering cross sections of cadmium compared with theoretical curves. Values of σ_a shown for 0.225 and 0.25 ev. have little weight because of large corrections for contamination and low statistics.

butions of the rare earth and oxygen ions to the energy distribution were computed separately and weighted according to their cross sections.

Samarium

The scattering ratio σ_s/σ_a was measured for neutron energies of 0.025 to 0.16 ev. and is shown in Fig. 8, with all corrections made. The resonance at 0.096 ev. belongs to Sm^{149} (19) which has an abundance of 0.1368 (the weighted mean of the two most recent determinations (14, 21)). The spin of Sm^{149} has been variously reported as 5/2 (24) and 7/2 (3). Experimental (3) and theoretical (9) considerations support the value 7/2 which is also in better agreement with this experiment.

The total cross section has been measured by Sturm (30) who found σ_{a0} = 15,500 barns and Γ = 0.074 ev. Using these values it has not been possible to obtain a fit within the precision of the measurements, though the spin of the compound nucleus is clearly $i + \frac{1}{2}$. To obtain a fit σ_{a0} must be increased and this is in agreement with recent work of Sailor (28) who has observed a total cross section of 16,800 $\pm$ 200 barns at 0.094 ev. Assuming this value for σ_{a0}

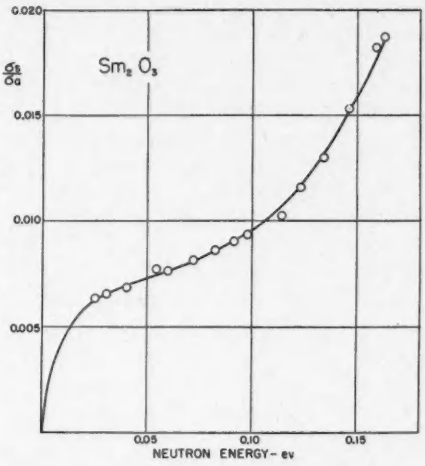

FIG. 8. Ratio of scattering to absorption cross sections for samarium oxide. The solid line is the best fitting Breit-Wigner curve, calculated with $E_0 = 0.096$ ev., $i = 7/2$, $I = 4$, $\Gamma_a = 0.074$ ev., $\Gamma_{n0}/\Gamma_a = 0.00816$, $\sigma_P(1/2(Sm_2O_3)) = 19$ barns, $a_R = 5.0 \times 10^{-13}$ cm.

at room temperature and correcting for Doppler effect $\Gamma_{n0}/\Gamma_a = 0.00816$. If Γ_a is assumed to be 0.074 ev. in agreement with Sturm and i is taken to be 7/2, a good fit can be obtained with $\sigma_P = 19$ barns and $a_R = 5 \times 10^{-13}$ cm. Subtracting 5.6 barns for the oxygen contribution ($3/2\ \sigma_s$ for oxygen) σ_p for samarium is 13.4 barns, somewhat higher than the geometrical cross section of about 8 barns, while a_R is somewhat lower than the geometrical radius. A change in E_0 or Γ_a could change these values appreciably however.

Gadolinium

Gadolinium has a very large slow neutron cross section which shows resonance behavior. According to Lapp, Van Horn, and Dempster (19) two isotopes contribute to the average cross section over a reactor neutron spectrum, Gd^{157} contributing about 78% and Gd^{155} 22%. The spin of neither isotope is known.

Measurements of σ_s/σ_a for gadolinium oxide for energies from 0.02 to 0.16 ev., with all corrections made, are shown in Fig. 9. Combining these results with the total cross section data of Sturm (30) the scattering and absorption cross sections of Fig. 10 are obtained. Sturm, and Brill and Lichtenberger (4) were able to fit their total cross section measurements by the single level Breit-Wigner formula with a resonance energy of about 0.03 ev. The scattering cross section also shows resonance behavior at about this energy but does not obey a single level formula. The values expected for the scattering cross section at resonance, computed from Sturm's data for various spins of target and compound nuclei on the assumption that the resonance is in Gd^{157}, are also shown. The disagreement with the measured scattering cross section is about as expected from the results of Lapp, Van Horn, and Dempster.

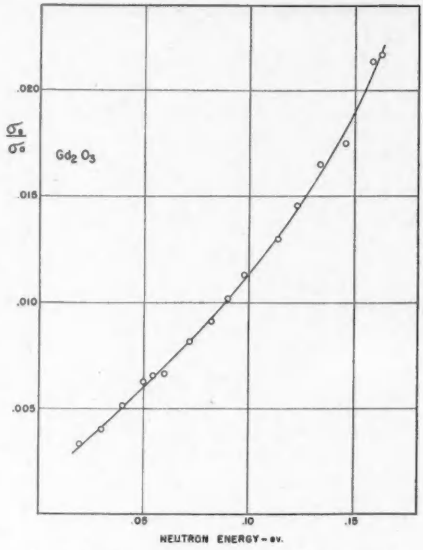

FIG. 9. The ratio σ_s/σ_a for gadolinium oxide.

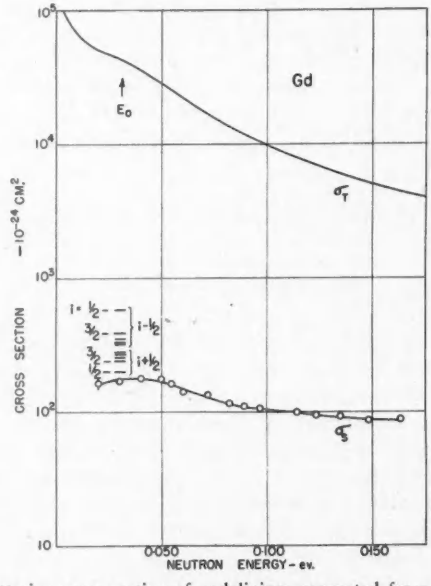

FIG. 10. The scattering cross section of gadolinium computed from σ_s/σ_a and the total cross section of Sturm (30). The bars at 0.03 ev. show the expected scattering cross section at this energy (assuming Sturm's resonance parameters and assigning the resonance to Gd^{157}) for various spins of the target and compound nucleus.

Dysprosium

Measurements of the total cross section of dysprosium by Sturm (30) suggested that the $1/v$ law is not obeyed and indicated a large resonance at a negative neutron energy of about 1 ev. Measurements of σ_s/σ_a for dysprosium oxide are shown in Fig. 11. The ratio is seen to be large ranging from 0.1 to 0.2. Hence the theory of the experiment does not apply accurately and the results may be a few per cent in error. When these results are combined with Sturm's total cross section and the oxygen contribution is subtracted, a scattering cross section of 100 barns at 0.03 ev. is obtained, which decreases almost linearly to 72 barns at 0.10 ev. It should be remarked, however, that a rough set of measurements made on the dysprosium sample indicate that

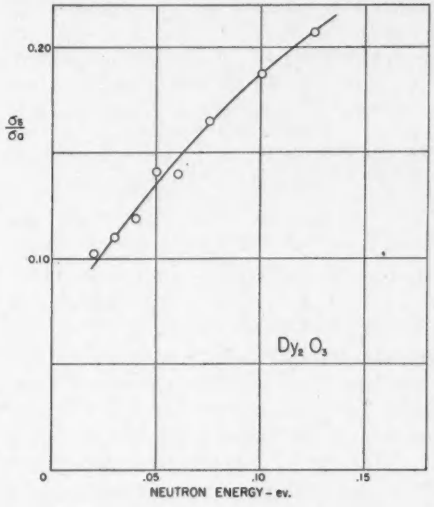

FIG. 11. The ratio σ_s/σ_a for dysprosium oxide.

while the total cross section in the region of 0.03 ev. is the same as that given by Sturm the cross section at higher energies has very nearly a $1/v$ energy dependence. Use of this total cross section gives a scattering cross section of 100 barns at 0.03 ev. decreasing to 90 barns at 0.10 ev. A large resonance at negative energy is again indicated but with the resonance energy considerably higher than 1 ev. (negative).

Europium

Results for europium are shown in Fig. 12. Combining these measurements with the total cross section data of Sturm (30) and subtracting 5.6 barns for the oxygen contribution, the scattering cross section of europium is found to be 8 ± 1 barns, almost independent of the neutron energy in the range 0.03 to 0.15 ev.

This again is, qualitatively, as expected from the total cross section which shows the presence of a resonance at -0.011 ev. in Eu^{151} and at 0.465 ev. in

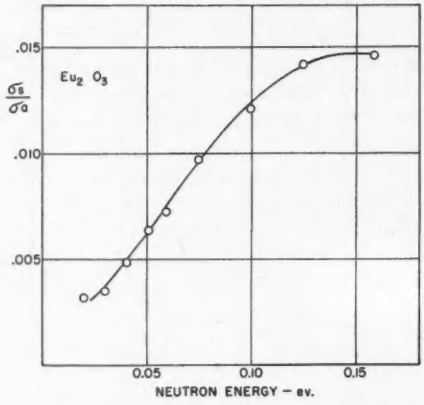

FIG. 12. The ratio σ_s/σ_a for europium oxide.

Eu^{153}. The first increases the scattering by Eu^{151} slightly above the potential scattering and the second lowers the scattering by Eu^{153} slightly below the potential scattering.

Rhodium and Indium

Measurements were made on rhodium and indium foils in the vicinity of their resonance energies at 1.26 ev. and 1.45 ev. respectively. Because of low counting rates it was not possible to determine σ_s/σ_a over the entire resonance and hence measurements were made only in the immediate vicinity of the resonance energies. In these cases the analysis was complicated by the necessity of taking into account the instrument resolution. In analyzing the measurements resonance parameters due to Sailor (28, 29) were employed. For indium the cross section at resonance is about 27,000 barns and the total width is 0.11 ev. For rhodium the cross section at resonance is 4630 barns and the width is 0.176 ev. The cross section of indium is in agreement with the work of McDaniel (22). The cross section of rhodium is much higher than that given by Meijer (23) but is in better agreement with measurements by Lowry and Goldhaber (20). The parameters apply to the metal at room temperature and had to be corrected for Doppler effect following Lamb (18).

Rhodium

The 1.26 ev. level in Rh^{103} is comparatively weak and hence potential scattering is important even near resonance. The scattering cross section for neutrons of 0.15 ev. energy was measured and found to be 4.1 barns. The potential cross section σ_P was then computed from Equation [7] assuming $a_R = 7 \times 10^{-13}$ cm., the geometrical radius of rhodium, and was found to be 5.3 barns.

The result of the scattering measurements was $\Gamma_{n0}/\Gamma_a = 0.004 \pm 0.003$ where the limits represent the estimated over-all uncertainty. This result is considerably lower than the value of 0.043 found by Harris *et al.* (11) from

integral scattering and absorption measurements. The spin of Rh^{103} is 1/2 (17) and comparison with the total cross section of Sailor by means of Equation [11] shows that g is 3/4 and therefore the spin of the compound nucleus in unity. This result is consistent with the measurements of Lowry and Goldhaber (20) who found $g\Gamma_{n0}/\Gamma_a = 0.0029$.

It should be remarked that the counting rate in this experiment was extremely low, about 0.4 counts per minute, compared with a background of 8 counts per minute, which fluctuated by about the amount of the signal. Four separate runs were taken and the results were statistically definite but the possibility of error cannot be excluded.

Indium

The resonance at 1.45 ev. in In^{115} is so strong that potential scattering has no effect. Using the parameters of Sailor (28) and taking $i = 9/2$ (25), the scattering measurements showed that $\Gamma_{n0}/\Gamma_a = 0.043 \pm 0.006$ and that the spin of the compound nucleus is 4.

ACKNOWLEDGMENTS

I wish to thank Dr. D. G. Hurst for many helpful discussions, and Dr. H. Carmichael for a careful reading of the manuscript. I am also indebted to the Bureau of Mines, Ottawa, Canada, for casting the vanadium specimen, and to Dr. V. L. Sailor for permission to publish his total cross section results.

APPENDIX A

Scattering from an Absorbing Specimen

A beam of neutrons is incident normally on an infinite plane scatterer of thickness d. Per unit area and incident neutron the number of neutrons scattered by an element dx at depth x is $n\sigma_s \exp(-n\sigma_T x)dx$. It is assumed that the scattering is isotropic and that only the absorption cross section is effective in reducing the scattered intensity on the way out of the material. If $q(\theta)$ is the angular sensitivity of the counters (cylindrically symmetric), the number of neutrons scattered from an element dx at an angle θ into an element of solid angle $\frac{1}{2}\sin\theta\, d\theta$ with energy E', and counted, is

$$\tfrac{1}{2} n\sigma_s q(\theta) \sin\theta \exp\{-nx(\sigma_T + \sigma_a(E')\sec\theta)\}(E')^{-\frac{1}{2}} F(E')\, dE'\, d\theta\, dx \Big/ \int_0^\infty F(E')\,(E')^{-\frac{1}{2}}\, dE'$$

where $F(E')$ is the energy distribution and the factor $(E')^{-\frac{1}{2}}$ is introduced to take account of the energy sensitivity of the counters, which were "thin" and hence obeyed the $1/v$ law.

Integrating over the sample thickness, the number of neutrons scattered at an angle θ with an energy E' and counted is

$$\tfrac{1}{2}[\sigma_s/(\sigma_T + \sigma_a' \sec\theta)][1 - \exp\{-nd(\sigma_T + \sigma_a' \sec\theta)\}] \times q(\theta) \sin\theta\, d\theta\, F(E')\,(E')^{-\frac{1}{2}}\, dE' \Big/ \int_0^\infty F(E')\,(E')^{-\frac{1}{2}}\, dE'.$$

If the energy distribution is assumed to be that at the mean scattering angle, the total number of neutrons counted is

$$\int_0^\infty \tfrac{1}{2}\, F(E')\ (E')^{-\frac{1}{2}} dE' \int_0^\pi \sigma_s(\sigma_T + \sigma_a'\sec\theta)^{-1}[1 - \exp\{-nd(\sigma_T + \sigma_a'\sec\theta)\}]$$

$$\times\, q(\theta)\, \sin\theta\, d\theta \Big/ \int_0^\infty F(E')\ (E')^{-\frac{1}{2}}\, dE'.$$

For $\sigma_s \ll \sigma_a$, $nd\sigma_T \gg 1$, and $\sigma_a' - \sigma_a \ll \sigma_a$, this can be written as Equation [1] where

$$C_0 = \tfrac{1}{2}\int_0^\pi q(\theta)\, \sin\theta\ (1 + \sec\theta)^{-1}\, d\theta,$$

$$C_1 = \frac{C_0^{-1}}{2}\int_0^\pi q(\theta)\, \sin\theta\ (1 + \sec\theta)^{-2}\, d\theta,$$

$$C_2 = \frac{C_0^{-1}}{2}\int_0^\infty \frac{\sigma_a'(E') - \sigma_a}{\sigma_a} F(E')\ (E')^{-\frac{1}{2}}\, dE'$$

$$\times \int_0^\pi q(\theta)\, \sin\theta\ (1 + \sec\theta)^{-2}\, d\theta \Big/ \int_0^\infty F(E')\ (E')^{-\frac{1}{2}}\, dE',$$

$$H(T) = \left[1 - \frac{C_0^{-1}}{2}\int_0^\pi (T)^{1+\sec\theta} q(\theta)\, \sin\theta\ (1 + \sec\theta)^{-1}\, d\theta\right]^{-1},$$

and $T = e^{-nd\sigma_T}$ is the transmission of the specimen.

APPENDIX B

Scattering from the Standard Scatterer

Assuming isotropic scattering, the fraction of incident neutrons scattered backwards into an angle θ from an element dx and emerging from the sample without further interference is

$$\tfrac{1}{2}\, n_v\, \sigma_{sv}\, dx\, \exp\{-n_v x\, \sigma_{Tv}(1 + \sec\theta)\}\, \sin\theta\, d\theta$$

where the change of neutron energy is neglected. Integrating this over the sample thickness yields

$$[B1]\quad I_1\, d\theta = \frac{1}{2}\frac{\sigma_{sv}}{\sigma_{Tv}}\frac{[1 - \exp\{-n_v d_v \sigma_{Tv}(1 + \sec\theta)\}]}{(1 + \sec\theta)}\sin\theta\, d\theta, \qquad \pi/2 < \theta < \pi.$$

If there were no scattering or absorption on the way out, the number emerging would be

$$[B2]\qquad I_0\, d\theta = \frac{1}{2}\frac{\sigma_{sv}}{\sigma_{Tv}}\Big\{1 - \exp(-n_v d_v \sigma_{Tv})\Big\}\sin\theta\, d\theta.$$

The difference between [B1] and [B2] represents the number interfered with on the way out, of which a fraction σ_s/σ_T is scattered.

For forward scattering $(0 < \theta < \pi/2)$

$$[B3]\quad I_1\, d\theta = \frac{1}{2}\frac{\sigma_{sv}}{\sigma_{Tv}}\frac{\exp(-n_v d_v \sigma_{Tv}\sec\theta) - \exp(-n_v d_v \sigma_{Tv})}{1 - \sec\theta}\sin\theta\, d\theta.$$

The total number rescattered is

$$U = \frac{\sigma_{sv}}{\sigma_{Tv}} \int_0^\pi (I_0 - I_1)\, d\theta.$$

Of these some get out, some are rescattered, and some absorbed. If the scatterer is thin, i.e. $n_v d_v \sigma_{Tv} \ll 1$, the neutron density will not vary greatly with depth. Assume that the angular distribution and proportion of the multiply scattered neutrons getting out is the same as for the total scattered neutrons. The total number scattered into an angle θ is then

$$I_v\, d\theta = (I_1 + \tfrac{1}{2}(I_v/I_0)\, U \sin\theta)\, d\theta.$$

Hence

[B4] $$I_v(\theta) = \frac{I_1(\theta)}{1 - \tfrac{1}{2}(U/I_0) \sin\theta}$$

The number of neutrons per unit area and unit incident neutron which are counted is

[B5] $$N_v = \int_0^\pi I_v(\theta)\, q(\theta)\, d\theta.$$

For the standard scatterer $\frac{1}{2}(U/I_0) \sin\theta \sim 0.1$ and $n_v d_v \sigma_{Tv} \simeq 0.1$–$0.2$, and hence $I_v(\theta)$ is nearly proportional to σ_{sv}. Equation [B5] can therefore be written in the form of [2] where

$$C_v = \frac{1}{\sigma_{sv}} \int_0^\pi I_{v0}(\theta)\, q(\theta)\, d\theta.$$

I_{v0} is determined at $E = \infty$ where $\sigma_{av} = 0$ and $\sigma_{sv} = \sigma_{Tv}$, and

$$G(E) = \frac{1}{\sigma_{sv}} \int_0^\pi I_v(\theta)\, q(\theta)\, d\theta \Big/ C_v.$$

This form is used in order to emphasize that the results are normalized to a particular value of vanadium scattering cross section and will be changed in proportion with it.

The constants C_0, C_1, C_2, and C_v and the functions $H(T)$ and $G(E)$ were evaluated by numerical integration.

The constant C_v was also computed in an approximation of the type used for the absorbing sample (Appendix A) and found to differ by less than 2% from that found in this approximation. The effect of the finite beam diameter and specimen size was investigated and found to be negligible.

REFERENCES

1. Adair, R. K., Bockelman, C. K., and Peterson, R. E. Phys. Rev. 76: 308. 1949.
2. Beeman, W. W. Phys. Rev. 72: 986. 1947.
3. Bogle, G. S. and Scovil, H. E. D. Proc. Phys. Soc. (London), A, 65: 368. 1952.
4. Brill, T. and Lichtenberger, H. V. Phys. Rev. 72: 585. 1947.
5. Brockhouse, B. N. and Hurst, D. G. Phys. Rev. 83: 841. 1951.
6. Brockhouse, B. N. and Hurst, D. G. Phys. Rev. 88: 542. 1952.
7. Brockhouse, B. N., Hurst, D. G., and Bloom, M. Phys. Rev. 83: 840. 1951.
8. Egelstaff, P. A. Nature, 168: 290. 1951.
9. Elliott, R. J. and Stevens, K. W. H. Proc. Phys. Soc. (London), A, 65: 368. 1952.
10. Feshbach, H., Peaslee, D. C., and Weisskopf, V. F. Phys. Rev. 71: 145. 1947.

11. HARRIS, S. P., MUEHLHOUSE, C. O., and THOMAS, G. E. Phys. Rev. 79: 11. 1950.
12. HIBDON, C. T., MUEHLHOUSE, C. O., RINGO, G. R., and ROBILLARD, T. R. Phys. Rev. 82: 560. 1951.
13. HURST, D. G., PRESSESKY, A. J., and TUNNICLIFFE, P. R. Rev. Sci. Instruments, 21: 705. 1950.
14. INGHRAM, M. G., HESS, D. C. Jr., and HAYDEN, R. J. Phys. Rev. 73: 180. 1948.
15. International Critical Tables.
16. KINSEY, B. B. and BARTHOLOMEW, G. A. Physica. To appear.
17. KUHN, H. and WOODGATE, G. K. Nature, 166: 906. 1950.
18. LAMB, W. E. Jr. Phys. Rev. 55: 190. 1939.
19. LAPP, R. E., VAN HORN, J. R., and DEMPSTER, A. J. Phys. Rev. 71: 745. 1947.
20. LOWRY, L. L. and GOLDHABER, M. Phys. Rev. 76: 189. 1949.
21. MATTAUCH, J. and SCHELD, H. Z. Naturforsch. A, 3: 105. 1948.
22. MCDANIEL, B. D. Phys. Rev. 70: 832. 1946.
23. MEIJER, R. Phys. Rev. 75: 772. 1949.
24. MURAKAWA, K. and ROSS, J. S. Phys. Rev. 82: 967. 1951.
25. Nuclear Data. Natl. Bur. Standards (U.S.) Circ. No. 499. 1950.
26. POMERANCE, H. Phys. Rev. 83: 641. 1951.
27. RAINWATER, L. J., HAVENS, W. W. Jr., WU, C. S., and DUNNING, J. R. Phys. Rev. 71: 65. 1947.
28. SAILOR, V. L. Brookhaven National Laboratory. Private communication. Curves are given in Neutron Cross Sections Report, AECU 2040.
29. SAILOR, V. L. and BORST, L. B. Phys. Rev. 87: 161. 1952.
30. STURM, W. J. Phys. Rev. 71: 757. 1947.
31. TITTMAN, J. and SHEER, C. Phys. Rev. 83: 746. 1951.
32. TUNNICLIFFE, P. R. and HURST, D. G. Unpublished.
33. WALLACE, P. R. Natl. Research Council (Canada) Rept. LT 15. 1947.

THE ABSORPTION SPECTRA OF FREE RADICALS FORMED IN AN ELECTRIC DISCHARGE*

By P. J. Dyne**

The study of the absorption spectra of free radicals formed in an electric discharge has, up to the present, not been systematic. This paper reports a search which has been made, using the technique for the spectra of some diatomic and polyatomic radicals. Absorption spectra of the radicals OH, SH, CS, CN, and NH_2 have been observed in discharges through H_2O, H_2S, CS_2, $(CN)_2$, and NH_3 respectively. Discharges through a number of organic compounds were studied in the hope of finding absorption spectra of such radicals as CH_2 and CH_3. However, no new spectra were observed.

Oldenberg (9) developed a technique for the observation of OH radicals in a discharge through H_2O. Lewis and White (8) used a similar technique to make the first reported observation of the spectrum of the SH radical in a discharge through H_2S. White (12) studied CN radicals formed in a discharge through $(CN)_2$. Laird, Andrews, and Barrow (7) observed free radicals of long life, e.g., CF_2 and CS in discharges through a fluorocarbon and CS_2.

In the present study a 5 kw. radiofrequency oscillator was used which had been used previously in studies of emission spectra (3). A glass discharge tube, 1.2 meters long and 18 cm. in diameter, was placed along the axis of the oscillator coil. Brass end plates were sealed on to the glass tube. These carried two concentric extension tubes 5 cm. in diameter in which a set of multiple reflecting mirrors of the type described by White (13) could be placed (Fig. 1). The separation of the mirrors was 2 meters. The reflecting surfaces were normally about 50 cm. away from the luminous region of the discharge so that tarnishing was reduced.

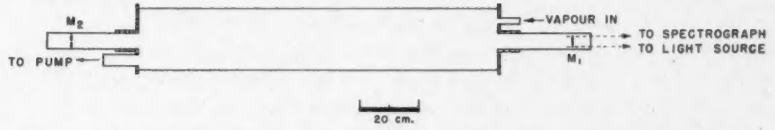

FIG. 1. Diagram of the discharge tube showing the position of the set of multiple-reflecting mirrors M_1 and M_2. The high frequency coil passed round the middle third of the discharge tube.

In most experiments the absorption background was obtained with a "flash tube" of the type used by Ramsay (10). A well exposed background could be obtained with one to five flashes on a Hilger E1 spectrograph in the region λ5000–λ2800. A rotating shutter was used to reduce the intensity of emission from the continuously running discharge to a minimum. In some

* *Issued as N.R.C. No. 2919.*
** *National Research Laboratories Postdoctorate Fellow.*

experiments the oscillator was pulsed; the flash tube being synchronized to fire at the close of each pulse.

The main search was carried out using a Hilger E1 Littrow spectrograph with both quartz and glass optics. The spectral region studied with a single traversal was λλ8000–2500. With a multiple path of eight traversals the spectral range λ7000–2800 was studied. A more restricted search was made using the second and third orders of a 21 ft. grating between λλ7000 and 3100, and one traversal of the discharge tube.

The power level of the oscillator was fixed. A much lower power input could be obtained by placing the discharge tube in an auxiliary coil which was loosely coupled to the main coil. It was found that the optimum conditions for the observation of the OH radical were high pressure and high power input. The pressure used was the highest at which a stable discharge could be run. These conditions are similar to those found by Oldenberg for OH to give the strongest absorption (9); higher pressures could be used in the present experiments because of the different characteristics of the high frequency discharge as compared with the d-c. discharge used by Oldenberg. The maximum pressure varied from compound to compound, but was of the order of 10 mm. It was found that these conditions also gave the strongest absorption with other band systems, and they were therefore used in the search experiments.

The observations on diatomic molecules essentially duplicate the results of previous workers. The SH band at λ3237 was observed in a discharge through H_2S. Bands of the violet CN system were observed in a discharge through cyanogen; the 0–0, 1–1, 2–2, 1–0, and 2–1 bands occur indicating a high vibrational temperature of the CN radicals. The bands of CS at λ2575 were observed in a discharge through CS_2; this has been reported briefly elsewhere (5).

From the results reported by Laird, Andrews, and Barrow (7), it was expected that the spectrum of CF_2 should be observed relatively easily in a discharge through CF_4. A series of experiments in which the power input, pressure, and flow rate of the gas were varied, together with various pulsing techniques, all proved negative. The failure of these experiments must be ascribed to the use of CF_4. Laird, Andrews, and Barrow used a perfluorocarbon (1) Average M. Wt. equivalent to C_7F_{12} which contains a number of CF_2 groups in each molecule. Dr. Barrow also noted that while CF_2 could be observed in a 10 liter bulb, it could not be observed in a discharge tube 4 cm. in diameter, and concluded that wall effects played a dominant part in the decay of the species. In the apparatus used here, the diameter of the discharge tube being 18 cm., wall effects would not be expected to predominate.

The most interesting result is the observation in absorption of the so-called "α" bands of ammonia which have recently been shown to be due to the radical NH_2 (6). Using a single traversal, two lines of the strong NH_2 band at λ5700 were observed in the second order of the 21 ft. grating in a discharge through flowing ammonia at a pressure of $\sim$10 mm. which was pale mauve in color. The total length of the luminous portion was about 70 cm. The in-

tensity of absorption could be greatly increased by increasing the absorbing path using the multiple traversal mirror system. For the spectral region of the "α" band (λ8000–λ4000) a tungsten light bulb gave a very convenient continuous background. The aluminum mirrors were not affected by the discharge under the above mentioned conditions. Satisfactory plates were obtained with a 5 to 15 min. exposure with a path length of 24 traversals of the discharge tube.

The intensity of absorption in the discharge due to NH_2 is estimated to be greater by a factor of about 3 than that obtained by Herzberg and Ramsay (6) in the flash photolysis experiments. Three new bands lying at λ7904, 8160, and 8240 were observed which may, with the more highly developed bands in the visible region, provide useful data for the analysis of this system.

In choosing compounds for the search the possibility of observing band systems due to CH_3, CH_2, C_3 (Douglas (2)), CH, HCO (Dyne and Style (4)), and HCO_2 (Style and Ward (11)) was considered. Discharges through CH_4, C_2H_4, C_2H_2, H_2CO, CH_3CHO, CH_3COCH_3, and HCOOH were examined with the E1 spectrograph with one traversal of the discharge tube. Discharges through CH_4, C_2H_4, C_2H_2, and HCOOH were examined with the E1 spectrograph using 8 or 12 traversals of the discharge tube, and in the second and third orders of a 21 ft. grating using one traversal of the discharge tube. A discharge through CH_4 was also examined in the first order of the grating in the region λ9000–λ7000.

The failure of these last experiments shows that it is not correct to suppose that a discharge in which a particular radical appears strongly in emission necessarily contains the radical in sufficient concentrations to be observed in absorption. For instance CH, NH, and OH bands appear strongly in emission in discharges through CH_4, NH_3, and H_2O. Only OH is observable in absorption under my experimental conditions. The α band of ammonia, which can be observed in absorption, is, on the other hand, not strikingly strong in emission in this discharge. Only in special cases, then, does a discharge contain a sufficient concentration of radicals to be observed in absorption. The intensity of a spectrum in absorption depends on the stationary *concentration* of radicals in the ground state; the intensity in emission depends on the *rate* at which radicals are formed in an excited state and their lifetime in that state. These factors are not necessarily correlated.

ACKNOWLEDGMENTS

I wish to express my appreciation for the considerable help and advice given during the course of this work by Dr. G. Herzberg, F.R.S., and Dr. A. E. Douglas.

1. BARROW, R. F. Private communication.
2. DOUGLAS, A. E. Astrophys. J. 114: 406. 1951.
3. DYNE, P. J. Can. J. Phys. 30: 79. 1952.
4. DYNE, P. J. and STYLE, D. W. G. Discussions Faraday Soc. No. 2: 159. 1947.
5. DYNE, P. J. and RAMSAY, D. A. J. Chem. Phys. 20: 1055. 1952.
6. HERZBERG, G. and RAMSAY, D. A. J. Chem. Phys. 20: 347. 1952.
7. LAIRD, R. K., ANDREWS, E. B., and BARROW, R. F. Trans. Faraday Soc. 46: 803. 1950.

8. LEWIS, M. N. and WHITE, J. U. Phys. Rev. 55: 894. 1939.
9. OLDENBERG, O. J. Chem. Phys. 3: 266. 1935.
10. RAMSAY, D. A. J. Chem. Phys. 20: 1920. 1952.
11. STYLE, D. W. G. and WARD, J. C. J. Chem. Soc. 2125. 1952.
12. WHITE, J. U. J. Chem. Phys. 8: 79. 1940.
13. WHITE, J. U. J. Optical Soc. Am. 32: 285. 1942.

RECEIVED SEPTEMBER 10, 1952.
DIVISION OF PHYSICS,
NATIONAL RESEARCH COUNCIL,
OTTAWA, CANADA.

EFFECT OF A LARGE DIELECTRIC CONSTANT ON GROUND-WAVE PROPAGATION

BY JAMES R. WAIT AND L. L. CAMPBELL

The rigorous theory of the propagation of electromagnetic waves around a spherical earth of infinite conductivity was first developed by Watson (6). His work has been extended to an earth of finite conductivity by Burrows (2), Norton (3), Bremmer (1), and others. Theoretically therefore, solutions are available for any value of the earth's constants (dielectric constant and conductivity) for either vertically polarized or horizontally polarized waves.

Usually in the practical computations of these solutions the relative dielectric constant for the ground is assumed to be in the range from 2 to 15. This is quite justified in most cases for frequencies above 1 Mc. per sec. as indicated by typical measured values, given by Smith Rose (4). At lower frequencies however the dielectric constant can be much greater. For example at 200 kc. per sec. Smith Rose has found the dielectric constant to be greater than 100 for damp soil. When the ground conductivity is poor this can be expected to have a pronounced effect on the propagation. Calculations show that this is the case.

The electric field strength in millivolts per meter for a point on the earth at a distance d miles from the transmitter is shown plotted in Fig. 1. The antenna radiates vertically polarized waves at 200 kc. per sec. and the field intensity at 1 mile for a perfectly conducting earth would be 100 millivolts per meter. For this example the ground conductivity is taken as 0.1×10^{-14} in electromagnetic units. Various values of the dielectric constant ϵ of the ground are shown. For values of ϵ from 2 to 200 Norton's formulas can be used directly for distances up to about 85 miles which is the limit of the flat earth approximation at this frequency. For distances up to 2000 miles Norton gives formulas that can be applied to the case when ϵ is not greater than 15. The complete curve of $\epsilon = 200$ is calculated from Bremmer's expansion formula given on page 45 in his book. The remaining portions of the curves for ϵ equal to 30 and 80 are interpolated.

The curves indicate that an effective dielectric constant of the order of 100 can at great distances from the transmitter give rise to field strengths up to 100 times the field strength for the case when the dielectric constant is of the order of 3. Charts (5) similar to this one have been prepared for other typical values of the ground conductivity in the frequency range from 15 to 500 kc.

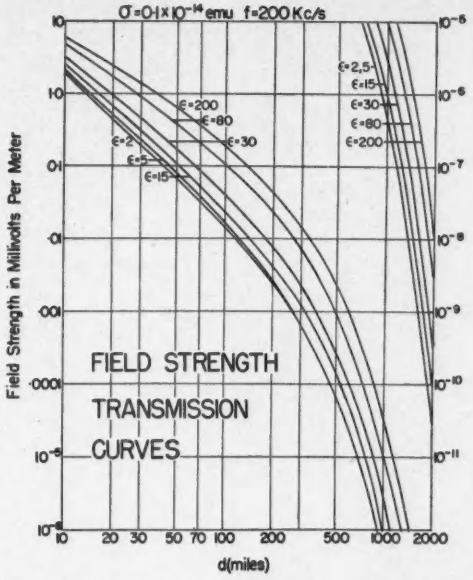

FIG. 1. The field strength of a vertical radiation on the surface of the earth showing the effect of changes of the dielectric constant of the ground.

From this work it appears that the dielectric constant as well as the conductivity has a pronounced effect on ground-wave propagation at low frequencies, particularly when the ground conductivity is less than 1.0×10^{-14} e.m.u. in value.

1. BREMMER, H. Terrestial radio waves. Elsevier Publishing Co. Inc., Amsterdam and New York. 1949.
2. BURROWS, C. R. and GRAY, M. C. Proc. Inst. Radio Engrs. 29: 16. 1941.
3. NORTON, K. A. Proc. Inst. Radio Engrs. 29: 623. 1941.
4. SMITH ROSE, R. L. J. Inst. Elec. Engrs. 75: 231. 1934.
5. WAIT, J. R. and CAMPBELL, L. L. Transmission curves for ground-wave propagation at low radio-frequencies. Defence Research Board, D.R.T.E. Report. (In press.)
6. WATSON, G. N. Proc. Roy. Soc. (London), A, 95: 83. 1918.

RECEIVED SEPTEMBER 8, 1952.
RADIO PHYSICS LABORATORY,
DEFENCE RESEARCH BOARD,
OTTAWA, ONTARIO.

CANADIAN JOURNAL OF PHYSICS

Notice to Contributors

GENERAL: Manuscripts should be typewritten, double spaced, and **the original and one extra copy** submitted. Style, arrangement, spelling, and abbreviations should conform to the usage of this Journal. Names of all simple compounds, rather than their formulas, should be used in the text. Greek letters or unusual signs should be written plainly or explained by marginal notes. Superscripts and subscripts must be legible and carefully placed. Manuscripts should be carefully checked before being submitted, to reduce the need for changes after the type has been set. If authors require changes to be made after the type is set, they will be charged for changes that are considered to be excessive. **All pages, whether text, figures, or tables, should be numbered.**

ABSTRACT: **An abstract of not more than about 200 words, indicating the scope of the work and the principal findings, is required.**

ILLUSTRATIONS:

(i) *Line Drawings:* All lines should be of sufficient thickness to reproduce well. Drawings should be carefully made with India ink on white drawing paper, blue tracing linen, or co-ordinate paper **ruled in blue only;** any co-ordinate lines that are to appear in the reproduction should be ruled in black ink. Paper ruled in **green, yellow, or red should not be used** unless it is desired to have all the co-ordinate lines show. Lettering and numerals should be neatly done in India ink preferably with a stencil (**do not use typewriting**) and be of such size that they will be legible and not less than one millimeter in height when reproduced in a cut three inches wide. All experimental points should be carefully drawn with instruments. Illustrations need not be more than two or three times the size of the desired reproduction, but the ratio of height to width should conform with that of the type page. **The original drawings and one set of small but clear photographic copies are to be submitted.**

(ii) *Photographs:* Prints should be made on glossy paper, with strong contrasts; they should be trimmed to remove all extraneous material so that essential features only are shown. Photographs should be submitted **in duplicate;** if they are to be reproduced in groups, one set should be so arranged and mounted on cardboard with rubber cement; the duplicate set should be unmounted.

(iii) *General:* **The author's name, title of paper, and figure number should be written in the lower left hand corner (outside the illustration proper) of the sheets on which the illustrations appear.** Captions should not be written on the illustrations, but typed together at the end of the manuscript. All figures (including each figure of the plates) should be numbered consecutively from 1 up (arabic numerals). **Each figure should be referred to in the text.** If authors desire to alter a cut, they will be charged for the new cut.

TABLES: Each table should be typed on a separate sheet. Titles should be given for all tables, which should be numbered in roman numerals. Column heads should be brief and textual matter in tables confined to a minimum. **Each table should be referred to in the text.**

REFERENCES: **These should be listed alphabetically by authors' names, numbered in that order, and placed at the end of the paper.** The form of literature citation should be that used in this Journal. **Titles of papers should not be given.** The first page only of the references cited should be given. **All citations should be checked with the original articles.** Each citation should be referred to in the text by means of the key number.

REPRINTS: A total of 50 reprints of each paper, without covers, are supplied free to the authors. Additional reprints will be supplied according to a prescribed schedule of charges. On request, covers can be supplied at cost.

Approximate charges for reprints may be calculated from the number of printed pages, obtained by multiplying by 0.6 the number of manuscript pages (double-spaced typewritten sheets, 8½ in. by 11 in.) and making allowance for space occupied by line drawings and half-tones (not inserts). The cost per page is tabulated at the back of the reprint request form sent with the galley.

Contents

Page

The Initial Magnetization of Nickel Under Tension—*B. N. Brockhouse* - 339

Counting Rate Measurement by Interval Sampling—*M. F. Crouch and G. E. Haynam* - - - - - - - - - - - - - - - - - 356

Plafonnement des Aerostats à Grande Altitude—*Pierre Demers* - 366

Temperature-Pressure Hypothesis and the Earth's Interior—*J. A. Jacobs* - 370

A Determination of the Half Lives of Some Magnetic Dipole γ-Ray Transitions—*R. L. Graham and R. E. Bell* - - - - - - - - 377

The Sound Field of a Piston Source—*Ernest W. Guptill* - - - - 393

The Maximum Age of the Elements and the Age of the Earth's Crust—*C. B. Collins, R. D. Russell, and R. M. Farquhar* - - 402

Fission Yields of the Stable and Long-lived Isotopes of Cesium, Rubidium, and Strontium and Nuclear Shell Structure—*D. R. Wiles, B. W. Smith, R. Horsley, and H. G. Thode* - - - - - 419

Resonant Scattering of Slow Neutrons—*B. N. Brockhouse* - - - 432

The Absorption Spectra of Free Radicals Formed in an Electric Discharge—*P. J. Dyne* - - - - - - - - - - - - - - - - 453

Effect of a Large Dielectric Constant on Ground-wave Propagation—*James R. Wait and L. L. Campbell* - - - - - - - - - - - 456

Printed in Canada *by* University of Toronto Press